ABSTRACT

**MICROMECHANICAL STUDY OF TWO-PHASE FLOW
DURING AIR SPARGING**

**by
Shengyan Gao**

Air sparging (AS) is an in-situ soil/groundwater remediation technology, which involves the injection of pressurized air/oxygen through an air sparging well below the region of contamination. The efficiency of the in-situ sparging system is mainly controlled by the extent of contact between injected air and contaminated soil and pore fluid. Hence, characterizing the mechanisms governing movement of air through saturated porous media is therefore critical to the design of an effective cleanup treatment. However, in spite of the success of air sparging as a remediation technique for the clean-up of contaminated soils, to date, the fundamental mechanisms or the physics of air flow through porous media are not well understood.

In this research, the micro-mechanics of air sparging are studied in order to understand the physical processes of air migration and air spatial occurring on the pore scale during air sparging. First, the void space in the porous medium is characterized by pore network consisting of connected pore bodies by bonds. Two approaches of generating 3D stochastic pore networks were proposed. The first methodology is to directly extract pore structure from a computer simulated packing of spheres. The second methodology is to generate an equivalent 3D pore network of porous media, in which the centers of voids are located in a regular lattice with constant pore center distance. Both algorithms were validated by comparing the predicted permeability of randomly packed spherical particles with published experimental data. The results showed that the predicted permeability values were in good agreement with those measured, confirming that the proposed algorithms can capture the main geometrical information and the topological information of random packing of spheres.

Secondly, based on the developed network model, a rule-based dynamic two-phase flow model was developed in order to study the dynamic flow properties of air water two-phase flow during air sparging. The rules for phase movement and redistribution are devised to honor the imbibition and drainage physics at pore scale. The system is forward integrated in time using the Euler scheme. For each time step, the distribution of the phases leads to a recalculation of the effective viscosities in the network, capillary pressures across the menisci, and thus the coefficients in the equations for the pressure field. When the pressure field is known, the flow field follows automatically and the integration step can be performed.

Finally, the developed dynamic model was used to study the rate-dependent drainage process during air sparging. Two types of numerical tests were performed: one is with one-step air injection pressure while the other one is with multistep air injection pressures. During the two types of numerical tests, the effect of the capillary number and geometrical properties of the network on the dynamic flow properties of air water two-phase flow including residual saturation, changing rate of water/air saturation, air and water spatial distribution, dynamic phase transitions, nonwetting fractional flow, air and water relative permeability and capillary pressure curve were systematically investigated. The results show that all this information for describing the air water two-phase flow properties is not an intrinsic property of the porous medium, but on the contrary, it is affected by the air water flow rate and historical distribution of air water phase. It is also shown that the developed model can capture the dynamic effects on all these data.

At the end of this research, two different ways of performing micro to macro level analysis to obtain the macro behaviors of air water two-phase flow by using micro-mechanics were also briefly discussed. In all, this research has laid substantial basis on understanding the mechanisms of the air water two-phase flow process during air sparging.

MICROMECHANICAL STUDY OF TWO-PHASE FLOW
DURING AIR SPARGING

by
Shengyan Gao

A Dissertation
Submitted to the Faculty of
New Jersey Institute of Technology
in Partial Fulfillment of the Requirements for the Degree of
Doctor of Philosophy in Civil Engineering

Department of Civil and Environmental Engineering

January 2012

.

APPROVAL PAGE

**MICROMECHANICAL STUDY OF TWO-PHASE FLOW
DURING AIR SPARGING**

Shengyan Gao

Dr. Jay N. Meegoda, Dissertation Co-advisor	Date
Professor of Civil and Environmental Engineering, NJIT	

Dr. Liming Hu, Dissertation Co-advisor	Date
Associate Professor of Hydraulic Engineering, Tsinghua University, P.R. China	

Dr. Raj P. Khera, Committee Member	Date
Professor of Civil and Environmental Engineering, NJIT	

Dr. Dorairaja Raghu, Committee Member	Date
Professor of Civil and Environmental Engineering, NJIT	

Dr. John R. Schuring, Committee Member	Date
Professor of Civil and Environmental Engineering, NJIT	

BIOGRAPHICAL SKETCH

Author: Shengyan Gao

Degree: Doctor of Philosophy

Date: January 2012

Undergraduate and Graduate Education:

- Doctor of Philosophy in Civil Engineering,
  New Jersey Institute of Technology, Newark, NJ, 2012

- Master of Science in Civil Engineering,
  Tsinghua University, Beijing, P. R. China, 2008

- Bachelor of Science in Civil Engineering,
  Xi'an University of Technology, Shaanxi, P. R. China, 2005

Major: Civil Engineering

Presentations and Publications:

Shengyan Gao, Jay N. Meegoda, Liming Hu (2011). "Development of Pore-Network Models for Flow through Porous Media." *International Journal for Numerical and Analytical Methods in Geomechanics*, **accepted**.

Shengyan Gao, Jay N. Meegoda, Liming Hu (2011). "Microscopic Modeling of Air Migration during Air Sparging." *ASCE Journal of Hazardous, Toxic, and Radioactive Waste Management*, 15(2), 70-79.

Shengyan Gao, Jay N. Meegoda, Liming Hu (2011). "Microscopic Research on Air Sparging I- Network Model Development." *Geo-Frontiers 2011 and Special Geotechnical Publication*, 4176-4185.

Shengyan Gao, Jay N. Meegoda and Liming Hu (2011). "Geometrical and Topological Characteristics of the Void Space in Random Packing of Equal Size Spheres." *Proceedings of the Engineering Mechanics Institute 2011 Conference*, Boston, 181-191.

Liming Hu, Jay N. Meegoda, Jianting Du, Shengyan Gao, and Xiaofeng Wu (2011). "Centrifugal Study of Zone of Influence during Air-Sparging." *Journal Environmental Monitoring,* 13(9), 2443-2449.

Liming Hu, Xiaofeng Wu, Yan Liu, Jay N. Meegoda, Shengyan Gao (2010). "Physical Modeling of Air Flow during Air Sparging Remediation." *Environmental Science and Technology*, 44(10), 3883-3888.

To my beloved God, for his every minute with me and giving me wisdom and guidance

throughout my life; to my mother for her love and unselfish support for any choice I made.

ACKNOWLEDGMENT

I would like to express my deep and sincere gratitude to Dr. Jay N. Meegoda and Dr. Liming Hu, who not only served as my dissertation advisors, providing valuable and countless resources, insight, and intuition, but also constantly gave me support, guidance and encouragement. I am very fortunate to have these kind and knowledgeable advisors who helped me overcome many obstacles and guided me to a new area of interest.

Special thanks are given to Dr. Raj P. Khera, Dr. Dorairaja Raghu and Dr. John R. Schuring for actively participating in my committee and for giving many helpful suggestion and comments.

I would also like to give thanks to the State Key Laboratory of Hydro Science and Engineering (SKLHSE-2010) and National Natural Science Foundation of China (Project No. 50879038) for providing financial support for this research.

Last, but certainly not least, I would like to thank my family. I especially thank my mother, Xi'e Hu and my two sisters, Xiaoyu Gao and Fangfang Gao, for their encouragement and support in all my life.

TABLE OF CONTENTS

TABLE OF CONTENTS
(Continued)

TABLE OF CONTENTS
(Continued)

LIST OF TABLES

LIST OF FIGURES

CHAPTER 1

INTRODUCTION

1.1   Background Information

According to the U.S. Environmental Protection Agency (USEPA), approximately 495,000 underground storage tank (UST) had been confirmed in September, 2010. While steady cleanup work has progressed for over a decade and over 401,000 contaminated sites have been cleaned up, there are still about 94,000 UST sites contaminated with organic chemicals needing remediation. Although there are many remediation technologies developed to remediate contaminants in soils and groundwater, the site specific characteristics (soil and contaminant type, proximity of groundwater, etc.) make one technology a better candidate than others. The USEPA is working with states to encourage the use of alternative cleanup technologies other than pump-and-treat for groundwater and excavation/disposal for soil. Examples of alternative cleanup technologies include soil vapor extraction (SVE), in situ air sparging (IAS), in situ groundwater bioremediation, biosparging, chemical oxidation, etc., of which IAS has been proved to be effective in reducing concentrations of volatile organic compounds (VOCs) found in petroleum products in contaminated sites. IAS is more applicable to remediating the lighter gasoline constituents (i.e., benzene, toluene, ethylbenzene, and xylene [BTEX]), because these lighter gasoline can readily transfer from the dissolved phase to the gaseous phase. In addition to air stripping, air sparging also promotes bio-degradation by increasing oxygen concentrations in the subsurface, stimulating aerobic biodegradation in the saturated and unsaturated zones. Compared with the traditional treatment approaches, air sparging is a

cost-effective, efficient treatment method. It does not require removal, treatment, storage or discharge considerations for groundwater. Also the equipment is readily available and easily to be installed.

During air sparging, pressurized Air/oxygen is injected below the region of contamination, and while migrating through VOC-zone, it partitions the contaminants into the vapor phase and transports the contaminants to the unsaturated zone. Then the contaminant-laden air is captured by soil vapor extraction (SVE) system and the extracted contaminated air can be treated using conventional air purifying methods, such as carbon filters and/or combustion. The schematic of in situ air sparging system is shown in Figure 1.1.
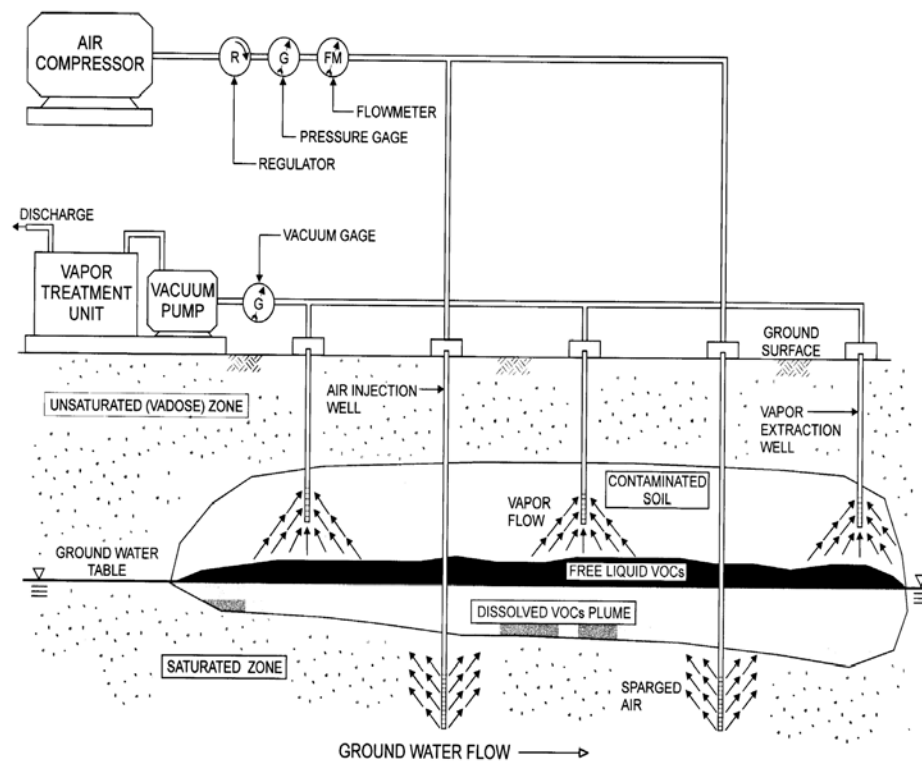
Figure 1.1 Schematic of in-situ air sparging system.

1.1.1   Mechanisms of Cleanup of Contaminants by Air Sparging Algorithm

The contaminants removal during air sparging can be attributed to: (1) mass transfer processes which include volatilization, dissolution and adsorption/desorption, (2) mass transformation process due to biodegradation, (3) mass transport which include advection, dispersion and diffusion.

1. Mass Transfer

Volatilization is defined as the partitioning of the liquid phase compound into the vapor phase. The air sparging process upsets the equilibrium between the gas and liquid phases by gas phase advection, which reduces the vapor phase concentration of the VOC. The volatility of a specific contaminant is indicated by its vapor pressure and Henry's constant. A contaminant is considered strippable and, therefore, suitable for remediation by air sparging if it possesses a vapor pressure greater than 5mm Hg and a Henry's constant greater than 10-5 atm m^3/mol (Brown et al. 1991, Leonard et al. 1992). The distribution of VOC in the gas and liquid phases is determined by Henry's law when the VOC is dissolved in water as in the saturated zone. Henry's law states that under equilibrium conditions, the partial pressure of a gas (i.e., volatile chemical) above water is proportional to the concentration of that chemical in the liquid. However, the velocity of air traveling through subsurface air channels or bubbles may be insufficient to achieve equilibrium as prescribed by Henry's Law. Due to insufficient residence time of injected air within the subsurface, vapor-phase partitioning is a nonequilibrium process.

Although mobile NAPL-phase contamination may directly partition into the vapor phase, a portion of NAPLs will dissolve in the groundwater depending on their aqueous solubilities. Dissolution into the groundwater will continue until equilibrium is established, resulting in a maximum concentration of the dissolved contaminants. In the tests performed with NAPL-phase TEC (Adams and Reddy, 1999) and NAPL-phase benzene (Adams and Reddy, 2000), it is observed that the increased air flow increased the rate of dissolution of mobile NAPL-phase contaminant. Additionally, the increased air agitated the pore water to assist in the dissolution of trapped NAPL-phase contaminant, helping to increase the rate of removal. When considering dissolution for modeling, the short contact

time between trapped NAPL-phase contamination and the mobile groundwater prevents the rate of dissolution from approaching equilibrium.

When contamination is migrating with groundwater through the subsurface due to either natural groundwater or induced groundwater circulation, adsorption of the contaminant to soil may retard movement as compared to groundwater movement. The organic contaminants can be adsorbed in a very thin layer to the exposed edges of clay, or they can be sorbed into a thin layer of naturally occurring organic matter on soil surfaces. The amount of adsorption of an organic contaminant onto soil is more dependent on the organic content of the soil. The amount of adsorption onto soil is also dependent on the moisture content of the soil because water competes effectively for adsorption sites. The greater the saturation is, the greater the displacement of the organic contaminant by water is. Adsorption/desorption may be modeled as either an equilibrium of a nonequilibrium process. If adsorption/desorption is a fast, reversible process, it may be modeled as an equilibrium process using an appropriate isotherm, as detailed in Adams (1999). However, if adsorption/desorption occurs slowly, it must be modeled as a nonequilibrium process using a nonequilibrium kinetic model.

2. Mass Transformation

Biodegradation is the mass transformation of organic compounds that occurs at many contaminated sites provided suitable microbial populations as well as adequate concentrations of nutrients and electron acceptors exist within the subsurface. Biodegradation is often represented as a sink term when coupled with other mass transfer/transport terms. Considerable debate on the importance of biodegradation during air sparging has taken place and most air sparging models neglect the biodegradation

(Sellers et al., 1992, Unger et al., 1995 and Wilson et al., 1994) due to the significant amounts of dissolved oxygen needed to cause complete mineralization of the organic compounds. So far, the benefits of biodegradation during the air sparging process have not been thoroughly quantified.

3. Mass Transport

The contaminant transport mechanisms, namely, advection, mechanical dispersion and molecular diffusion dictate the overall removal of contaminants from the subsurface during the air sparging process. Advection movement may result from either injected air or groundwater flow. The injected air induces significant removal of contaminants through vapor-phase partitioning while groundwater flow may result in spreading of aqueous- or NAPL-phase contamination, depending on the magnitude of groundwater velocity. The advection occurs in response to a pressure gradient resulting from injected air; as a result, the air flow rate is the key factor that affects the vapor-phase removal. Mechanical dispersion or simply dispersion is a mass transport mechanism that arises from variable flow within porous media. Diffusion refers to the contaminant transport from areas of higher concentration to areas of lower concentration. This may occur at both the macroscale and the microscale. At the macroscale, diffusion from regions of higher concentrations to regions of lower concentrations will lead to contaminant migration. When air sparging is implemented, the contaminant removal occurring within the zone of influence will create a concentration gradient, inducing contaminant movement from surrounding regions into the zone of influence. At the microscale, diffusion is necessary for contaminant remediation in regions not in immediate vicinity of an air channel. Braida and Ong (1998) and Rabideau and Blayden (1998) used a two compartment model to account

for this diffusion. The first compartment represented regions in the immediate vicinity of air channels that are subjected to direct volatilization. The second compartment represents regions that are not directly affected by air channels and rely upon diffusion for contaminant removal. The regions outside of the zone of influence relied upon macroscale diffusion for contaminant removal, greatly increasing necessary remedial times. When lower air channel densities and air saturation within the zone of influence, such as in tests using fine sand as the test soil or during tests with lower air injection flow rates, microscale diffusion became more important for contaminant transport to air channel to removal. This behavior led to greatly increased remedial times.

Generally, during air sparging, mass transport is the primary mechanism controlling contaminant removal (Bausmith et al., 1992). At the onset of sparging, contaminant mass removed is mostly from the evacuation of vapors in the soil pore space on the unsaturated zone in equilibrium with the surrounding organic contaminant (Brown et al., 1991) followed by advective and dispersive/diffusive transport of contaminant from the surrounding aqueous phase to the zone of influence (Cho, et al, 1991). Diffusive transport can be limited by slow mass-transfer from immobile non-aqueous phase liquids (NAPLs) to the advecting aqueous and gas phases, as well as from areas of low permeability within the aquifer (Wilson et al., 1992). Contaminant removal through air sparging induced biodegradation is secondary to mass transport, but becomes increasingly more significant in long-term operations. Semer et al. (1998) evaluated these different mechanisms that control the contaminant removal from saturated soils during air sparging based on laboratory air sparging column experiments conducted on two types of soil: Ottawa sand and fine gravel, that are contaminated with toluene. According to the test

results, it has been concluded that: (1) For the saturated sand and gravel which are contaminated with toluene, volatilization was the most dominant contaminant mass transfer process that occurred. The volatilization rates depend on the distribution of the injected air in the soil. (2) During air sparging, dissolution of NAPLs such as toluene into the dissolved phase occurs very slowly, but this dissolution is likely to increase with increased injected air movement in soils. (3) The adsorption of the contaminant to the soils tested in this study was negligible, however, adsorption can be a significant retardation mechanism in soils which either contain large amounts of clay or have a high organic content. (4) Biodegradation is not significant in these experiments due to the lack of microorganism in the test soils and the short duration of the tests. (5) In soils where the injected air cannot be evenly distributed, contaminants will migrate into the air passageways due to diffusion. (6) In sandy soil, volatilization, dispersion, dissolution, and diffusion may be the major contributing mechanisms for contaminant removal with diffusion being the rate-controlling mechanism. In gravelly soil, dispersion, dissolution, and volatilization may be the most significant mechanisms with dissolution likely to be the rate-controlling mechanism.

1.1.2 Current Macroscopic Research on Air Sparging

Based on the above brief summary and evaluation of contaminant removal mechanisms, it can be concluded that the efficiency of in situ sparging system is mainly controlled by the extent of contact between injected air and contaminated soil & pore fluid. As a result, the determination of size and shape of zone of influence (ZOI) and the understanding of air flow dynamics and air spatial distribution within zone of influence are of essential importance in air sparging design.

Quantities of mathematical models have been developed to improve our understanding and ability to predict air migration patterns and spatial distribution in different subsurface environments. In a recent state-of-the-art publication, McCray (2000) presented a comprehensive review of the two types of published mathematical models used to simulate air sparging: 1) lump-parameter models; and 2) multi-phase fluid flow models. The details of the models will not be discussed here and readers are referred to McCray (2000). The former type of mathematical models simulates various mass transfer processes by lumping them into compartments and bulk parameters. However, compartmentalized or lumped-parameter models cannot fundamentally describe the spatial distribution of injected air and the associated spatial behaviors of air-sparging physics and chemistry. Usually, in this type of models, the air channels are assumed to be uniformly and evenly spaced. In addition, the number of air channels may be arbitrary. For example, Wilson et al. (1997) used randomly spaced air channels to simulate the sparging of dissolved volatile organic compounds (VOCs) and nonaqueous phase liquids (NAPLs) from contaminated aquifers. A random generator was used to determine the spatial coordinates of air channels. In addition, according to McCray (2000), the principal limitation of these models is the assumption of complete mixing within compartments. This assumption may not hold for widely spaced air channels and severe heterogeneous soils. The second type of mathematical models - multiphase fluid flow model, on the other hand, considers the interaction between the different phases flowing simultaneously through the medium. This type of models includes capillary pressures between air and water and the mutual impedance (relative permeability) of the two phases (McCray 2000). In this type of models, the simulation of air phase and water flowing through the porous media uses an extension

of Darcy's single-phase flow equation, where pore-size distributions, pore throat sizes and shapes, and pore interconnectivity are all lumped into a single soil permeability value. For each phase, the hydraulic conductivity is a function of saturation. However, in the current numerical simulation of air water two-phase flow during air sparging, the hydraulic properties of porous media are generally assumed to be of a static nature, and this implies that the relationship between water content, matric potential, during monotonous draining or imbibition processed is not affected by the dynamics of water flow. Traditional, the water retention characteristic is measured in the laboratory under equilibrium conditions, and it is generally assumed that the so-determined properties can be used to model transient water flow under field conditions. However, comparison of drainage retention data obtained with dynamic methods and using the conventional approach indicate that more water will be held at a given suction in the dynamic case. If dynamic nonequilibrium occurs between the water content and water potential during transient water flow, the presently used standard simulation technique for describing saturated/unsaturated flow cannot be reliably applied under transient flow conditions.

According to the above review current mathematical models for air sparging need further improvement on the temporal evolution of spatial distribution of air water distribution. As we know, pore-scale study on the two-phase flow can consider the spatial distribution of each phase and can also take into account the effect complicate soil structure on two-phase flow dynamics. Hence a microscopic study of air water two phase flows will be an excellent technique to investigate the efficiency of air sparging.

1.1.3   Current Microscopic Research on Air Sparging

The growing interest in pore-scale models is due to wide range of applications that can be used with these models, such as wettability, multiphase flow dynamics, hysteresis, single-phase or multiphase mass transfer, and dispersion (Jerauld et al., 1990; Reeves et al, 1996, Blunt et al., 2001; Niasar et al., 2008). In this section, the current published research related to the microscopic modeling of air sparging is briefly summarized. Some of them may not be classified as microscopic approach; however, they do provide some insight to pore level modeling of air sparging.

Contrary to the assumption for most macroscopic research that the air phase was continuous during the air sparging, the air is considered as a discontinuous phase in the model developed by Zhu (2006) for estimating the ZOI (Zone of Influence) during air sparging. The porous medium is reconstructed as a network of 'Rooms' and 'Doors'. For an REV (Representative Elementary Volume), which refers to an element of the porous medium that contains soil grains and pore space, the term 'Room' refers to the pore space in the REV while the 'Door' refers to the fluid channels connecting the rooms. The door is considered closed when it is full of water and opened when it is full of air. The interstitial pore liquid (water) is assumed always continuous in the network and its movement is governed by Darcy's Law. At any time, the air can exist in one or more rooms and the doors can be either opened or closed. When the two rooms are air saturated (i.e., $\theta = \theta_{max}$), and the pressure in one room is sufficiently high to open a door between them, then the door can be opened. Once the door is open, the air of these two rooms is connected and considered to be continuous through the rooms, and shares the same pressure. If multiple doors are open at a given time, large continuous air bubbles may form. Once the air

pressure inside a multi-room air bubble drops below the door's force, that door will close so that the air bubble is divided into smaller bubbles until the internal air pressure is sufficient to re-open all of the doors. When air is injected into the Room-Door network (the porous medium), the doors open and close with the change of internal air pressures. Hence the air plume's internal structure evolves with time, meaning that the sizes, number, and locations of air bubbles in an IAS air plume vary with time. Once the air pressure distribution is obtained within the air plume, the pressure of the pore liquid at the interface between air and liquid is also known by taking into account the capillary pressure. The water pressure at the boundaries of the air plume gives rise to a hydraulic gradient which causes water flow. According to the brief summary of the above research, it can be concluded that this model is based on REV (Representative Element Volume), it cannot take into account the structure properties of porous media, especially the heterogeneous soil matrix. In addition, the model is also based on the assumption that the air phase is distributed uniformly within the air plume during the air sparging; thus, it is not applicable to the general situation where the air bubble or channel density varies within ZOI. Most importantly, this model can only consider the quasi-static pressure evaluation in air and water. It cannot consider the dynamic properties of air water two-phase during air sparging.

Another model which describes the air phase distribution during air sparging from microscopic prospective was developed by Seleker (2006). In order to take into account the buoyant force and viscous force of discrete bubbles during the air sparging, the air sparging zone is divided into two regions: one is far source region, and the other one is near source region. In the region far from the source, the air flow channels are formed primarily due to buoyant forces constrained by capillary entry pressures. In this region, the channel

diameter is estimated by assuming a simple geometry of a cylindrical channel. The upward growth of the plume is driven by the buoyancy of the upper hemispherical volume in the cylindrical channel, and restrained by the surface tension exerted on the hemisphere. By balancing the buoyant force and surface tension, the radius of channel is obtained as $R = \sqrt{\frac{3\sigma}{\Delta\rho g}}$. The invasion process described in his model is one of discrete nearly full gas filled channel of flow rather than smoothly varying volumetric gas contents as would be represented in a continuum multiphase models. Assume the air injection rate of Q during air sparging and Darcy's law for the gas phase, the cross sectional area of gas flow is obtained as $A \geq \frac{Q\mu}{\Delta\rho g k_{sg}}$, where k_{sg} is the gas permeability at complete gas saturation. Then the number of vertical gas flow channels N is of the order $N \approx \frac{Q\mu}{3\pi\sigma k}$. If the probability distribution for lateral position of any single channel is Gaussian with a variance that grows with the square root of total displacement, then the spatial distribution of air channel can be obtained. In near source region, the pressure gradients exceed buoyant gradients and thus air exhibits largely radial flow. The radius (three-dimension model) can be estimated as $R_{3d} \approx \sqrt{\frac{Q\mu}{4\pi\Delta\rho g k}}$. The lateral near field was estimated as roughly twice as wide as its deep, thus the shape can be described as an ellipsoid rather than a hemisphere. The boundary between the 'near source region' and 'far from the source region' is where the energy gradients from buoyant and pressure force are equal. To some extent, this model can be used to roughly estimate the size of the ZOI in homogeneous soil. However, this model is based on the assumption that air moves in gas saturated channels from bottom to top of the soil and this is generally not expected to bifurcate, join each other nor get trapped during the air sparging. In addition, the buoyancy is considered as the driving force while the

surface tension is the resistant force. This is not the case for both bubble and channel flows. In reality, as for bubble flow, drag force cannot be ignored and for channel flow, the air is mainly driven by air injection pressure. However, the advance of this model lies in it firstly presents the idea of separating air plume into two regions: 'near source region' and 'far from source region' which provides insight to microscopic modeling of air sparging.

Elder (1999) developed a very simple model to estimate the air-water interface per unit volume of soil based on analysis of digital images of air channels passing through submerged glass beads having particle size of sand. This model is based on the assumptions that: the channel spacing is reasonably constant for a given medium, as a result, hexagonal pattern of distribution in horizontal plane was used in the model, and the ratio of channel diameter to channel spacing did not vary significantly for different media. Then typical value for channel diameter and ratio of channel diameter to channel space were used to determine the interfacial area per volume of soil. However, his model oversimplified the system and hence it is not applicable to both field and laboratory tests.

For the bubble flow, Corapcioglu, et al. (2004) theoretically studied the rise velocity of an air bubble in coarse porous media. This model is based on balance of forces acting on a bubble rising in porous medium. The forces include inertial force, added mass force or inertial force, buoyant force, surface tension and drag force among which the added mass force or inertial force is due to the flow field created by the bubble if it accelerates relative to the surrounding fluid and the drag force results from the momentum transfer between the phases. The momentum transfer terms take into account the viscous as well as the kinetic energy losses at high velocities. The drag force acting on a bubble was expressed by the modified Ergun equation. In Ergun's equation, the viscous energy losses

are expressed by the Kozeny equation for laminar flow, proportional to the first power of the velocity, while the kinetic ones are expressed by the Burke-Plummer equation for turbulent flow, proportional to the product of density with the second power of the velocity. Velocities of steady state, quasi-steady and unsteady state bubble motions were calculated. Results showed that for larger bubbles, the buoyant force dominated and it was similar in magnitude to the total drag force. The result of steady state bubble rise velocity matched with the experiment data reported by Roosevelt and Corapcioglu (1998) for bubbles with radii greater than 2 mm. This is model can be used to estimate the average bubble flow velocity in coarse sands during air sparging. However, the average air bubble size and spatial distribution cannot be obtained from the model, and the forces analyzed in the model cannot be applied to channel flow. In addition, this model could not describe the flow properties of air phase such as the flow pattern transition and bubble breakup or coalescence.

1.2 Discussion of Microscopic Research on Air Sparging

In order to investigate questions of interest regarding two phase flow in porous media, it is possible to apply methods that count as theoretical, experimental or numerical. Experimental methods provide quantitative results for the actual system investigated. However, experimental results may differ from sample to sample or from system to system. By means of numerical simulations the system properties can be controlled to a greater extent. This is highly advantageous when one wishes to study the effect of varying parameters of the system. As a result, numerical approach of studying two-phase flow properties during air sparging will be employed in this research.

In order to investigate both the air flow dynamics during air sparging and the temporal evolution of air water spatial distribution in the porous medium, and also to bridge the gap between microscopic research and macroscopic research, pore network model can be employed for this purpose. Pore network model, in which the pore space is represented by a 3D network of interconnected pores and throats, are used extensively to compute important macroscopic transport properties including capillary pressure, relative permeability and residual saturation, etc. Pore-scale network models are based on solution of certain flow equations and interface conditions on a domain composed of idealized shapes that are meant to capture the essential features of natural porous media. The research approach of using pore network model contains two main parts: one is for characterizing the void space in porous medium, and the other one is for developing dynamic air-water two-phase flow model.

As is known that, the flow of fluid in a granular material occurs through interconnected pores between solid particles, as a result, the water and solute transport and the distribution of fluid phases in subsurface systems are directly related to the geometry and the topology of the pore space of porous medium. Hence the physical properties that are related to fluid-flow and chemical transport such as permeability and dispersivity, and electrical conductivity of a porous medium depend on the structure of the solid phase or on the geometry and topology of the pore space. As a result, the most critical part of constructing a pore network model is the identification of the geometrical and topological properties of the voids within the porous media and the predictive value of pore network models depends on the accuracy with which the network captures the complex geometrical and topological properties of pores. Blunt et al. (2002) suggested that if the complex pore

geometry can be adequately represented, then pore-scale models can be developed into predictive models. However, because of the complexity of the pore structure, most of previous pore-scale models for fluid movement through soils were based on simplifications that idealized the complicated soil structures (Crawford, et al. 1994; Abichou et al, 2004). Traditionally, network models represented the void space of soil by regular two- or three-dimensional lattice of wide pores connected by narrower throats with constant coordination number of six. Each pore or throat was assumed to be cylindrical or spherical and hence contain just one phase. In addition, the pore sizes were spatially uncorrelated. However, real systems allow two or even three phases to be simultaneously present in a single pore, have a random topology and have correlated pore size. In addition, these models are unable to account for the interconnectivity of the pore space, and as reported in actual porous media, the connectivity is distributed, and can have coordination number greater than six (Kwiecien, et al., 1990). It is also reported by Arns et al. (2004) who performed a comprehensive study of effect of network topology on relative permeability that even by matching the average coordination number of a network, it is still not sufficient to match relative permeability. However, by matching coordination number distribution, the results were more reasonable.

In recent years, several advances have been made in the construction of realistic representations of porous media. Al-Raoush et al. (2003) classified the methods used in generating pore- scale network into two main types: In the first type, the geometric parameters of a regular network (often having pores of circular cross section) are tuned to match available experimental data. This may involve removing throats on a cubic lattice to reduce the coordination number, and adjusting the pore size distribution (Dixit, et al., 1998,

1999 and 2000 and Fischer, et al., 1999). Then this model is used to predict other properties that are more difficult to measure (Zhou, et al., 2000, Dillard, et al., 2000, Dixit, et al., 1999 and Fischer, et al., 1999). The problem with this approach is the non-uniqueness of the solution obtained due to the dependency of macroscopic properties such as relative permeability and capillary pressure in both the topology of the pore space and the pore size distribution (Vogel, 2000). The second method is direct mapping of a specific porous medium onto a network structure. This method requires a representation of the pore structure prior to the construction of the network. Two main approaches can be used in this method:

a. The three dimensional reconstruction of the pore space based on the measured porosity and correlation functions or serial cross sections (e.g., Vogel and Roth, 1997, Bakke and Oren, 1997, Liang, et al., 1999 and Okabe and Blunt, 2003). This approach works well for sedimentary systems.

b. Direct three-dimensional non-destructive imaging using micro-tomography or magnetic resonance (e.g., Baldwin, et al., 1996 and Rintoul, et al., 1996).

While building the three dimensional network of porous media, special attention should be paid to the shape of pore space. Actually, individual pores and throats can be modeled as triangles or a square. The essential feature of these two cross sections is that wetting phase can reside in the corners. This allows wetting phase to occupy the corners when the non-wetting phase fills the center. Models based on three-dimensional reconstructions of porous media have successfully predicted relative permeability using pores with an irregular triangle cross-section (Oren, et al., 1998 and Lerdahl, et al., 2000). Some authors have used a grain boundary pore shape, formed at the junction of four

spherical particles (Man, et al., 1999, 2000 and 2001, Mani, et al., 1998 and Kagan, et al., 2000), while others have advanced a fractal-type model of pore wall roughness (Tsakiroglou, et al., 1999 and 2000).

As to the simulation of air water two-phase flow in pork network, network models have been used extensively to study different displacement processes in simple or idealized porous media (Blunt & King, 1991; Mani & Mohanty, 1996). If two immiscible fluids are present in the porous medium, the fluid for which the contact angle is smaller than 90 is called the "wetting fluid"; the other one is called the "non-wetting fluid". The displacement of wetting phase from a porous medium is called drainage. In such two-phase flow situations, the flow problem becomes complicated due to the introduction of capillary pressure. The ratio of viscous forces to capillary forces, called the capillary number (N_{ca}), can affect the flow behavior. In the limiting case of capillary-dominated flow, the invasion percolation model (Chandler et al. 1992; Mohanty et al. 1982; Wilkinson et al., 1983; Lenormand et al., 1985) adequately describes two-phase flow through the porous media by using concepts from percolation theory. In the other limiting extreme of viscous-dominated flow, the diffusion-limited aggregation (DLA) model describes the displacement of high-viscosity fluid by a low-viscosity fluid, thereby giving rise to pore scale viscous fingering (Chen et al., 1985). Both theories described the porous media as a set of interconnected pores. These theories expand the capillary tube models by allowing virtually any interconnectivity and pore-size distribution and associated pore space. The pore volume of porous media is assigned to pores and the flow resistance of porous media is assigned to pore-connectors. Percolation theory was originally developed by Broadbent, (1957) to study resistor networks. It was later extended and used by a number of

researchers (Chandler, 1982, Larson, 1981, Heiba, 1984, Pathak, 1982 and Wilkinson, 1984) to study two-phase capillary flow in porous media. In this model, flow qualitatively similar to capillary fingering. Chandler (1982) numerically generated percolation like clusters using a non-uniform pore grid. A displacing fluid was introduced on a non-uniform grid of random flow resistances. The displacing fluid moves into the grid of lowest flow resistance on the boundary between the displacing the displaced fluid. This process is repeated over and over again. The only additional rule is that the displaced fluid which is completely surrounded by the fluid that cannot be displaced. But percolation theory is limited to very low flow rates dominated by capillary pressures. The diffusion limited aggregation (DLA) is another technique used by several researchers (Meakin, 1983 and 1984 and Witten et al., 1983) to numerically generate fractals which physically occur in porous media flow. The DLA has been limited to simulating highly mobile fluid flows displacing a less mobile fluid in the limit grid moving randomly. However, both invasion percolation and DLA are rule-based models and work very well in the limiting cases described above. In summary, percolation theory was successful in simulating flows dominated by capillary pressures, while DLA theory was successful in simulating the fingering of a highly mobile fluid into a very viscous fluid (e.g., Koplik, 1982, Dias, 1986, Lenormand, 1988 and Yanuka, 1989). These models do not contain any physical time for the front evolution and they cannot describe the crossover between the major flow retimes.

In a more general two-phase flow situation where both viscous and capillary forces are present, a suitable combination of rule-based model is needed to adequately describe flow. For this, one can use a rule-based model to update the fluid configuration and then to determine the pressure field while immobilizing the interfaces-such models are known as

dynamic network models. The essential difference between the static models and dynamic models lies in the computation of the pressure field. In static network models (e.g., percolation theory), the pressure field is assumed to be uniform in each phase (in the absence of gravity). However, the dynamic network models estimate the pressure field at each time step and make rule based interface movements based on the computed pressure drops in both phases but makes the problem more computationally intensive.

1.3   Research Objectives

The main goal of this research is to develop a predictive mathematical model that can simulate the micromechanics of air-water two-phase flow during air sparging and then based on the developed model to investigate dynamic flow properties of air water two-phase flow during air sparging under different boundary conditions. Specifically, our research objectives consist of three main parts:

The first part is about developing a 3D stochastic pore network model to characterizing the void space in porous medium which can capture both the geometrical and topological information of void space. Two methodologies of constructing such 3D stochastic pore networks are proposed: one is by directly extracting the void space from the random packing of spheres while the other one is by constructing an equivalent 3D pore network. In the second part, a dynamic two-phase flow model which can simulate time-dependent and flow rate-dependent air spatial distribution and movement of menisci in porous media during air sparging is developed. In the third part, the developed dynamic AIRFLOW model is employed to study the dynamic flow properties of air water two-phase flow including residual saturation, changing rate of water/air saturation, air and water

spatial distribution, dynamic phase transitions, nonwetting fractional flow, air and water relative permeability and capillary pressure curve during air sparging with both one-step air injection pressure and multistep air injection pressures.

CHAPTER 2

DEVELOPMENT OF PORE NETWORK MODEL OF POROUS MEDIUM

2.1   Introduction

In order to employ microscopic approach to study air migration in soil or to predict macroscopic properties (e.g., permeability, relative permeability) of soil, accurate 3D representation of the pore space with accurate characterization of pore morphology is needed.

Generally, there are two approaches commonly used for constructing the pore network of porous medium. The first attempts to directly map a specific porous medium onto a pore network structure. The second attempts to create an equivalent pore network using statistical distributions of basic morphologic parameters. The fundamental difference between the two methods is that direct mapping provides a one-to-one spatial correspondence between the void structure in porous medium and the pore network structure, whereas the second method develops the network that is equivalent only in a statistical sense. However, the appeal of the second approach lies in its simplicity and ability to quickly access to the effects of complex soil structure (heterogeneous soil) on fluid flow characteristics. In addition, Markus (2003) calibrated equivalent pore-network models to three experimental porous medium systems and found that although the morphology of calibrated networks did not capture all aspects of the packing, the result showed good agreement between the simulated and measured capillary pressure-saturation curves. In this chapter, two methodologies of developing pore network models for characterizing void space in porous medium are proposed. This chapter is

organized as follows: Section 2.2 describes the first methodology of developing an equivalent 3D network model which can match both geometric and topological information of porous media, and Section 2.3 presents the second methodology of directly extracting pore network from random packings of spheres. Then the geometrical and topological properties of void space in random packing of equal size spheres were studied by the second methodology and the results are presented in Section 2.4. Finally, the validation of the two methodologies is provided in Section 2.5. At the end of this chapter the main conclusions are briefly summarized.

2.2   Development of Equivalent Pore Network Model of Porous Medium

In this section, the procedures of developing an equivalent pore network model of porous medium are presented. The whole procedures can be divided into four steps which will be described separately.

2.2.1   Procedures of Constructing an Equivalent Pore Network

I.   Generate geometric and topological parameters

During the first step of developing an equivalent pore network, the soil parameters including void ratio and permeability should be inputted to the model for the calibration purpose. Then once the equivalent network is constructed, the void ratio and the permeability of the network should be computed and compared with the inputted parameters. If the computed parameters match the inputted soil parameters, it means the constructed pore network can capture the main geometrical and topological properties of the soil and the pore network can be used to simulate single phase flow or air water two-phase flow. Otherwise, the geometrical and topological parameters should be

modified and the whole procedures of constructing equivalent pore network are needed to be repeated.

Besides the soil parameters mentioned above, the main geometric and topological parameters of the network including total number of pores in the network, average pore size, maximum and minimum pore size, standard deviation of pore size, pore spacing, parameters for characterizing the bonds connecting two neighboring pores, average coordination number, standard deviation of coordination number are also needed to be inputted. Then based on the inputted parameters, the coordinates of the all nodes in the network and the corresponding distribution of geometrical and topological parameters of the network should be generated. Finally, the generated parameters are assigned to each nodes of the network. In the following parts, the discussions on estimating the inputted geometrical and topological parameters of the networks are provided.

(1)   Pore size distribution.

The pore size distribution information can be extracted from three-dimensional images of unconsolidated porous media systems. Two approaches can be used for this purpose. The first approach utilizes a pixel image of the pore space. It is an extension to unconsolidated systems of a medial-axis based approach (MA). The second approach uses a Modified Delaunay Tessellation (MDT) of the grain locations. Riyadh et al. (2003) compared the two techniques and concluded that the MDT method is able to extract the correct pore body and throat size while the MA-based method is resolution-dependent and precise locations of nodes are non-unique, as a result, the exact inscribed pore body and throat sizes were underestimated. Hence the second method of MDT is used in this research. For this method, granular medium is needed to

be modeled by the assemblies of poly-disperse spheres. This can be completed by computational code such as PFC^{3D} which describes the behavior of independent bodies belonging to smooth discrete elements (Cundall et al. 1979). Besides the above method for generating the pore size distribution, this research employs another simple method of generating the pore size distribution by using the normal or log-normal functions to describe the pore size distribution. So once the average pore size, standard deviation of pore sizes, and the maximum and minimum pore size are inputted, the pore size distribution can be generated very easily. The basis of this method is based on research of Reboul et al. (2008) and Rouault et al. (1998). Reboul et al. (2008) studied the void size distribution curve for narrowly graded packing of spheres and found that the distribution curve was unimodal and asymmetrical, as a result, it can be expressed by a log-normal law. Rouault et al. (1998) used a probabilistic approach to correlate the void size distribution (VSD) and particle size distribution (PSD) and they also concluded that VSD was bell shaped (Gaussian and log-normal distribution). The parameters of the pore size distribution function can be estimated by matching the void ratio values. Of course, for the generated Gaussian distribution curve, it has to be truncated to ensure that all the pore sizes are in the range of maximum and minimum pore sizes.

It should be noted here that the generated pore sizes are corresponding to the size of the largest inscribed sphere in the packing of spheres. Although the shape of pore body can be a cube, tetrahedral, or star shape, the effect of shape of cross-section on the air water two-phase flow can be studied separately by finite element method or boundary element method. As a result, the proposed 3D network has flexibility and can be adapted to model complicate soil structures.

(2)   Pore spacing-characteristic length of the network.

This is also an important parameter of the network. It determines the size of the network once the total number of nodes is determined. As a result, it affects the void ratio of the network. Unfortunately, for a real porous medium, this pore-to-pore spacing is not easy to determine, as a result, there are no consistent opinions on how to choose the distance between pore center to center for natural soil. Roychoudhary (2001) indicated that it should exceed six hydraulic radii while Bryant et al. (1993) suggested that it should be larger than one grain size. But for the 3D network developed in this research, this parameter is estimated by matching the void ratio and the coefficient of permeability of the porous medium, which can be easily obtained by laboratory tests. For regular packing of uniformly-sized or narrowly graded particles, the pore space can be considered to be equal to layer space which depends on the type of packing. For random packing of uniformly-sized spheres, Haughey (1969) suggested a simple method for evaluating layer spacing of a rhombohedral unit cell in which the spheres are moved equally apart to give a bulk mean voidage ε, then layer space can be determined as βD_p where D_p is the sphere diameter, and $\beta = \sqrt{2/3} \left[\pi / (3\sqrt{2}(1-\varepsilon)) \right]^{1/3}$.

(3)   Pore throat size distribution.

This section describes the methodology to generate pore throat size distribution. The pore throat size is usually correlated to the pore body size and the pore spacing. Dullien (1992) assumed the pore throat radius to be proportional to the adjacent larger body radius. Mani et al. (1999) generated throat size and pore size independently by Weibull probability distribution function and then assigned the size of throat based on the average size of the two adjacent bodies. The strong correlation between pore size and

throat size was also considered by Markus et al. (2003). However, there are no well-established correlations between pore throat size and pore body size. In order to solve the both problems this research introduces BACON bond as a replacement of the traditional cylindrical bond with constant cross sectional dimension. This type of bond was also used by Acharya et al. (2004). It assumes the bond between node A and B is composed of two parts: the left part (from node A to throat) and the right part (from throat to node B). Here each node represents one pore body. Each part is formed by rotating smooth curves around the axis. Each curve is tangent to its adjacent pore body and can be expressed by two simple power functions. The left curve can be expressed by $y = y_i(1 - x/l)^n$ while the right part can be expressed by $y = y_j(x/l)^n$, where x is the distance from the center of pore body i; l is the pore spacing between the two adjacent pores: pore i and j; y_i and y_j can be determined by the point of tangent between the curve and the pore body and n is called curvature constant, which determines the shape of each curve. The position of the throat can be determined at the intersection of the two curves and the radius of the throat is the y value at the position of the throat. As a result, it can be found that the position and size of the throat is affected by both the pore size and the pore spacing. In addition, the cross sectional dimensional of the bond can smoothly changes from the starting point of the bond to the position of the throat. Hence, it can capture the main structural properties of the soil matrix much better than that of traditional cylindrical bond. Another advantage of BACON bond lies in its simplicity. Once the pore size distribution and pore spacing are determined, the n value is the only parameter needed for this type of bonds. The *n* value can be the same for all bonds in the network or it can be varied. It can also be very easily adjusted to match the measured void ratio and coefficient of permeability of the soil matrix. In addition, the

expression of the bond shape by simple equation also allows the mathematical study of the effect of size and shape of cross-section on migration of air during two phase flow. Here it is also worth to mention that, the size of each bond section determined by two power functions is corresponding to the largest inscribed circle in the cross-section of bond, while the shape of bond does not have to be circular.

(4)   Coordination number distribution:

Coordination number distribution of a natural soil is almost impossible to obtain at present. However, for packing of soil particles with a certain particle size distribution, its coordination number can be obtained by grain reconstruction technology (Thovert, et al. 2001; Reboul, et al. 2008). The coordination number distribution can also be obtained by first designating the function of coordination number distribution and then adjusting the parameters of the function to match the measured permeability of the soil. For the laboratory experiment of air sparging where uniformly sized glass beads or narrow size region glass beads are usually used, the coordination number of this type of soil can be reasonably estimated. For the regular packing of uniformly-sized spheres, the packing patterns can be classified into cubic, ortho-rhombic, tetragonal-sphenonoidal and rhombohedral types. The corresponding coordination numbers are 6, 8, 10 and 12, respectively. For random packing of uniformly-sized spheres, the above mentioned correspondence does not occur and the coordination number distribution is approximately normal about the mean values. Haughey and Beveridge (1966) suggested one model as show in Equation 2.1, which gives the average coordination number as functions of the bulk mean voidage for random packing of uniformly sized particles and it fitted the experimental data. In Equation 2.1, m is the average coordination number and ε is the

voidage (porosity) of random packing of uniformly-sized spheres. Haughey (1969) further suggested that for very loose random packing, bulk mean voidage is about 0.46-0.47, for loose random packing, the bulk mean voidage is about 0.40-0.41, for poured random packing, the bulk mean voidage is about 0.375-0.391, and for close random packing, the minimum voidage values is 0.359-0.375. Generally, the overall range of voidage is between 0.36 and 0.44 for random packing, while the range is 0.26 to 0.47 for regular packing.

$$m = 22.47 - 39.39\varepsilon \ \text{ for } \ 0.259 \leq \varepsilon \leq 0.5 \tag{2.1}$$

After generating pore size, throat size and coordination number distributions the next step is to assign them to each node. It should be noted here that, the assignment of the pore body size is random; as a result, the spatial distribution of the pore body sizes is also random. Mani et al. (1999) studied the effect of the spatial correlations of the pore sizes on two-phase flow in porous media, and concluded that spatial pore-space correlation had a large impact on inhibition capillary pressure and relative permeability curves. However, there is no direct proof that the pore bodies of naturally occurring porous medium are spatially correlated in size. In this research, the spatial pore-space correlation is not considered and all the pore sizes are assigned to the nodes in the network at random. While assigning a generated coordination number distribution to each node, the larger coordination number is assigned to bigger pore body, as observed by Markus et al. (2003) and Yanuka et al. (1986) that coordination number increases with the increase in porosity.

II.   Generate fully connected network with compressed connection matrix

After assigning all the generated parameters to all the nodes in the network, the next step is to generate a fully connected pore network. This work has is similar to that presented by

Raoof (2010). In the fully connected network, each node in the network can be connected to 26 of its nearest neighbors except the nodes at the bottom and top plane, assuming there is no in plane flow during the air sparging at the bottom and top planes. Among the 26 bonds for each node, the directions of 13 bonds are forward (up) while directions of the other 13 bonds are downwards. Then one can obtain the connection matrix, called CONMAT. Assuming N is the total number of nodes generated in the network, the size of connection matrix is N×N. In the matrix CONMAT, the column and row number represent the number of nodes, while the corresponding entry of the matrix is the direction of the bond, e.g., for CONMAT(i, j)=3, it means the direction of the bond connecting node i and node j is 3. If two nodes are not connected, the corresponding entry is 0. As each node can only be connected to at most 26 nearest nodes; hence the connection matrix CONMAT is a sparse matrix. One can use compressed sparse row (CSR) format to store the entries in the sparse matrix. This method is similar to the compression technology used by Raoof et al. (2010), hence, details not given.
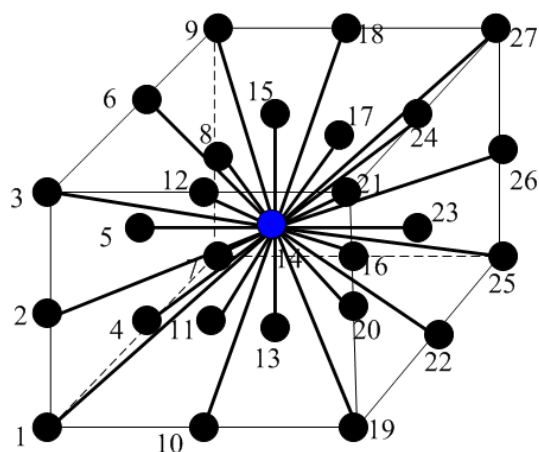
Figure 2.1 A cell of fully connected network.

III. Generate diluted bond matrix

After the first step the coordination numbers have been generated and assigned to each node. However, according to the matrix CONMAT of fully connected network stated in the second step, one can find that the coordination number of 26 is much larger than the assigned coordination number of the soil. Hence, a dilution process has to be applied to eliminate extra bonds.

Raoof et al. (2010) performed the dilution process by assigning threshold number and elimination number to each bond. The threshold number is between zero and one denoting the probability of having a bond in that direction, while the elimination number is a random number with uniform distribution. If the elimination number is greater than the threshold number, then the bond is eliminated, and vice versa. This method is very difficult to match the coordination number of each node with the assigned coordination number. Arns et al. (2004) used another algorithm which selected bond to reduce the degree of freedom of the network. This algorithm can avoid leading to many isolated bonds or clusters. Hence algorithm proposed by Arns et al. (2004) was used in this research. However, as mentioned above, the available coordination number of 26 is much larger than assigned coordination number, hence just one algorithm is not sufficient to develop reasonable network for air migration. Hence three other algorithms are proposed and total four algorithms are used in the dilution process.

1 Choose the bond with high priority

The priority of each bond can be determined by formula $p_{bij} = \dfrac{1}{1 + F(s_i)F(s_j)}$,

where $F(s_i) = 1 - n_i / a_i$, p_{bij} is the priority of bond connecting node i and j, n_i is assigned

coordination number for node i in step 1, a_i is the available number of nodes connecting node i. For example, the assigned coordination number for node i is 7, available coordination number for node i is 20, while assigned coordination number of node j is 1, available coordination number is 1, then $F(s_j) = 1 - n_j / a_j$ becomes 0, as a result, the bond between node i and node j has 100 percent of priority to be chosen. This algorithm can reduce the degree of freedom of the network.

2 Choose the bond with shortest length

3 Choose the bond connecting the larger size node

4 Choose the bond in the upward direction

For the above four algorithms, the priority of each algorithm is decreasing. The basis for last three algorithms is that: during the air sparging one air bubble is first squeezed into the nearest node; however, if two bond lengths are same, the bubble is more likely to be squeezed into the node with larger size; finally, if the available bonds have same length and node size, the bubble is more easily to be driven in upward direction due to buoyant force.

After applying dilution process, the coordination number of each node can be matched with the assigned coordination number distribution for the network.

IV. Remove isolated clusters from the network:

After the third step, it is found that although the algorithm 1 in the dilution process tries to avoid forming isolated nodes or clusters, the isolated clusters may still exist. The isolated sites and clusters may cause numerical problems since they lead to a singular or ill-conditioned coefficient matrix when calculating the permeability coefficient or other network properties. As a result, the isolated nodes or cluster should be removed from the

matrix. Raoof et al. (2010) presented a search algorithm for the isolated cluster, which is used in this research and hence details not given.

V.   Network Validation

The last step of developing the equivalent pore network is called network validation. In this step, the void ratio and permeability of the network are calculated and compared with that of the input parameters. If the differences between them are less than 5%, then the constructed network is accepted, otherwise, the pore size distribution and coordination number distribution should be generated again by adjusting the standard deviation. The calculation of permeability of the network and the validation of the constructed equivalent network will be expatiated together with the other methodology of extracting pore network from packing of spheres.

The above parts describe the complete procedures for developing the void network for air sparging. The flow chart of the whole procedure of constructing equivalent network model is shown in the Figure 2.2.
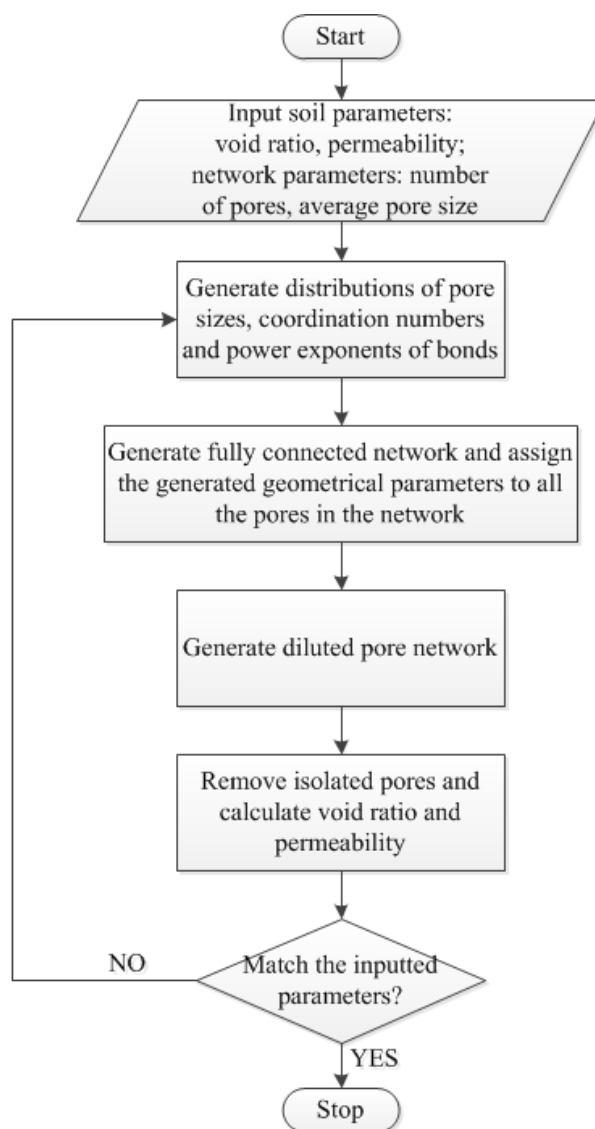
Figure 2.2 Flow chart of constructing an equivalent pore network.

It is worth to mention that, the above mentioned methodology of constructing 3D pore network can be adapted to simulate heterogeneous soil structure, e.g., two-layer soil. For this, one need to develop two independent networks and connected them at the boundary, e.g., during the simulation of multiphase flow, the output of air and water at the top of the lower layer will serve as input for the top layer. At the boundary, the mass and moment of fluids are conserved.

2.2.2 An Example of the Developed Equivalent Pore Network

In this section, an example of equivalent pore network is present. The parameters of the pore networks are shown in the following table:

Table 2.1 Geometrical Parameters of the Pore Network

Network Size	$\overline{r}$ (mm)	r_{min} (mm)	r_{max} (mm)	σ_r	n	σ_n
35-35-35	0.286	0.13	0.455	0.05	5	0.5

In table 2.1, network size is the total number of nodes contained in the network. $\overline{r}$, r_{min}, r_{max} and σ_r are the average pore size, the minimum pore size, the maximum pore size and the standard deviation of pore size distribution respectively. n and σ_n are the average coordination number and standard deviation of coordination number distribution.

The generated pore size distribution and coordination distribution are shown as follows:
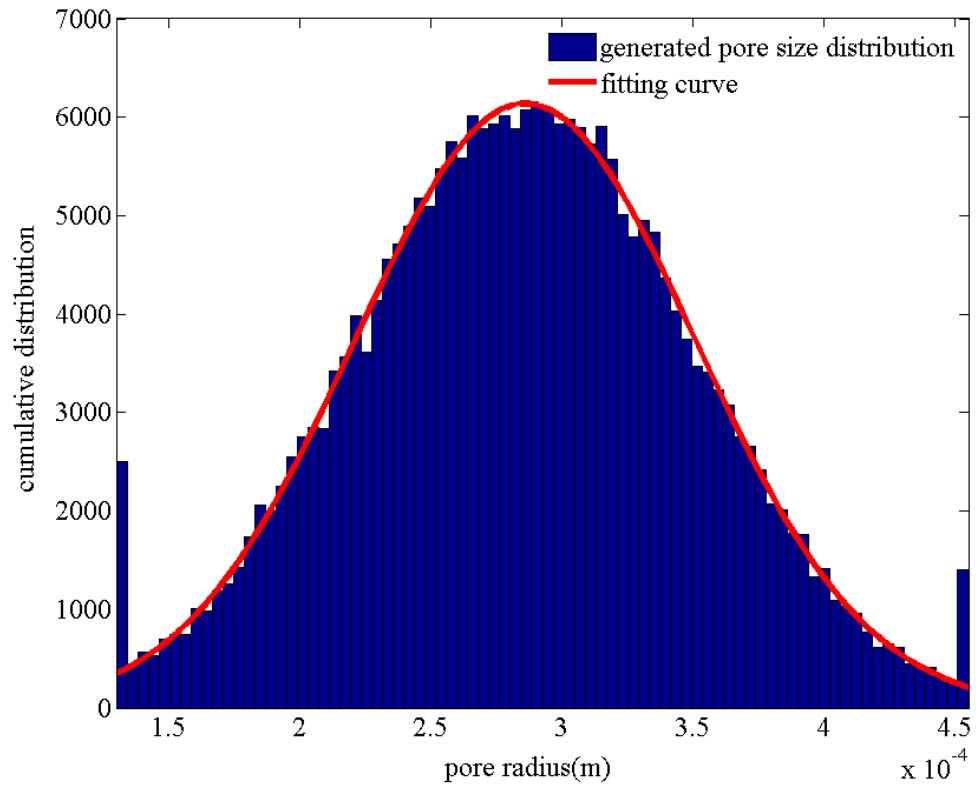
Figure 2.3 Generated pore size distribution.
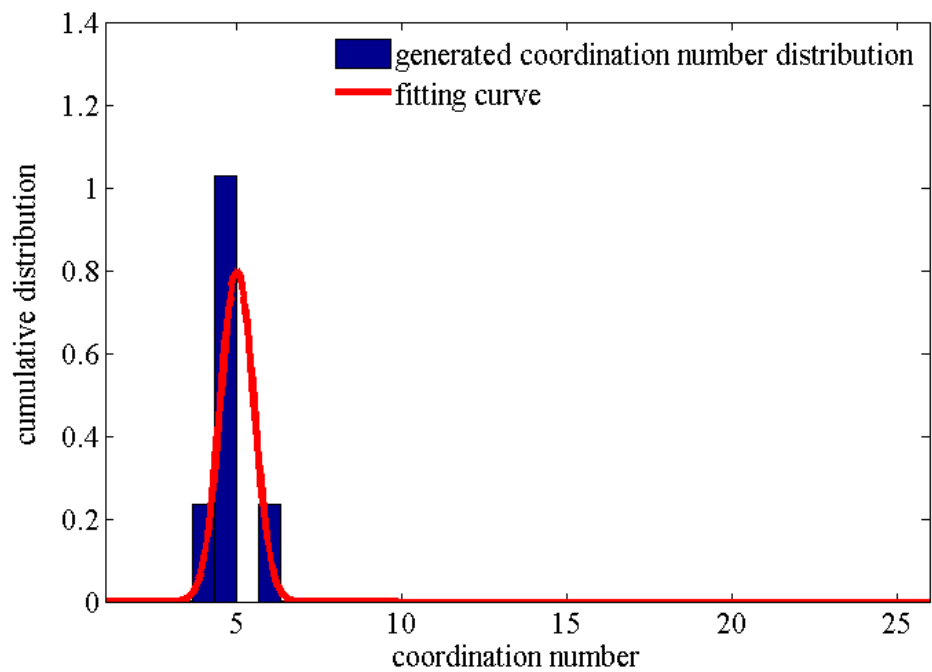
Figure 2.4 Generated coordination number distribution.

The following two figures show the generated equivalent pore network and a unit cell of the network respectively. For the visualization purpose, there are only 15*15*15 nodes shown in the Figure 2.5 instead of 35*35*35. For simplicity, the unit cell shown in Figure 2.6 has a constant coordination number of 6 for each pore. However, this is not the truth in the network shown in Figure 2.5. As mentioned above, the coordination number of each node in the equivalent pore network is not a constant and the coordination numbers of all the nodes in the network obey normal distribution.
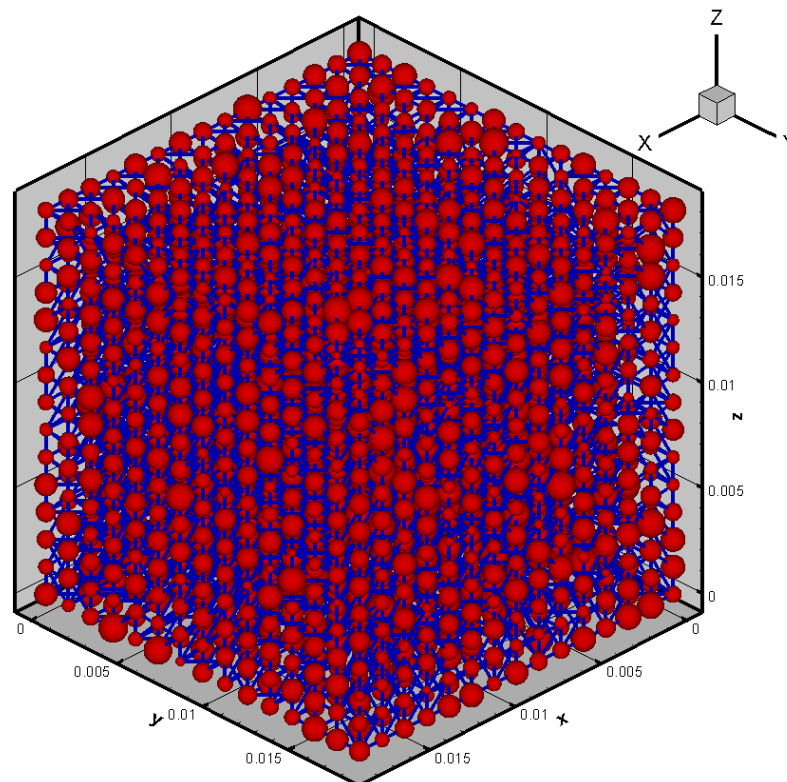
Figure 2.5 An example of constructed equivalent pore network.
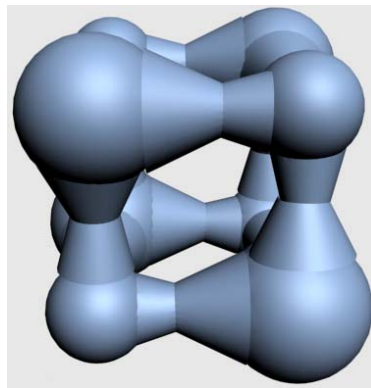
Figure 2.6 A unit cell of the equivalent pore network.

2.3   Development of Extracted Pore Network Model of Porous Medium

2.3.1   Introduction

As mentioned in the introduction part of Chapter 2, there are two ways to simulate the 3D

network of interconnected pores and throats. The first method is to directly map a specific

porous medium onto a network structure, while the second method is to create an

equivalent network using distributions of basic morphologic parameters. The fundamental

difference between the two methods is that the direct mapping provides a one-to-one

spatial correspondence between the porous medium structure and the network structure,

whereas the other type of network is equivalent only in a statistical sense to the modeled

system. In the previous section, the approach of constructing equivalent pore network

model has been presented. In this section, the approach for directly extracting the network

is presented.

The direct mapping technique requires methods of obtaining the pore structure

before the reconstruction of a network. Imaging techniques including the analysis of serial

thin section (Cousin et al., 1996, Vogel et al., 2001) and non-destructive direct imaging

techniques such as X-ray computed micro-tomography (Rintoul et al., 1996, Lindquist et al., 2000) have been widely used in constructing the pore network. Computer simulations can also be used to generate pore structure of packed beds, well-sorted sands, or certain sandstones (Riyadh et al., 2003). The use of computer-generated porous media is preferable to direct construction of networks from statistical information because one can work with more fundamental material properties (e.g., grain size distributions rather than inferred properties of the pore space) and the packing of particles can mimic the actual construction (e.g., construction of embankment dams). In this method, particles are collectively released under gravity and compacted by means of shear cycles.

There are a wide variety of sphere packing algorithms, and two primary ideas are the force-biased algorithm (Moscinski et al., 1989, 1991) and the 'drop and roll' algorithm (Jodrey et al., 1979, Vischer et al., 1972 and Jullien et al., 1987). The force-biased algorithm starts with a very dense configuration of large spheres which can even overlap while the drop and roll algorithm simulates the spheres falling under gravity sequentially and rolling to their stable position. The stable position is defined as a position where the sphere rests on three earlier packed spheres. The force-biased algorithm may not be adapted for the study of actual granular materials composing the structure, e.g., embankment, since it does not always reflect the compaction by rollers and compactors with large shear deformations and vibrations. Hence the drop and roll algorithm was adopted in this study. Once the granular media are modeled by assemblies of spheres, two partitions-Voronoi and Delaunay tessellations can be used to geometrically describe the medium. The Voronoi tessellation has long been used to characterize local arrangement in granular media (Oger et al., 1997, Yang et al., 2002), while the Delaunay tessellation

seems to be more appropriate to characterize and quantify pore volumes and pore throats for fluid flow computations (Balhoff et al., 2004, Steven et al., 1993). The Delaunay tessellation has been applied to an existing, computer-generated, random packing (Chan et al., 1988). The Delaunay tessellation subdivides the pore space into a set of tetrahedral volumes whose vertices are the centers of fours neighboring spheres as shown in Figure 2.7.
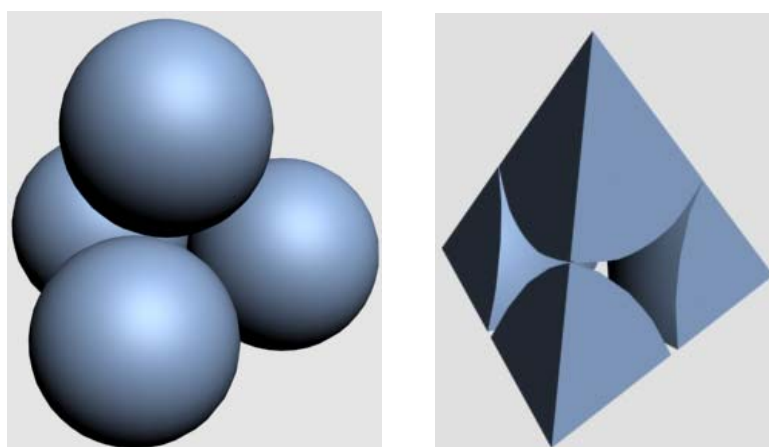
Figure 2.7 Two views of one sample Delaunay cell. Left: Delaunay cell with four composing spheres. Right: The parts of spheres located inside the tetrahedron.

The void space inside the tetrahedron represents a pore, and constrictions on each surface of the tetrahedron represent a throat. Thus each tetrahedron represents a pore with four throats emanating outward across the four surfaces. Each member of the set of pores generated using Delaunay tessellation has four neighbors (except those at the boundary), and thus has a constant coordination number of four. Adjacent pore chambers share a common triangular surface. However, the direct use of a Delaunay tessellation has two problems (Riyadh et al., 2003). First, the tessellation restricts the network to have a fixed coordination number equal to exactly four in all three dimensions. Second, it can lead to inaccurate identification of pore locations and throat sizes. Specifically, the Delaunay

tessellation tends to subdivide a single void into multiple ones. When considering a group of eight spheres packed in the form of a cube in regular cubic packing, one possible tetrahedron is made up of a sphere at one of the eight corners and the three spheres in contact with it if one insists on having tetrahedral. These three spheres do not touch one another and the corresponding constriction is actually larger than the pore. Riyadh et al. (2003) proposed a conceptually simple solution to this problem, which allows merging of multiple tetrahedrons into larger polyhedrons in cases where a single void is unnecessarily subdivided. Riyadh et al. (2003) suggested a merging criterion from the concept of the largest sphere entirely contained in the void space which can be inscribed between four spheres at the vertices of a Delaunay cell. According to Riyadh et al. (2003), the neighboring voids should be merged if the center of one void lies within a neighboring inscribed void. This merging criterion is reasonable and provides one-to-one correspondence between discrete network pores and the true voids within the packing. However, it does not consider the voids that do not meet the merging criterion but are interconnected, which should be treated differently from those are completely separated. In addition, the configurations of bonds connecting two neighboring pores are not clearly defined in their research.

In this section, different merging criteria are defined and an algorithm of directly extracting pore network from computer simulated packing of spheres is presented.

2.3.2   Methodology of Extracting Pore-Network

In this part, the main steps for directly extracting the pore network from Computer-generated packing of sphere are presented.

Step 1-Computer-simulated packed bed. For the tessellation and the network algorithm to be implemented, a complete description of a packed bed is required (consisting of sphere ID, spatial coordinates of each sphere center and the radius of every sphere in the packed bed). This can be accomplished by the computational code PFC^{3D}, a *discrete element* code. The input parameters for PFC^{3D} include dimensions of the space or box (bounded by 6 walls) to contain the particles, total number of particles to be generated (note: if the space is too small to contain all the particles, fewer particles will be created.), particle size distribution, the stiffness properties of the particles and walls, the friction coefficient and mass density of the generated particles. Then the generated particles can be deposited into a box and allow to reach equilibrium due to gravitational body forces. The PFC^{3D} can also apply dynamic motion of the spherical particles (Cundall at al., 1979). As a result, denser states can be obtained by subjecting the sample to alternating compression and extension in three perpendicular directions. In order to generate sphere packing with certain porosity, the loading/unloading cycles can be applied until the desired porosity is reached. Another simple and robust way to produce a compacted assembly with certain porosity is to start with packing of small sphere particles within a given space and then expands the radii of all particles until the desired porosity is obtained. During the expansion of the radii, all particles are allowed to move freely until they reach a state of equilibrium within a set of confining walls.

Step 2-Perform tetrahedral tessellation. This step begins with a computer-generated packing of spheres with known centroid locations and sizes of the spheres. Tetrahedral tessellation can be completed by one of the built-in functions of MATLAB 'delaunay3.m', or use the crystal growth-like algorithm presented by Chan et al.

(1988). In the later approach, a seed triangle is selected by joining the three centers of neighboring spheres. For each side of the seed triangle, identify points of sphere centers that are sufficiently close that a close-to-regular tetrahedron can be formed with the seed triangle as its base. Once a new tetrahedron is formed, the newly formed triangles are added to the list of existing triangles. Then, four faces of triangles can serve as the base of a new tetrahedron. Repeat the above steps as additional tetrahedron bases are generated. This is continued until all the sphere centers are exhausted and no more close-to-regular tetrahedrons can be formed.

After performing tetrahedral tessellation, care must be taken in dealing with the irregular cells at the boundary of the packing. Irregular cells are those with either flat or wide pore throats compared to those cells inside the packing and they may lead to singularities while searching for the largest inscribed void during the next step. In order to avoid the boundary effects, tetrahedrons formed by particles within the range of two times of the largest diameter of the particle in the packing next to the wall should be removed. At the end of the step, the ID of each tetrahedron and the radii and coordinates of the four spheres located at vertices of each tetrahedron should be recorded. In addition, for each tetrahedron, its four neighboring tetrahedrons should be also recorded, which will be used in the following steps.

Step 3 - Search for the maximum inscribed voids. This step consists of local optimization to find the largest inscribed sphere that can fit within the void space immediately adjacent to a tetrahedron. The optimization is performed using a three dimensional simplex search, modified according to the algorithm proposed by Nelder and

Mead (1965). The main steps of the optimization algorithm used to search the largest inscribed spheres are briefly summarized below:

1. For each tetrahedron, the coordinates and radii of the spheres located at the vertices of the tetrahedron and its neighboring tetrahedrons are collected.

2. Construct the initial simplex by four points (P_1, P_2, P_3, P_4) around the centroid of the four spheres which are located at the vertices of the tetrahedron. Let L_{i1}, L_{i2}, L_{i3} and L_{i4} indicate the distance between the point i and the four spheres (L_{ij} equal to the distance between points i and the sphere center j subtracting the radius of the sphere j). The function value f_i at point i is defined as $f_i = \max(L_{i1}, L_{i2}, L_{i3}, L_{i4})$.

3. Determine the worst and the best points, respectively, in current working simplex. The best point P_h (h for high) is chosen if $f_h = \max(f_1, f_2, f_3, f_4)$ while the worst point P_l (l for low) is chosen if $f_l = \min(f_1, f_2, f_3, f_4)$. Then calculate the centroid c of the best side where $c = \frac{1}{3}\sum_{i \neq l} P_i$.

4. Perform transformation of the simplex by using reflection, expansion, contraction and reduction. Try to replace only the worst vertex P_l with a better point P_l' by using reflection, expansion or contraction with respect to the best side. For each operation make sure that the line joining P_l' and the vertices of the tetrahedron should not pass through any neighboring spheres. If so, the new point will be accepted and becomes the new vertex of the working simplex, otherwise, this process will be considered failed and the new point will be rejected.

5. Repeat steps 2 to 4 until the termination test is satisfied. Here, the termination test can be the function-value convergence test. It becomes true when all four function

values f_1, f_2, f_3, f_4 are close.

6. Return the best vertex of the current simplex and the associated function value, which are corresponding to the pore center of the largest inscribed sphere and its radius. It is noted here that the existence of relative flat tetrahedrons next to the wall will lead to very large inscribed sphere; as a result, at beginning of this step, the tetrahedrons next to the walls should be removed to avoid the boundary effect as mentioned in the last step.

Step 4 - Check the interconnectivity between two neighboring voids. After tetrahedral tessellation, for each tetrahedron, its four neighboring tetrahedrons have been recorded. After locating the maximum inscribed voids for each tetrahedron, one void can be obtained (the void is not necessary to be confined in the tetrahedron) with radius and coordinates of its geometrical center. During this step, for two connected tetrahedrons, the interconnectivity of the two voids belonging to the two neighboring tetrahedrons will be checked. Before checking the interconnectivity between two neighboring voids, three levels of interconnectivity between two voids are defined. Given two neighboring pores: pore i and pore j, with pore radii of r_i and r_j, respectively, d_{ij} is the distance between two pore centers. For level 0, $d_{ij} \geq r_i + r_j$, the two pores are separately; for level 1, $abs(r_i - r_j) \leq d_{ij} < r_i + r_j$, the two pores are interconnected, by one center of pore is not included in the other the pore; for level 2, $d_{ij} < abs(r_i - r_j)$, two pores are interconnected and the center of one pore is included in the other one. For interconnectivity of levels 0 and 1, the two pores are considered connected by bond, and the throat size of the bond will be given in the next step. For interconnectivity of level 2, two pores can be merged into one pore. The definitions of the three levels of interconnectivity are shown in Figure 2.8

Level 0   Level 1   Level 2
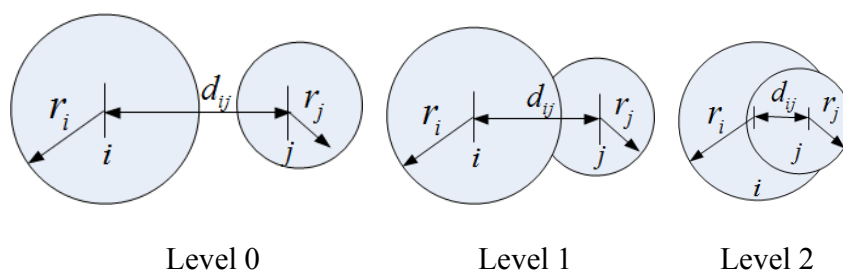
Figure 2.8 Definitions of the three levels of interconnectivity.

Step 5 - Determine the throat size and parameters for defining the bond. Throat size is the narrowest part that connects two neighboring pores. As the vertices of each tetrahedron are at the spheres center during tessellation, the void projected onto each of the four faces is necessarily the smallest constriction that will be encountered when traversing a passage into the central pore. There are about three types of throats after tetrahedron tessellation, as show in Figure 2.9.

Level 0   Level 1   Level 2
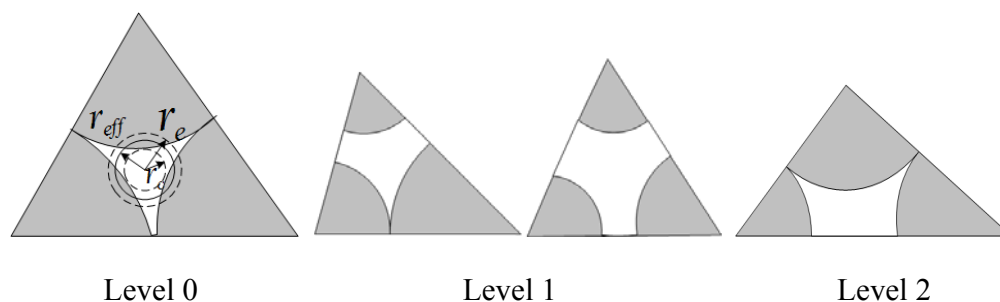
Figure 2.9 Three types of throats for different levels of interconnectivity.

Figure 2.9 shows that spheres forming the constriction between two voids do not necessarily touch. However, after steps 3 and 4, the throat shown in Figure 2.9 may not be accurate. During step 3, a new void may be defined which is different from that defined as the void space inside each tetrahedron, as a result, the position and size of the throat may also be changed correspondingly. For two voids with interconnectivity level 0, the throat size defined in this step is the same as that is defined in step 2, however, for the

interconnectivity level of 1, as the voids belonging to two neighboring are intersected, the throat size are different from that defined before, which needs to be recalculated in this step. In the following sections, the calculation of the throat size and description of the bond for the all levels of interconnectivity are presented.

For level 0, (the two voids are completely separated), the throat is the projection of the void on the tetrahedron's face, as shown in Figure 2.9. Then the throat size is equal to the effective radius of the void shown in Figure 2.9 and the effective radius is defined as follows: the radius of a hypothetical cylindrical tube which haves the same hydraulic conductivity as that of the conduit with cross section shown in Figure 2.9. It is denoted as 'effective radius' r_{eff}. As the cross section shown in Figure 2.9, it is in an irregular shape. In order to calculate the hydraulic conductivity of it, the Navier-Stoke equation can be applied with no slip boundary condition and solved using the finite-element method as performed by Karsten et al. (1997) and Steven et al. (1993). Finally, by comparing the hydraulic conductivity of the two conducts, the effective radius can be calculated. According to Steven et al. (1993), the effective radius r_{eff} is quite close to the arithmetic mean of r_c, which is the radius of the largest inscribed circle of the irregular cross section and r_e, which is the radius of the 'equivalent circle' having the same total area as the irregular cross section.

The next step is to determine the geometrical parameters of the bond. Here, a bond is defined as the passage connecting two neighboring pore voids and the throat is the narrowest part of the bond. In order to study the geometrical properties of the bond, the geometrical properties of pore space in the packing should be described.
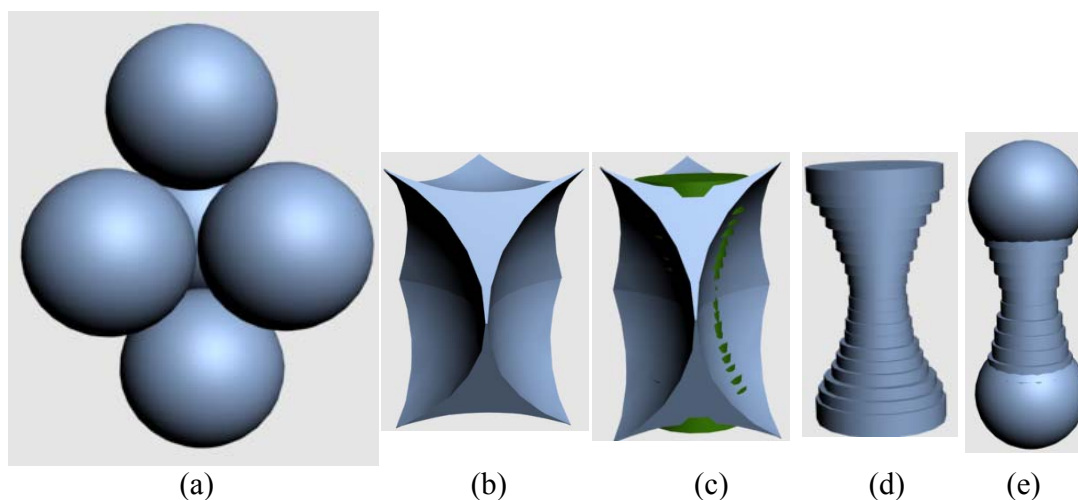
Figure 2.10 Extracted bond between two neighboring pores: (a) packing of spheres; (b) pore space formed in the packing; (c) pore space with inscribed circular disks; (d) inscribed plates in the pore space; (e) proposed expression of the pore space

Figure 2.10(b) shows the extracted pore space from cubic close packing of four particles as shown in Figure 2.10(a). It should be noted here that the size and shape of the two ends of Figure 2.10(b) are not correct for describing the real space in the packing, as it did not consider other connections to the pore. From Figure 2.10(b), it can be easily observed that the pore space is an irregular shape and the cross sections of the pore space are arbitrary. In addition, the cross-sectional area of it is not a constant. In order to obtain additional information about the pore space, it is divided into 'n' segments and each segment is replaced by an inscribed circular disk with thickness 1/n of the height of the extracted space. This process is shown in Figure 2.10(c), in which the pore space is divided into 25 segments. Finally, after removing the extract part of the pore space, the approximated shape of the space is obtained as shown in Figure 2.10(d). Here, one may argue that the using of inscribed radius may underestimate the conductivity of the bond as the cross-sectional area is larger than that, however, the main purpose of demonstration of

this process is not to determine the dimensions of the bond, but to check the equivalent profile of the bond and to find an approximate mathematical expression for it.

From Figure 2.10(d), it can be stated that the pore space converges and then diverges. Two approaches can be used to deal with the pore space. Approach 1 is to consider the whole pore space shown in Figure 2.10(d) as a bond and there will be no volume assigned to the 'pore body'. However, this will result in the problem of double-counting the volume of the two ends of the bond, as each 'pore body' is supposed to connected to more than one neighboring 'pore body'. Approach 2 would be to replace the two ends of the pore space with two pore spheres as shown in Figure 3e. Then the pore space contains two parts: pore bodies and bond. In Figure 2.10(e), the spheres represent pore body while the bond is the part connecting the two pores. The volume and center of the pore body can be determined by finding the inscribed spheres of the packing as shown in Figure 2.10(a).

In this manuscript, the second approached is used. The size of pore body can be determined from step 3 and two power functions are used to define the shape of the bond as shown in Figure 2.11.

(a) (b)
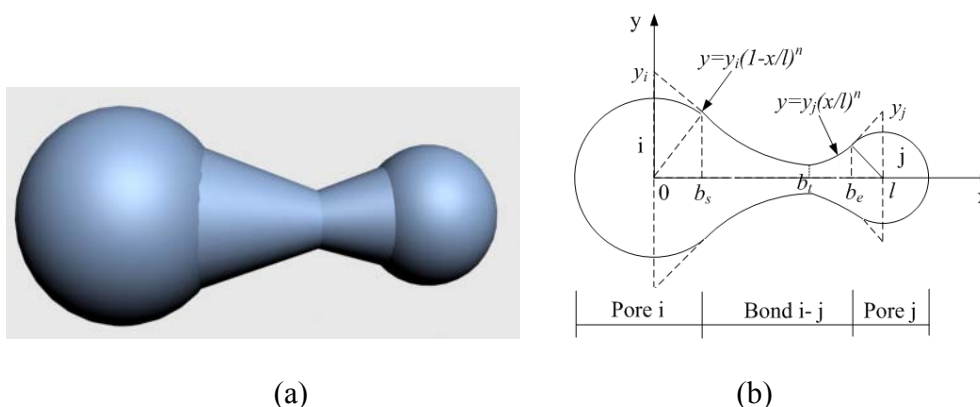
Figure 2.11 Approximate expression of the bond for interconnectivity of Level 0.

This type of bond is known as Biconical abscissa Asymmetric CONcentric (BACON) bond (Acharya et al., 2004). As shown in Figure 4b, the bond between node i and node j is composed of two parts: the left part (from b_s to b_t) and the right part (from b_t to b_e), where b_s and b_e are the starting position and ending position of the bond, respectively while b_t is the position of the throat in the bond. Each part of bond is formed by rotating smooth curves around the x axis. Each curve is tangent to its adjacent pore body and can be expressed by two simple power functions. The left curve can be expressed by $y = y_i(1 - x/l)^n$ while the right part can be expressed by $y = y_j(x/l)^n$, where x is the distance from the center of pore body i; l is the pore spacing between the pore i and j; y_i and y_j can be determined by the point of tangent between the curve and the pore body and 'n' is called power exponent, which determines the shape of each curve. As the position and size of throat have been determined before, by knowing the coordinates and radii of the two pore-bodies, all the parameters of the bond can be easily determined. There are at least two advantages for using this power equation to describe the bond: First, it is easy to obtain the analytical solutions for the conductivity of the bond by using this flow profile. As a result, it will offer an easy and rapid way of considering the flow properties of fluid in the network if the required precision of the problem is not too high. At same time, as radius of each section of the real bond, which is in arbitrary shape, is represented by its inscribed circular radius. It also allows for further improvement of this flow profile of the bond to obtain predicted results higher accuracy. Second, by using the power function to express the flow profile the position and size of the throat is correlated to both the pore size and the pore spacing.

For level 1, the two pore bodies are connected by a cylindrical bond as shown in Figure 2.12.
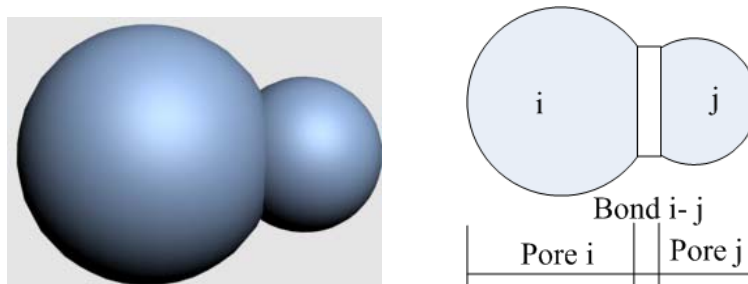
Figure 2.12 Approximate expression of the bond for interconnectivity of Level 1.

The radius of the cylindrical bond is equal to the radius of the common cross section between the two spheres, which can be calculated based on the radii of the two spheres and the pore center distance. The length of the cylindrical bond can be considered as very small, e.g. 1/10 of the radius of smaller ball between the two spheres.

For level 2, the two voids should be merged together. After imposing the merging criterion, multiple voids become merged together, and the resulting pores may be polyhedrons with essentially arbitrary shapes.

The schematic flow diagram of extracting pore network from computer simulated packing of sphere is shown in Figure 2.13.

```
                    ┌──────────────┐
                    │    START     │
                    └──────┬───────┘
                           │
                           ▼
    ┌─────────────────────────────────────────────────────────┐
    │ Generate compute simulated packing of spheres, and record │
    │ information of ID, coordinate and radius of each sphere   │
    │ in the packing                                            │
    └─────────────────────────────────────────────────────────┘
```

Generate compute simulated packing of spheres, and record information of ID, coordinate and radius of each sphere in the packing

Perform tetrahedral tessellation; for each tetrahedron, record the IDs of the four spheres located at the vertices of the tetrahedron and IDs of spheres belonging to its four neighboring tetrahedrons

Perform local optimization to search for the maximum inscribed void for each tetrahedron (except for the tetrahedrons at the boundary)

Determine and record the level of interconnectivity between two voids

According to the interconnectivity level between two neighboring voids, merge the voids with interconnectivity of level 2

Are there any voids merged?

YES

NO

Determine coordination number for each void, calculate parameters for defining the bond shape and throat size; report the information of all the voids and bonds

STOP

Figure 2.13 Flow chart of extracting pore network from computer simulated packing of spheres.

2.3.3 An Example of Extracted Pore Network

An example of the extracted pore-network from packing of spheres is presented in Figure 2.14. In Figure 2.14, the packing of 3000 spheres with diameter of 2 is generated by software PFC^{3D} and the pore network is extracted using the above algorithm. Figure 2.15 shows the largest void in the network which is formed by imposing the merging criterion. The void size distribution and coordination number distribution of the extracted network is shown in Figure 2.16. The last two graphs in Figure 2.16 are the distribution of pore center distance and distribution of back calculated power exponent used to define the shape of the bond as shown in Figure 2.11. As shown in Figure 2.16, the pore size distribution and coordination number distribution obey normal distribution while the power exponent distribution obeys exponential distribution as shown by the fitting curves in the graphs. In addition, the pore center distance is not constant as assumed in most lattice based network. All these information are helpful to the construction of equivalent network to be presented in the next section.
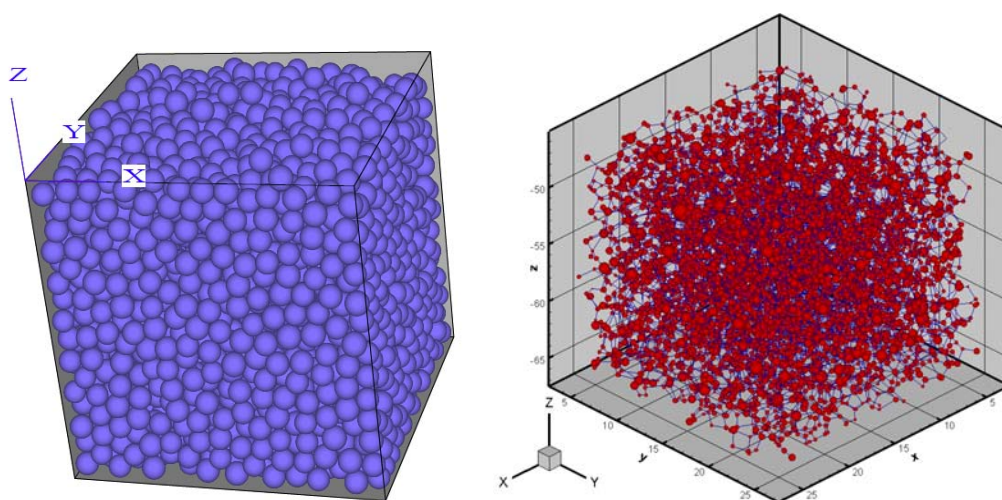
Figure 2.14 Packing of spheres and extracted pore network.
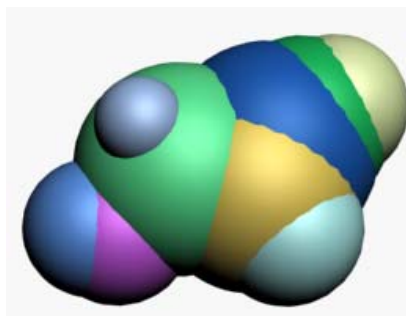
Figure 2.15 A void formed by merging multiple neighboring voids.
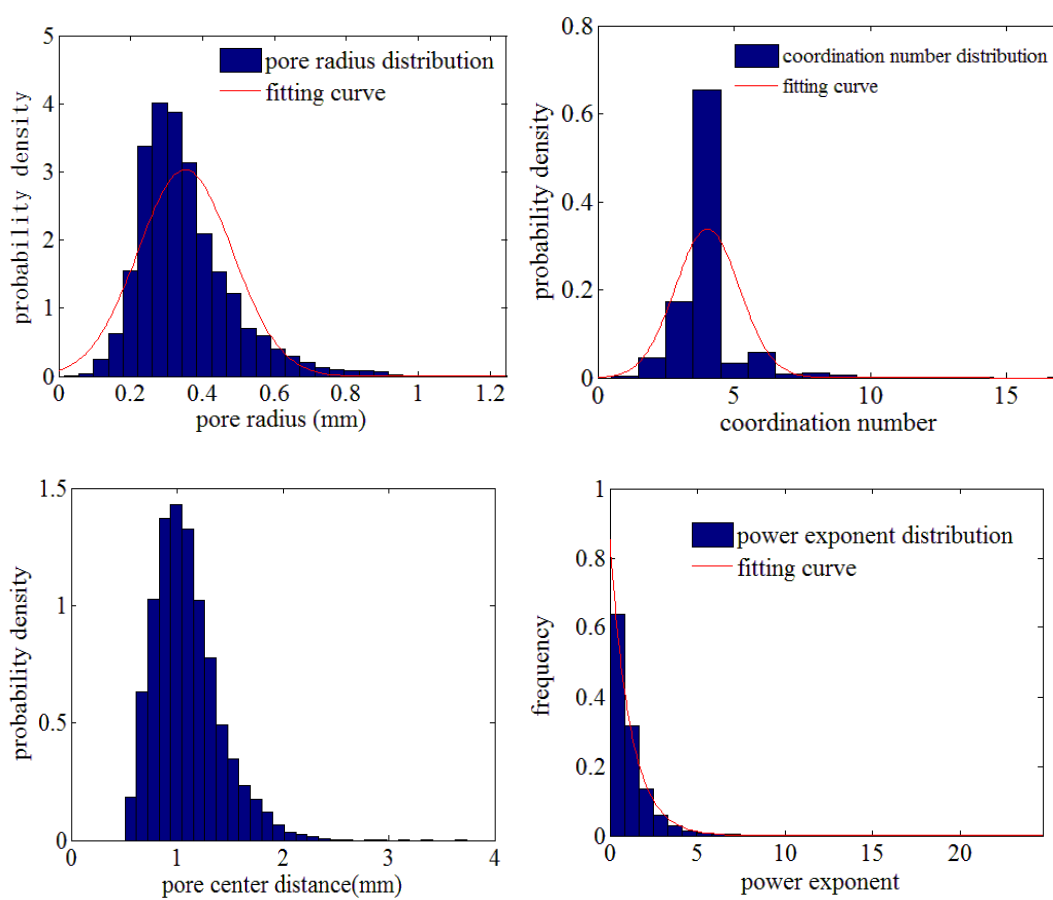
Figure 2.16 Obtained geometrical and topological information of the pore network.

2.4 Geometrical and Topological Characteristics of the Pore Space

2.4.1 Introduction

As mentioned in the Section 2.2 that the most critical part in constructing a pore-network model is defining its structure and geometry, i.e., the locations of pore bodies, pore-body size distributions, throat-body size distribution, pore connectivity, and the spatial correlation between pore bodies and pore throats (Celia et al. 1995). Generally，typical parameters required for the creation of an equivalent network include pore body and pore throat size distributions, coordination number distribution, spatial correlation between adjacent pore bodies, and spatial correlation between pore throat size to pore body size known as aspect ratio. Usually during the construction of equivalent pore network, the pore size and throat size distribution are generated based on probability density functions, which are normal distribution, log normal distribution or Weibull distribution, and a common assumption in network model construction is that pore sizes are independently distributed upon the network lattice. The space between two neighboring pore centers is identical for the whole network, but can be adjusted to fit experimental porosity (Mattews et al., 1993, 1995). However, during the construction, the spatial correlation between pore body and throat or pore body to pore body have not been clearly considered, but it has drawn attentions of many researchers (Rajaram et al., (1997), Mani and Mohanty (1999)). Mayagoitia et al. (1985, 1997) considered the correlation between pore size and throat size by applying the construction principle that any pore is always greater than or at least equal to the size of any throat that is connected to it. During the construction, the pores and throats size distributions can follow independent normalized distribution functions. After initial random size distribution, there are pores that do not satisfy the construction principle

and one way to overcome this deficiency is to use Markovian transformations (Riccardo et al., 1997, Kornhauser et al., 1997) until an "equilibrium" distribution is reached in whole network, which is called weak correlation. The strong spatial correlation between pore-body and pore-throat size have also been considered by many other researchers (Chatzis and Dullien, 1985, Wardlaw et al. 1987, Diaz et al. 1987, Markus et al. 2003). In these researches, it is assumed that large pore bodies were connected to large pore throats and small pore bodies to small pore throats. For that, they first assigned random radii to the pore bodies and make sure the pore bodies did not overlap each other; then generated the pore-throat sizes without assigning the values to the pore throat. For each pore throat, determine the mean size of the adjacent pore bodies and assign sizes to the pore throats by assuming an increasing monotonic relationship between the pore throat size and the main adjacent pore body size. Although there is no consistent approach on dealing with the spatial correlation between pore body and pore throat, the importance of spatial correlation to pore scale simulation of single phase or multiphase flow has been realized by many researcher. Tsakiroglou and Payatakes (1991) studied the effect of spatial correlation on simulations of mercury porosimitry curves. They found that pore body-throat correlations are significant and affect the shape of the pressure saturation curve where it becomes more gradual. Three types of network were used: uncorrelated, body-throat correlated, and body-body and body-throat correlated. They found that body-body and body-throat correlated networks strongly affect mercury intrusion curves. Bryant et al. (1993) also showed the importance of the spatial correlation between pore sizes in a network constructed from simulated random close packing with uniform spheres. They examined the effect of correlation on permeability by comparing predictions of correlated and

randomly distributed networks. They found that incorrect permeability predictions were obtained when the pore size distribution is assigned randomly to throats in the network.

Equally important to the geometric properties are the topological properties of the pore space which are the connection patterns of the pores and have a significant influence on many single and multi-phase parameters such as pressure-saturation curves, phase distributions and interfacial area ((Lowry and Miller, 1995). Most of the previous network models studied in three dimensions have been limited to regular cubic lattice with connectivity of six or smaller (Dixit et al. 1998; Fenwick and Blunt 1998 and Dixit et al, 1999). However, the connectively can be larger than six and follows nonuniform distributions (Kwiecien et al., 1990). For example, Oren and Bakke (2002) developed a process-based reconstruction procedure which incorporates grain size distribution and other petrographical data obtained from 2D thin sections to build network analogues of real sandstones. They reported average coordination number of 3.5-4.5 and while the majority of pores were 3-connected, some pores displayed more than 15 connections. Arns et al. (2004) studied the role of topology on drainage relative permeabilities derived from network models. They found that relative permeabilities calculated for the equivalent sandstone networks cannot be reproduced by regular networks or stochastic networks which have the same geometric properties, but which only match the average coordination numbers of the equivalent rock networks. However, they found that relative permeability curves computed on stochastic networks which match the full coordination number distribution are in reasonable agreement with those for the imaged rock networks. Further, they also found that distorted and regular lattices with the same coordination number distribution produce similar relative permeabilities.

According to the brief review of the current research on construction of pore network model, it can be concluded that the main challenge in development of the structure of a pore network is to preserve essential features of the void space. Generally, the major characteristics of a pore space are its geometric properties and topological properties. In practice, measurements of the microstructure of a porous medium are usually limited to images of void space in two-dimensional sections and to the pore entry sizes given by mercury porosimetry. These data are insufficient to allow construction of an exact network replica of the porous medium (Bryant, 1993). In the previous section, a new approach of extracting pore network from packing of spheres has been proposed, so in this section, the main geometrical and topological characteristics of the void space in the random packing of equal size particles are studied by the proposed algorithm.

2.4.2 Extracting Geometrical and Topological Information of Void Space

(1) Computer Simulated Packed Bed

In this research, the analysis of void space is performed on a numerical packing composed of 3,500 rigid spheres deposited under gravity in a parallelepipedal box. Particles are collectively released under gravity and compacted by means of shear cycles. This can be accomplished by computational code PFC^{3D}, a discrete element code, which was used to assess the dynamical motion of the spherical bodies (Cundall et al. 1979). Sphere packing algorithms is 'drop and roll' algorithm (Jullien, 1987) which simulates that the spheres fall under gravity sequentially and roll to their stable position. The stable position is defined as position when the sphere rests on three earlier packed spheres. The input parameters for PFC^{3D} include size of the space to contain the particles, total number of particles to be generated (note: if the space is too small to contain all the particles, fewer particles will be

created.), particle size distribution, the stiffness properties of the particles and walls, the friction coefficient, and mass density of the generated particles. In this study, 3500 equal size particles with radius of 1 unit were packed in the space of 30*30*30. Particle density is equal to 2,500 kg/m³, $k_n = k_s = 108$ N/m and friction coefficient f is set to 0. Firstly, the generated particles can be deposited into a box and allow to reach equilibrium due to gravitational body forces. Then vertical load was applied on the top plane of the box and the porosity of 0.424 was obtained for the packing. The packed bed is shown in Figure 2.17.
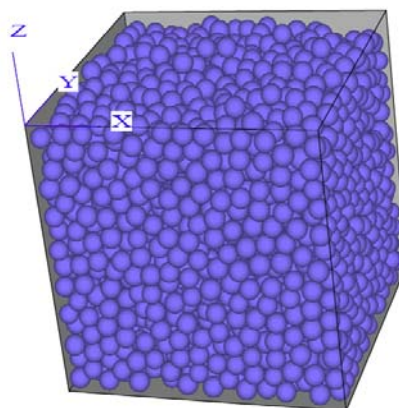
Figure 2.17 Computed generated packing of spheres.

(2) Modified Delaunay Tessellation

The Delaunay tessellation can be implemented very easily based on a complete description of a packed bed (consisting of an array containing the x, y and z coordinates and the radius of spheres in the packed bed) obtained from computer-generated packing of spheres. In order to avoid the boundary effects, the particles located within the range of two times of the diameter of the particle in the packing to the wall were removed. After performing tetrahedral tessellation, care must be taken in dealing with the irregular cells at the boundary of the packing. Irregular cells are those with either flat or wide pore throats compared to those cells inside the packings and they may lead to singularities while

searching for the largest inscribed void. Finally, there are a total of 11,110 tetrahedra. For each tetrahedron, one largest inscribed sphere can be found by modified Nelder-Mead Method. This step consists of local optimization to find the largest inscribed sphere that can fit within the void space immediately adjacent to a tetrahedron. The optimization is performed using a three dimensional simplex search, modified according to the algorithm proposed by Nelder and Mead (1965). The boundary condition of the modified Nelder-Mead method is that the largest inscribed void should not be interconnected with all neighboring spheres in the packing.

(3) Throat Size and Coordination Number Calculation

By using modified Nelder-Mead Method, the maximum inscribed voids for each tetrahedron can be found. In order to calculate the throat size and coordination number, the interconnectivity between two neighboring voids should be checked. Three levels of interconnectivity between two voids are defined in this research. Given two neighboring pores: pore i and pore j, with pore radii of r_i and r_i, respectively, d_{ij} is the distance between two pore centers. For level 0, $d_{ij} \geq r_i + r_j$, the two pores are separately; for level 1, $abs(r_i - r_j) \leq d_{ij} < r_i + r_j$, the two pores are interconnected, by one center of pore is not included in the other the pore; for level 2, $d_{ij} < abs(r_i - r_j)$, two pores are interconnected and the center of one pore is included in the other one.

For the interconnectivity of levels 0, two adjacent pores are considered separated and connected by bond between them. The throat, which is the narrowest part that connects two neighboring pores, is the void projected onto each of the four faces. The two main types of throat as shown in figure 2.18.
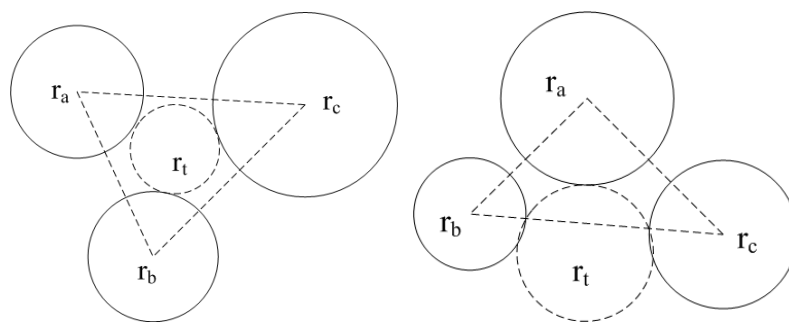
Figure 2.18 Two types of throats for interconnectivity of level 1 (type 1, left and type 2, right).

For the type 1, the throat size is equal to the radius of the inscribed circle shown in Figure 2.18. It can be calculated by using iterative numerical methods. However, for the type 2, the radius of the inscribed circle cannot be considered as the throat size any more, it is much larger than the throat size. So in this research, the throat size for type 2 is equal to the equivalent radius of the void area confined in the triangle shown in Figure 2.18.

For the interconnectivity level of 1, the two neighboring voids are intersected and the throat size is the radius the interface between two spheres as shown in Figure 2.19 (1). However, if one void is connected to more than one neighboring voids, some interfaces may be interconnected with each other as shown in Figure 2.19 (2). This situation is very complicate and it is not considered in this research.

(1)   (2)
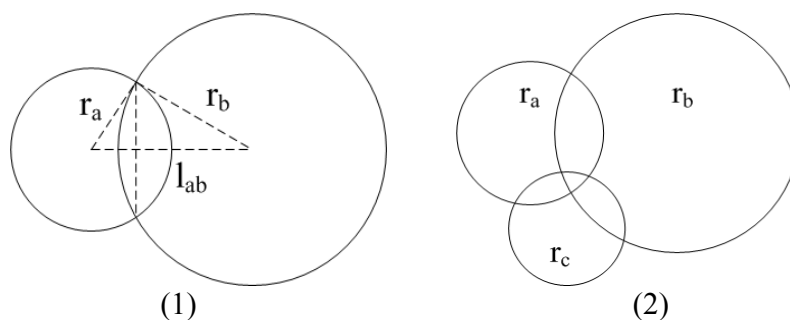
Figure 2.19 Throats for interconnectivity of level 1.

For the interconnectivity level of 2, two pores are merged into one pore. So there is no throat inside the merged void. However, as the two pores are merged into one pore, the size of the merged void should be recalculated. This also becomes complicate if multiple voids become merged together, and the resulting pores may be polyhedrons with essentially arbitrary shapes. In this case, if more than two voids are merged, firstly, the common volume between two the closest voids can be found, and then the equivalent radius and the volume of the merged void can be calculated by using the total volume subtracting the sum of common volumes.

For the coordination number calculation of each void, it is equal to the number of the connections of each void with its neighboring voids at interconnectivity level of 0 or 1.

2.4.3   Results and Discussion

3500 equal size spheres (radius of 1 with arbitrary unit) are packed by the software PFC^{3D} and the porosity of packing is 0.424. In order to eliminate the boundary effect of the packing, the particles located within the range of two times of the diameter of the particle in the packing to the wall are removed. After performing tetrahedral tessellation, there are a total of 11110 tetrahedra. For each tetrahedron, one largest inscribed sphere was found by modified Nelder-Mead Method. Finally, after performing merging criteria, the 3D pore network can be obtained and is shown in Figure 2.20.
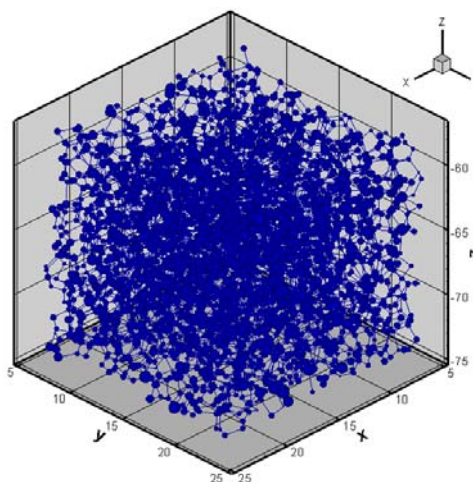
Figure 2.20 The extracted pore network.

The geometrical properties of this random packing are presented as follows, including pore size distribution, throat size distribution, pore size ratio between two neighboring voids, throat size to pore body size ratio (also known as aspect ratio), pore center distance distribution, and topological properties of the random packing including coordination number distribution, and correlation between coordination number and pore size.

1 Pore size and neighboring pore size ratio

Figure 2.21 shows the pore size distribution for the random close packing. In order to find the spatial correlation between adjacent pore bodies, the pore size ratio between two neighboring pores are calculated and plotted in Figure 2.22. In Figure 2.22, the pore size ratio is calculated as the larger pore size divided by the smaller pore size.
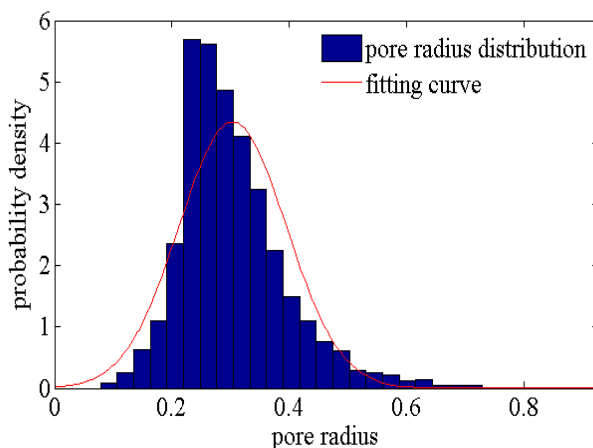
Figure 2.21 Obtained pore size distribution.
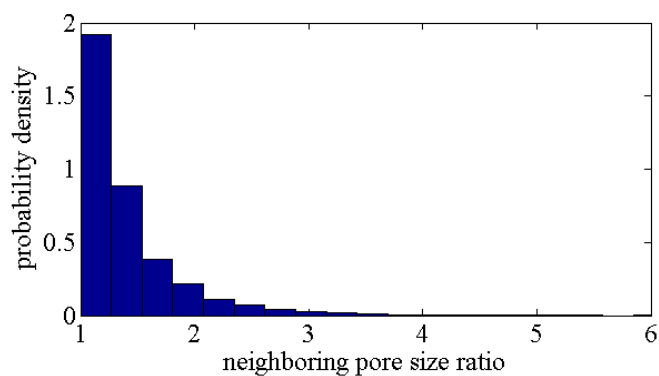
Figure 2.22 Obtained neighboring pore size ratio.

In Figure 2.21, it can be clearly shown that the pore sizes obey normal distribution. The fitting curve of the pore size distribution shown in Figure 2.21 is normal distribution with average of 0.31 and standard deviation of 0.092. In Figure 2.22, it can be found that the majority of neighboring pore size ratios fall in the range of 1~2 although the neighboring pore size ratios are not constant. So when assigning the generated pore size distribution to pore network during the construction of pore network, this principle should be considered. To further consider the spatial correlation between two neighboring voids,

neighboring pore ratio is plotted against average of the two adjacent pore sizes as shown in Figure 2.23.
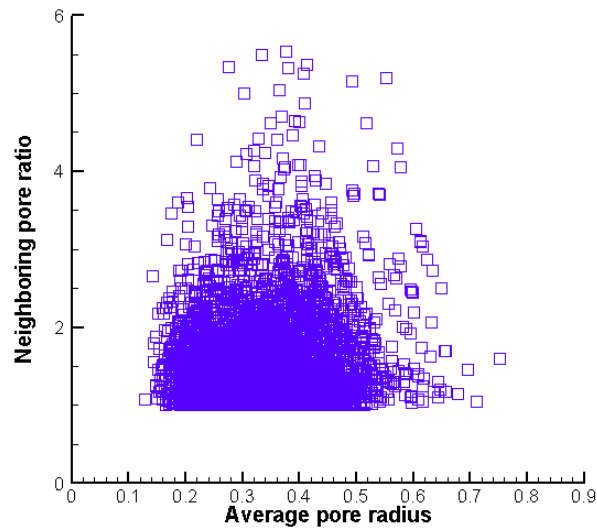
Figure 2.23 Correlation between neighboring pore size ratio and average pore radius.

From Figure 2.23, it can be observed that there is no strong correlation between the neighboring pore ratio and average pore size.

2 Throat size and aspect ratio

In this part, the throat size distribution and the ratio between throat size and the average pore size of its two neighboring pores are presented in Figure 2.24 and Figure 2.25, respectively.
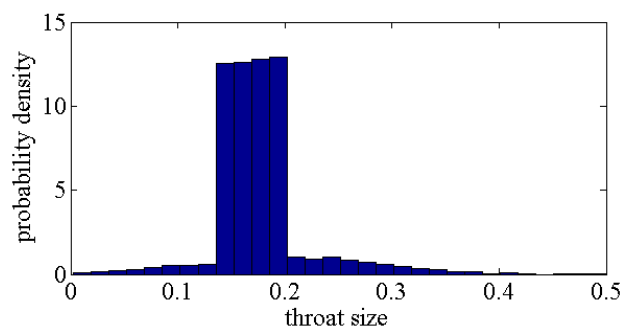
Figure 2.24 Obtained throat size distribution.
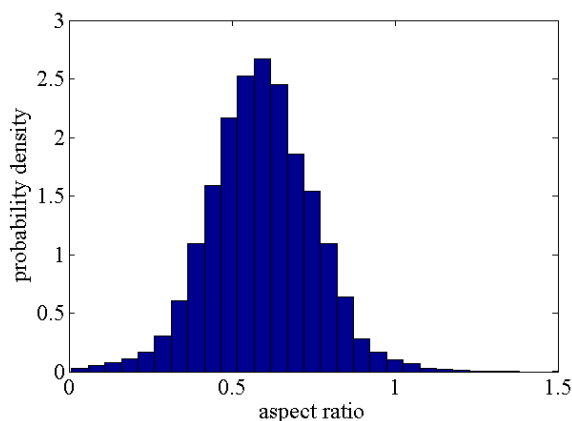
Figure 2.25 Obtained aspect ratio distribution.

From Figure 2.24, it can be found that the range of throat sizes is very wide, however, it mainly falls into the range of 0.15~0.2. As shown in Figure 2.25, the aspect ratio is not constant and its distribution obeys the normal distribution. It should be noted here that in Figure 2.25, some aspect ratios are larger than 1 and there are two possible reasons accounting for this result: firstly, the aspect ratio is defined as the ratio between throat size and the average of its neighboring pore sizes. So it is possible to have throat size larger than the averaged pore size; secondly, as mentioned above, when calculating the throat size for some flat tetrahedron with interconnectivity of level 0, the throat size is the equivalent radius of the total pore cross sectional area. The calculation of this type of throats might introduce some large throat size. However, for the flat tetrahedra, usually the interconnections between two pore bodies are of the level 1 or 2 (two pore bodies are intersected), as a result, only small part of aspect ratios are greater than 1 as shown in Figure 2.25. In order to find the spatial correlation between aspect ratio and pore size, the aspect ratio is also plotted against average pore size as shown in Figure 2.26. From Figure 2.26 it can be concluded that there are no strong correlation between aspect ratio to average pore size. However, it is clear that small pore size tends to have high aspect ratio.
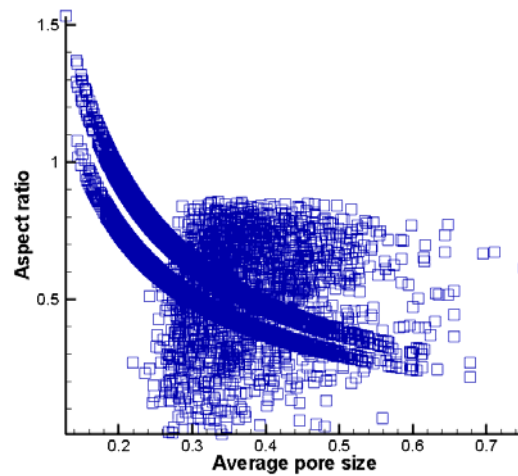
Figure 2.26 Correlation between aspect ratio and average pore size.

3 Pore center distance (pore spacing)

As mentioned above, for regular 3D pore network, the spacing between two adjacent pore centers is same for the whole network. To check how accurate this assumption is, the distribution of pore center distances is plotted in Figure 2.27. From Figure 2.27, it is obvious that the pore center distance is not constant as assumed in most lattice based network and it has a wide range from 0.5 to about 2.2. To further study on this point, the distorted pore network is suggested to be used and compared with lattice based network.
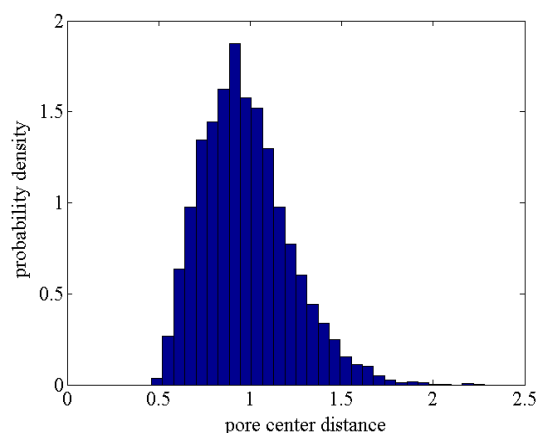
Figure 2.27 Obtained pore center distance distribution.

4 Coordination number distribution

Figure 2.28 shows the coordination number distribution of the extracted pore network. It can be observed from Figure 2.28 that the coordination number of the network is not constant as those obtained by tetrahedron tessellation. It approximately obeys normal distribution. In order to find the correlation between pore size and coordination number, the coordination number is plotted against the pore size as shown in Figure 2.29.
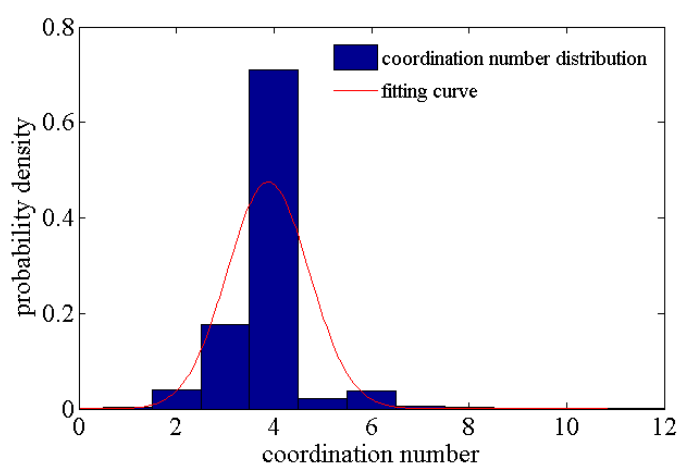
Figure 2.28 Obtained coordination number distribution.
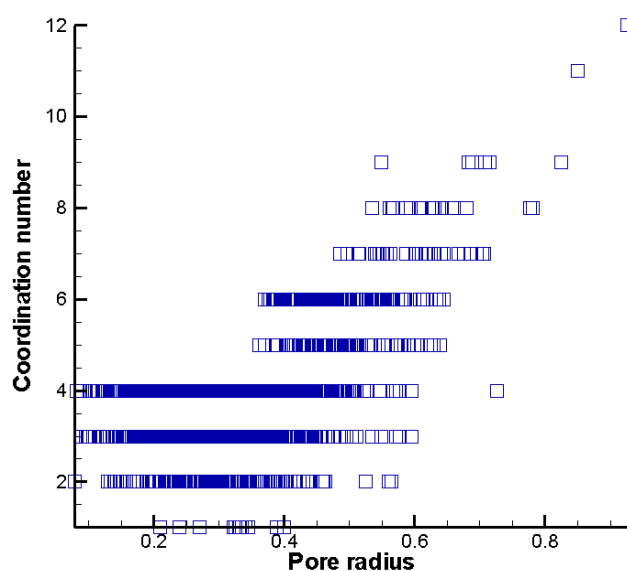
Figure 2.29 Correlation between coordination number and pore size.

From Figure 2.29 it can be found the trend that the coordination number increases along with the increase of pore size. It suggests that the larger coordination numbers should be assigned to larger pores when we assign the generated coordination number to each pore. However, this is no strong correlation between the coordination numbers and pore radii.

2.4.4 Conclusions

A systematic study of the geometrical and topological properties of pore space of a random packing of equal spheres is provided in this section. Some preliminary results can be summarized as follows: as to the geometrical information of the pore space, its pore body size distribution obeys normal distribution and the neighboring pore size ratios are not constant but mainly fall in the range of 1~2. There is no strong correlation between neighboring pore size ratio and pore radius. As to the throat size distribution, it has wide ranges; however, the majority of them fall in a narrow range. There is a weak correlation between aspect ratio and pore body size. In addition, it is found that the pore center distance is not constant and it obeys a normal distribution. For the topological information, the coordination number has a wide range and it obeys a normal distribution. There is a relative strong correlation between coordination number and pore size that larger pores tend to have higher coordination numbers. All these observations are the basis for the accurate construction of 3D pore network model.

2.5   Validation of the Two Types of Pore Networks

2.5.1   Direct Validation of the Extracted Pore Network

The algorithm of directly extracting pore network can be validated by comparing the extracted pore network from a regular packing, of which the pore size distribution and coordination number distribution can be easily obtained with the actual geometrical and topological information of the voids in the packing. Cubic packing was chosen for this purpose and it has known pore radius of $0.366d$ (d is the diameter of each particle), throat size of $0.207d$ and average coordination number of 6. In the simulation, 125 equal size balls with radii of 0.5mm were used in the cubic packing. A tessellation was performed on this cubic packing as shown in Figure 2.30. After performing tessellation, 384 tetrahedrons are obtained. For each tetrahedron, the maximum inscribed void was obtained by using modified Nelder-Mead method and the radius the inscribed void was equal to 0.366mm. After checking the interconnectivity between two neighboring voids and merging two voids with interconnectivity of Level 2, 64 pores were obtained with radii of 0.366mm. The pore center distances and throat sizes are constant for all the pores and they are equal to 1mm and 0.207mm, respectively. The coordination number of the pores at the center of the packing was six. These results are consistent with the structural properties of the simple packing as shown in Figure 2.30.
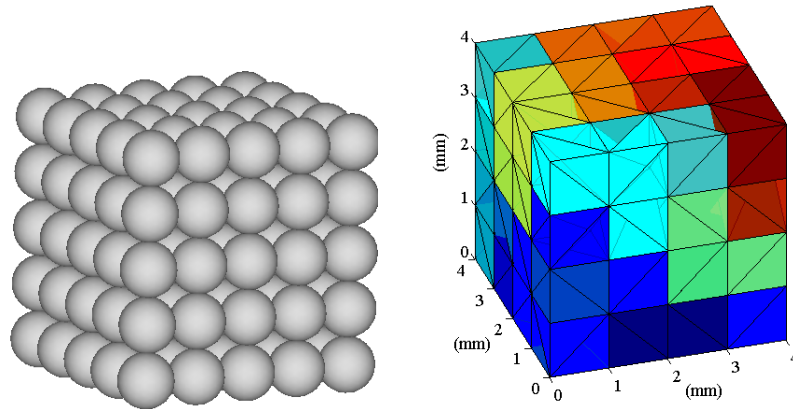
Figure 2.30 An array of cubic packing and schematic of Delaunay Tessellation.

2.5.2 Indirect Validation of the Extracted Pore Network

The proposed algorithm can also be indirectly validated by comparing the predicted permeability of the extracted pore networks with published experimental data.

In order to simulate the single phase flow through the pore network, the flow rate in each bond should be calculated. To simulate the flow through a tube with circular cross section at the pore level, the flow equation of Navier-Stokes equation for saturated steady state Newtonian viscous flow, which is also known as the Hagen-Poiseuille flow equation, can be applied to calculate the flow rate. Assume that the bond connecting pore i with pressure of P_i and pore j with pressure of P_j is in the shape of cylinder with a constant circular cross section, then the discharge through the bond from pore i to pore j can be calculated from Hagen-Poiseuille equation:

$$q_{i,j} = \frac{\pi}{8\mu} \frac{P_i - P_j}{l_b} r^4 \qquad (2.2)$$

where μ is the dynamic viscosity of water; P_i and P_j are the total pressure at the corresponding pores and l_b is the length of the bond connecting pore i and pore j.

However, as to the BACON bond shown in Figure 2.11, the cross sectional dimension of the bond is not constant. Hence Equation 2.2 is modified for the left part of the bond,

$$q_{s,t} = -\frac{\pi}{8\mu}\frac{dP}{dx}y_i^4(1-x/l)^{4n} \text{ for } b_s \le x \le b_t \tag{2.3}$$

where b_s and b_t are the starting position of the bond and position of the throat, respectively, as shown in Figure 2.11.

By integrating the equation from b_s to b_t,

$$\frac{(p_s - p_t)}{q_{s,t}} = \frac{8\mu}{\pi y_i^4 l(1-4n)}\left[\left(1-\frac{b_s}{l}\right)^{1-4n} - \left(1-\frac{b_t}{l}\right)^{1-4n}\right] \tag{2.4}$$

For the right part of the bond,

$$q_{t,e} = -\frac{\pi}{8\mu}\frac{dP}{dx}y_j^4(x/l)^{4n} \text{ for } b_t \le x \le b_e \tag{2.5}$$

where b_t and b_e are the position of the throat and ending position of the bond respectively, as shown in Figure 2.11.

By integrating the equation from b_t to b_e

$$\frac{(p_t - p_e)}{q_{t,e}} = \frac{8\mu}{\pi y_j^4 l(1-4n)}\left[\left(\frac{b_e}{l}\right)^{1-4n} - \left(\frac{b_t}{l}\right)^{1-4n}\right] \tag{2.6}$$

Because of the continuity of flux, $q_{s,t} = q_{t,e} = q_{i,j}$. In addition, as Biconical abscissa Asymmetric CONcentric (BACON) bond is introduced in the network, the cross sectional of bonds is much smaller than that of pores and the length of bond is much larger than its neighboring pores. As a result, it is reasonable to assume that primary head loss occurs in

bonds and there is no pressure drop when water flows through the pore body. Then, $P_s = P_i$ and $P_e = P_j$. By summing up the left side of Equations 2.4 and 2.6, the rate of flow through the bond connecting node i and node j, $q_{i,j}$ is:

$$q_{i,j} = \frac{(P_i - P_j)}{\frac{8\mu}{\pi y_i^4 l(1-4n)}\left[\left(1-\frac{b_s}{l}\right)^{1-4n} - \left(1-\frac{b_t}{l}\right)^{1-4n}\right] + \frac{8\mu}{\pi y_j^4 l(1-4n)}\left[\left(\frac{b_e}{l}\right)^{1-4n} - \left(\frac{b_t}{l}\right)^{1-4n}\right]} \tag{2.7}$$

For each node in the pore network, considering the conservation of mass of water flowing through the network:

$$\sum_{j=1}^{\beta} q_{i,j} = 0 \tag{2.8}$$

where j is the index of the pore bodies that are connected to pore body i.

The resulting Equation 2.8 can be solved by Gauss-Seidel successive over relaxation. Solution of the network equations provides the pressure in each pore of the packed bed, and hence the volumetric flow rate passing through each pore. This information, combined with known dimensional properties of the overall bed is used to calculate averaged macroscopic parameters such as permeability based on Darcy's law.

In this numerical simulation, the equal sized spherical particles were used. Before the simulation, the influence of model size on simulation results was studied and it was found that if the ratio between the model length and particle diameter is greater than 30, the predicted permeability is constant. As a result, in all simulations, the ratio of 35 is used to in all the numerical experiments. During the construction of pore network, after performing tetrahedral tessellation, in order to avoid boundary effects, the tetrahedrons formed by particles within the range of two times of the diameter of the particle in the packing next to the wall were removed. Before the simulation of single phase flow through

the extracted pore network, pressure boundary was applied to the top and bottom planes of the network, respectively, while the four side planes of the network were defined as no flow boundary. During the simulation, the pressure field was solved by Gauss-Seidel iteration method and it was terminated until the iteration error was less than 10^{-5}. To ensure reproducibility, for each particle size, the whole process of simulation including the randomly packing the spheres was repeated three times and the average permeability for each particle size were reported and compared with that of experimental data.

As to the published experiment results on permeability, numerous investigators have measured the permeability of random packing of equal spheres (Wyllie et al., 1955, Chu et al., 1989, Schneider, 1963, Harleman et al., 1963 and Ward, 1964). On average, the bulk properties of random packing should be comparable, though each packing will have a different detailed structure (sphere locations) (Steven et al., 1993). Hence, it is reasonable to compare the permeability of the network model with that of other packing. In these experiments, water or oil was chosen as the fluid for these flow experiments and equal sized glass beads were used in the randomly packed beds. The standard procedures of constant head and falling head permeability tests were followed and laminar flow condition was maintained during the experiment. The permeability values of the randomly packed beds were reported, which was calculated by taking account the viscosity of different fluids.

The comparison between predicted permeability values and those obtained experimentally are shown in Figure 2.31. Figure 2.31 shows a good agreement between the network prediction and the experimental data. The slight scatter may be attributed to the use of non-single size particle in the experiments (it is impossible to have single sized

particles during experiments), or potential difficulty in accurately measuring pressure drop in high-permeability packing. Thus the above validates the proposed network model approach.
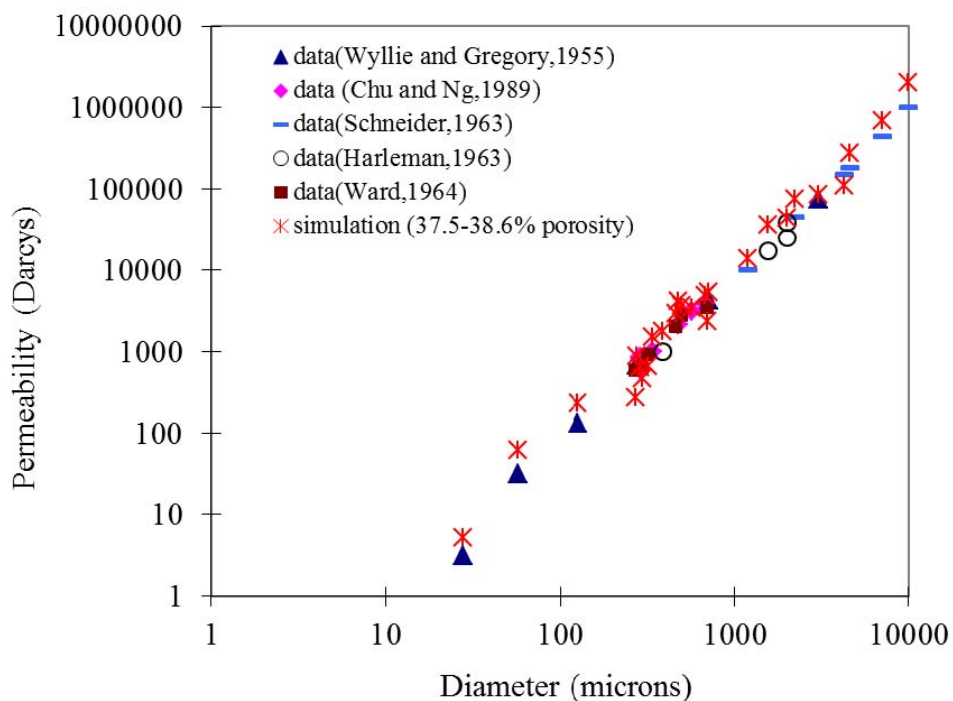
Figure 2.31 Comparison between predicted results by the extracted pore network and experimental results.

2.5.3 Indirect Validation of the Equivalent Network

In order to check the validity of the proposed algorithm of generating equivalent network, the results predicted by the directly extracted network and the equivalent network are compared. The input parameters for the equivalent network are determined as follows: according to the geometrical and topological properties of void space in random packing of spheres discussed in section 2.4, both pore size distribution and coordination number

distribution obey normal distribution. Hence during the construction equivalent pore network, both the pore size distribution and coordination number distribution are generated as normal distribution with the mean value and standard deviation obtained from the corresponding test for construction of extracted pore network model. As to the power exponent distribution of BACON bond, a constant n value is used, which is the average of the power exponent distribution obtained from the extracted pore network. It should be noted here that, as the approach of generating equivalent network is a stochastic approach, which includes assigning the generated pore size distribution and coordination distribution to the voids in the network at random, as a result, for each set of input parameters, the test was repeated five times and the final reported permeability value for a certain set of input is the average of five predicted permeability values. The comparison of the results of two types of network models is presented in Figure 2.32.
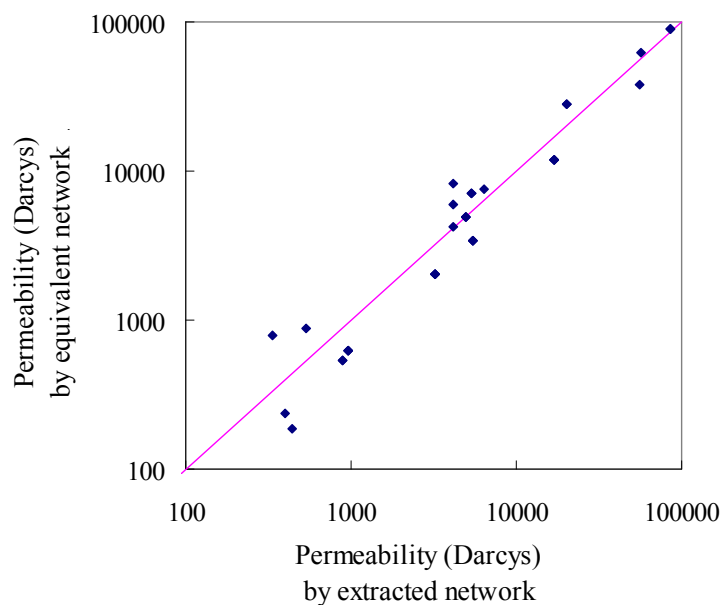
Figure 2.32 Comparison of predicted results by the two types of pore networks.

From Figure 2.32, it can observed that the results obtained by the two types of models matches very well and even for those scatters, the permeability values predicted by the equivalent network are still the same order of magnitude as those obtained by the extracted pore network. The comparison suggests that the equivalent network can also be used as a predictive tool for flow through porous media. Also, results from the above two models compare well with predicted hydraulic conductivity from rigorous micromechanical analysis of Meegoda et al. (1989).

In addition, it is worth mentioning that as the radius of each cross section of bond in the proposed two types of pore networks is the inscribed radius of real pore space, there are great flexibilities of further modification of the shape of the bonds for different accuracies. For example, in order to deal with noncircular cross section of the pore space, the shape factor and hydraulic conductance of noncircular capillaries (Patzek et al., 2001) can be incorporate into the calculation of flow rate in bond in the proposed pore networks to take into account the flow in the corner of the pore space.

2.6   Conclusions

In this chapter, two methodologies of developing pore network model for characterizing the pore space of random packing of spherical particles were proposed. The first approach can generate a statistically equivalent pore network of porous media while the second is about directly extracting the pore network from packing of spheres based on the coordinates and radii of particles in the packing. The second methodology of constructing pore network was directly validated by comparing the extracted geometrical and topological information of void space of a simple packing with the theoretical results and also validated by comparing the simulated permeability of the network with published

experimental data. As to the equivalent network, the predict permeability of packing of spheres were compared with that predicted by the other algorithm. A good agreement between them showed that the equivalent network can also be used as a predictive tool for quantitative study of fluid flow through porous media.

CHAPTER 3

DISCRIPTIONG OF DYNAMIC AIR WATER TWO-PHASE FLOW MODEL

3.1   Introduction

One of the attractive features of pore-scale network models is their ability to simulate actual laboratory experiments. If a three-dimensional network of pore bodies and pore throats is constructed, typically involving tens to hundreds of thousands of pore bodies and throats, then this network may be treated as a "mathematical sample" of porous medium and subjected to "mathematical experiments" that mimic actual laboratory experiments.

In the previous chapter, two methodologies have been proposed to characterize the pore space of porous medium. In this chapter, a rule based on dynamic air water two-phase flow model is developed to simulate the two-phase flow in the pore network during air sparging. The rule based dynamic two-phase flow model allows the wetting and non-wetting fluids flow simultaneously in a cross section of a bond and it can also consider both the viscous and capillary forces during two-phase flow process. The assumptions of the dynamic model, flow mechanisms employed in the dynamic model, fluid configurations, determination of time steps, updating the fluid configurations, computing network saturations and etc. are presented in the following sections.

3.2   Model Assumptions

1. The injected fluid is non-wetting fluid-air while the defending fluid is the wetting fluid-water. The fluids are Newtonian, incompressible and immiscible. The wetting phase is "perfect wettability" with no contact angle hysteresis.

2. The gravity effects of water and air during the flow process are neglected. The capillary pressure difference across an interface between the two fluids in a bond is inversely proportional to the tube radius.

3. Pore-body and throat conductance are computed by assuming Stokes or Creeping flow at the pore level.

4. The two types of fluids can coexist both in bond and nodes. All pressure drops occur in the bonds while the node is so wide than bond that the pressure drop in a node is neglected.

5. The average viscosity of the fluids in a pore throat or pore body is the saturation weighted viscosity of individual phases.

6. It is further assumed that for the isolated fluid in a node, it is kept isolated until the node is full of the isolated fluid. The film flow of water is neglected in this situation.

3.3   Description of Void Space in Porous Medium

The most critical part in constructing a pore-network model for characterizing the pore space in porous is defining its structure and geometry, i.e., the locations of pore bodies, pore-body size distributions, throat-body size distribution, pore connectivity, and the spatial correlation between pore bodies and pore throats (Celia et al. 1995). In this research, the equivalent pore network model which is introduced in Chapter 2 is used to simulate the pore structure of porous medium in the dynamic air water two-phase flow model. Generally, typical parameters required for the creation of an equivalent network include pore body and pore throat size distributions, coordination number distribution, spatial correlation between adjacent pore bodies, and spatial correlation between pore throat size

to pore body size known as aspect ratio. All these parameters can be obtained from the directly extracted pore network model from packing of spheres.

One of main differences between the pore network model employed in this research and that used by other researchers lie in the shape of bond connecting two neighboring pores. In this research, BACON bond is used which is in converging-diverging shape as shown in Figure 3.1:
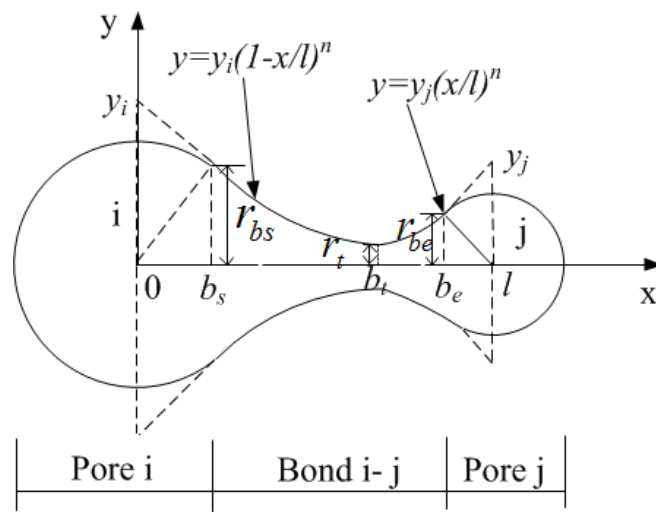
Figure 3.1 Geometrical information of a bond in pore network model

Compared with the bond in cylindrical shape with constant cross-sectional area, one advantage of using this bond is that the air water interface can reside in any position of the bond, which provides great flexibility on determining the time step and updating the position of air water interface. Here, the details of the geometrical information of the bond are determined as follows. Define a bond i-j connecting node i and node j as shown in Figure 3.1, the geometrical information of the bond i-j includes: position of starting point of bond (b_s), position of throat (b_t), position of the ending point of bond (b_e), radius of bond at the starting point (r_{bs}), radius of bond at the ending point (r_{be}), radius of bond at

the throat (r_t), volume of the left part of bond i-j (v_{bl}), volume of the right part of bond i-j (v_{br}), and parameters for charactering the bond i-j: y_i and y_j.

It is assumed that the starting point of the bond is from the position of $r_i/\sqrt{2}$ and the ending point of the bond is at $r_j/\sqrt{2}$. Then, the other parameters can be easily calculated:

$$r_{bs} = r_i/\sqrt{2}, \; r_{bs} = r_j/\sqrt{2}, \; y_i = r_i/\sqrt{2}*(1-r_i/\sqrt{2})^n, \; y_j = r_j/\sqrt{2}*(1-r_j/\sqrt{2})^n,$$

$$b_t = y_i{}^{\wedge}(1/n)*l/(y_i{}^{\wedge}(1/n) + y_j{}^{\wedge}(1/n)), \; r_t = y_i(1-b_t/l)^{\wedge}n,$$

$$v_{bl} = \pi y_i{}^{\wedge}2/(2n+1)*((1-b_s)^{\wedge}(2n+1) - (1-b_t)^{\wedge}(2n+1)),$$

$$v_{br} = \pi y_j{}^{\wedge}2/(2n+1)*(b_e{}^{\wedge}(2n+1) - b_t{}^{\wedge}(2n+1)).$$

3.4   Initial and Boundary Conditions

The medium is initially saturated with the wetting phase and the non-wetting phase is injected at the bottom of the network. At the bottom of the network, a constant air injection pressure is maintained at each pressure step while at the top an exit pressure is maintained. The boundary conditions in the other two directions are no flow boundaries. During the simulation of the air water two-phase flow process, all the bottom nodes are maintained air saturated and the air water interfaces in the bonds connecting to the bottom nodes are introduced at the beginning of the simulation.

3.5   Fluid Flow Description

3.5.1   Fluid Mechanisms

The flow of two or more phases through a porous medium can occur by several mechanisms. Our model incorporates the following three main flow mechanisms:

(a) Bulk Flow---each phase flow in the space occupied by that phase. In this case, single phase Poiseuille Law linearly relates the pressure drop and flow rate in each bond, expressed mathematically in Eq.3.1:

$$q_{ij} = \begin{cases} G_{ij}(P_i^{nw} - P_j^w - P_{cij}), & P_i^{nw} - P_j^w - P_{cij} \geq 0, \\ G_{ij}(P_i^{nw} - P_j^w - P_{cij}), & P_i^{nw} - P_j^w - P_{cij} \leq 0, \\ 0, & Otherwise \end{cases} \tag{3.1}$$

Where the subscritps i and j repsent pore body i and pore body j respectively; q_{ij} is the volumetric flow rate in the bond connecting pore i and pore j; G_{ij} is the conductance of the bond connecting pore i and pore j; P_i^{nw} is non-wetting phase pressure in pore i; P_j^w is wetting phase pressure in pore j; P_{cij} is the capillary force at the interface between wetting phase and non-wetting phase, which depends on the position of meniscus inside a bond.

(b) Meniscus Movement---movement of the interface between wetting phase and non-wetting phase. The moving direction of a meniscus depends on the pressure drop in the bond. The menisci can both invade into or retreat from a bond. The presence of these menisci makes the flow equation non-linear.

(c) Snap Off---depending on the local pressure field, the non-wetting phase can be snapped off, which leads to the formation of isolated non-wetting phase blob. During drainage process, the non-wetting phase moves into a throat, goes past its narrowest point, and snaps off at the throat being invaded if the adjacent body to throat ratio is large enough (i.e., the local capillary pressure is small enough to develop a neck meniscus and snap).

3.5.2 Flow Configurations

As the pore network consists of bonds and pore bodies, the fluid configurations for both of them will be discussed separately.

As to a bond, it can be occupied by either water or air, or occupied by the both fluids. Based on the types of fluids in a bond and also the types of fluids in the nodes on the both sides of the bond, there can be three configurations in a bond: a bond with one air-water interface, a bond with two air-water interfaces and a bond with no interface. Take bond ij for example, here the bond ij is the bond connecting two neighboring nodes- node i and node j.

One-interface configuration: it is the case that node i is occupied by one type of fluid while the node j is occupied by the other type of fluid. As to the bond, it can be divided into two parts: the left part is connected to node i and it is filled with the fluid same as that in pore body i while the right part is connected to node j and it is filled with the fluid same as that in pore body j. In this case, there is only one air-water interface. The interface can either move in the direction towards node i or move in the direction towards node j, which are corresponding to drainage or imbibition process respectively.

Two- interface configuration: there are two special cases for this type of configuration. Case I: both node i and node j are filled by the same type of fluid (air or water) while the part of bond ij is filled with the other type of fluid. In this case, one type of fluid is isolated in the bond by the other type of fluid. The isolated fluid can either move towards node i or move towards node j depending on the pressure drop from node i to node j. Case II: this case is similar to the case for one interface configuration that node i and node j are filled with different types of fluids and the bond is occupied by the both types of fluids.

The bond can be divided into two parts: the left part is connected to node i but it is filled with the fluid different from that in pore body i while the right part is connected to node j but is filled with the fluid different from that in pore body j.

No interface configuration: this is the case that the two neighboring pore bodies node i and node j and the bond ij between them are filled with single type of fluid, either water or air.

It should be noted here that, the configuration with more than two air-water interfaces in a bond is neglected in this research.

As to a pore body, two main types of configurations of nodes are defined here: the first one is called two-phase node while the second one is called one phase node.

Two-phase node: For this type of nodes, both air and water phase can coexist in the node and can flow in/out of the node simultaneously. When there are two types of fluids present in the node, each type of fluid should have at least one bond connecting to it filled with the same type of fluid. The typical configurations of two-phase node are shown in figure 3.2.
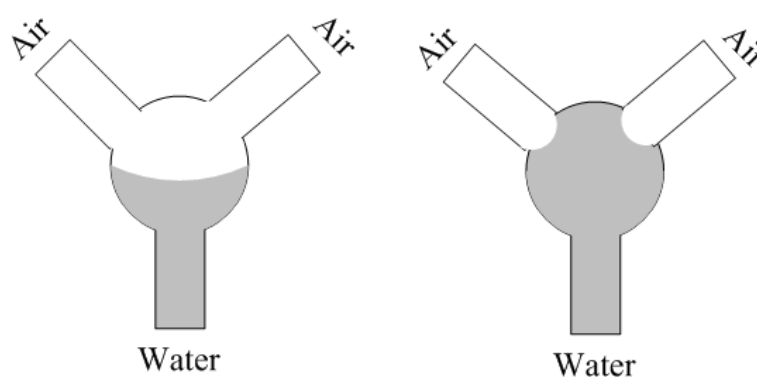
Figure 3.2 Schematic of two-phase nodes.

One-phase node: For this type of nodes, there can be two types of fluids or single type of fluid in the node. When there are two types fluids present in a node, only one type

of fluid is continuous in the pore network while the other one is isolated in the pore network without any bond connecting to it filled with the same type of fluid. In this case, the saturation of the isolated phase in the node is called residual saturation of the node. During the simulation, it is assumed that the isolated phase in the node does not move until the node is full of the isolated phase, and then there is only one type of fluid isolated in the node. The typical configurations of one-phase nodes are shown Figure 3.3.
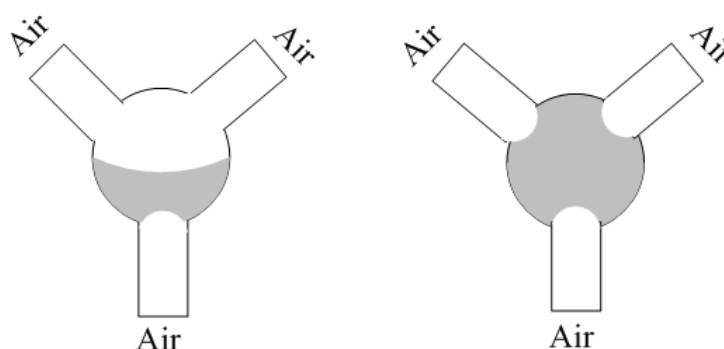
Figure 3.3 Schematic of one-phase nodes.

3.6   Solving for Pressure Field

3.6.1   Flow through a Bond

During two-phase flow during air sparging, the conservation of flow quantities at each node is maintained. The pressure field in pore network during two-phase flow simulation can be obtained by solving the equations of conservation of flow quantities at each node. In this section, flow in a bond is introduced first.

When considering two-phase flow in a bond, the capillary force at the air-water interface is an important force which should be considered carefully. With respect to the capillary pressure, as the Biconical abscissa Asymmetric CONcentric (BACON) bond is

used in the pore network as shown in Figure 3.4, the capillary pressure becomes a function

of the position of the meniscus in the bond.
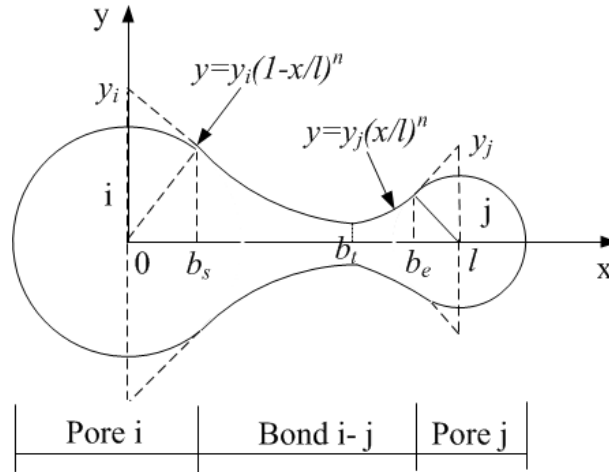
Figure 3.4 Configuration of a BACON bond.

The capillary force in a BACON bond can be expressed as follows:

For the air-water interface on the left side of the throat:

$$P_c = \frac{2\sigma}{y_i * (1 - x/l)^n} \tag{3.2}$$

For the air-water interface on the right side of the throat:

$$P_c = \frac{2\sigma}{y_j * (1 - x/l)^n} \tag{3.3}$$

As mentioned in Chapter 2, the volume flux q_{ij} through a bond connecting nodes i and j

with no fluid interface in the tube can be expressed as:

$$q_{i,j} = \frac{(P_i - P_j)}{\frac{8\mu}{\pi y_i^4 l(1 - 4n)}\left[\left(1 - \frac{b_s}{l}\right)^{1-4n} - \left(1 - \frac{b_t}{l}\right)^{1-4n}\right] + \frac{8\mu}{\pi y_j^4 l(1 - 4n)}\left[\left(\frac{b_e}{l}\right)^{1-4n} - \left(\frac{b_t}{l}\right)^{1-4n}\right]} \tag{3.4}$$

By considering two-phase flow through a bond, the bond may be filled with wetting

and nonwetting phases, which introduces either one or two menisci. Duo to the existence of

menisci in the bond, the movement of nonwetting is impeded while the movement of wetting phase is promoted. In order to consider the effects of the interfaces on the two-phase flow, the parameters of capillary forces should be introduced into the above formula.

In addition, for two types of fluids present in a bond, the viscosity is not a constant as that during single phase flow. It depends on the volumetric percentage of each phase in the bond. In order to consider the viscosity of fluids in a bond during two-phase flow, an effective viscosity is introduced, where μ_{eff} can be calculated as:

$$\mu_{eff} = (1 - S_w) * \mu_{air} + S_w * \mu_w \tag{3.5}$$

Using the weighted viscosity is motivated by the fact that when both phases are presented in a bond, both viscosities play a role in determining the relative strength of viscous and capillary forces.

Finally, the flow quantities in the bond connecting pore i and pore j for air water two-phase flow can be expressed as:

$$q_{i,j} = \frac{(P_i - P_j - P_c)}{\frac{8\mu_{eff}}{\pi y_i^4 l(1-4n)}\left[\left(1-\frac{b_s}{l}\right)^{1-4n} - \left(1-\frac{b_t}{l}\right)^{1-4n}\right] + \frac{8\mu_{eff}}{\pi y_j^4 l(1-4n)}\left[\left(\frac{b_e}{l}\right)^{1-4n} - \left(\frac{b_t}{l}\right)^{1-4n}\right]} \tag{3.6}$$

3.6.2 Determining the Flow Field

As the fluids are assumed as incompressible and immiscible, consequently, the volume flux is conserved everywhere in the network. At each node, the following equation can be maintained:

$$\sum_j q_{ij} = 0 \tag{3.7}$$

In the Equation 3.7, q_{ij} is the volumetric flow rate of flow from pore j to pore i. The summation of j runs over the nearest neighbor nodes to the ith pore where i runs over all nodes that do not belong to the top or bottom planes. Equation 3.6 and 3.7 constitute a set of linear equations which are to be solved for the nodal pressure with the constraints that the pressures at the nodes belonging to the upper and lower rows are kept fixed. The equation 3.7 can be solved by using Gauss-Seidel iterative method or conjugate gradient method.

It should be noted here that while calculating the flow quantity in a bond, both drainage and imbibition are allowed to occur in this model. For example, in the following Figure 3.5, node i is filled with air while the node j is filled with water. If $P_i - P_c \geq P_j$, then the air water interface will move to the right side, called drainage, however, if $P_i - P_c \prec P_j$, then the air water interface will move to the left side, called imbibition. This way of dealing with the movement of interface is different from that of static multiphase flow models (Martin et al, 1990) in which the air-water interface is frozen by capillary force if $P_i - P_c \prec P_j$, as result, the no flow occurs cross it until P_i increases.
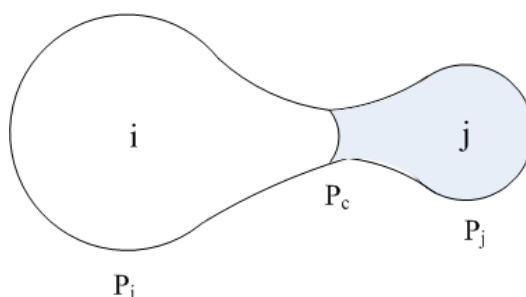
Figure 3.5 Schematic of drainage and imbibition situations.

3.7   Selection of Time Step

For the bond i-j which connects node i and node j, a time step Δt_{ij} is chosen such that every

meniscus is allowed to travel at most a maximum step length $\Delta x_{\max}$ during that time step.

Then, the minimum time step of all the bonds $\min(\Delta t_{ij})$ in the network can be determined,

which is the time step $\Delta t_{\min}$ for the whole network with the current configurations. The

calculation of time step depends on the positions of interfaces and different fluid

configurations in bonds which are mentioned in chapter 3.5. The calculations of time steps

for each configuration are as follows:

3.7.1   Time Step for the Configuration of No Interface

For the configuration of no interfaces, it is the case that both nodes i, j and the bond i-j

connecting the two nodes are filled up with one type of fluid (air or water). The time step

for this type of configurations is set as a very larger number (e.g., 1), which is not to be

considered for updating configurations.

3.7.2   Time Step for the Configuration with One Interface

For the configuration of one interface, it is the case that node i is filled up with air while the

node j is filled up with water. There are three situations for calculating time step in the bond

i-j. Here, only the determination of time steps of the drainage flow is presented. As the

determination of time steps of imbibition flow is quite similar to that of the drainage flow,

it won't be repeated here. Define node i is an air saturated node and node j is a water

saturated node. Air saturation of the bond i-j is S_{nw} and the flow rate in the bond is q_{ij} with

direction from node i to node j (drainage). The configuration of the bond is same as that

shown in Figure 3.4: the starting position of the bond is b_s, the ending position of the bond

is b_e, the position of the throat is b_t and the position of air-water interface in a bond is

$P_{\text{int } erface}$. In the following parts, the determination of time steps under different situations

will be discussed for the drainage flow.

Situation 1: $b_s \leq P_{\text{int } erface} \leq b_t$

In this situation, the air-water interface is in the left part of the bond (between the

node i and the throat), then a time step is chosen such that the meniscus is allowed to travel

to the throat during the time step. Then the time step of the bond i-j can be calculated based

on the saturation of the bond and the volumetric flow rate through the bond, which is

expressed as:

$$t_{ij} = \frac{v_{bl} - (v_{bl} + v_{br}) * S_{nw}}{q_{ij}} \tag{3.8}$$

Situation 2: $b_t \prec P_{\text{int } erface} \prec b_e$

In this situation, the air-water interface is in the right part of the bond (between the

throat and the node j), and then a time step is chosen such that the meniscus is allowed to

travel to the right end of the bond (fill up the bond with air). The time step of the bond i-j

can be calculated based on the saturation of the bond and the volumetric flow rate through

the bond, which is expressed as:

$$t_{ij} = \frac{(v_{bl} + v_{br}) * (1 - S_{nw})}{q_{ij}} \tag{3.9}$$

Situation 3: $P_{\text{int } erface} = b_e$

In this situation, the air-water interface is at the right part of the bond. It should be

noted here that although the air saturation of the bond is 1 in this situation, there is still one

air-water interface in the bond i-j unless the node j is also full of air. The time step is

chosen to fill up the node j by air. When calculating the time step in this situation, special

attentions should be paid to the situation that more than one bonds may inject air into the

node, which is different from that in static models (Martin et al, 1990). In static model,

during each time step, only one node can be filled. However, in the dynamic model

developed here, during each time step, multiple nodes can be filled simultaneously. So, all

the bonds connected to the node j will be scanned to check the number of bonds filling up

the node j simultaneously. So, the time step can be expressed as:

$$t_{ij} = \frac{v_j * S_{wj}}{\sum q_{kj}} \tag{3.10}$$

Where v_j is the volume of node j, s_{wj} is the water saturation of node j and k is the index of

the nodes that connected to node j with bond k-j injecting air to the node j.

3.7.3   Time Step for the Configuration with Two Interfaces

For the configuration of two interface, it is the case that both node i and node j are filled up

with single type of fluid, water or air while the bond is filled up with or partially filled by

the other type of fluid. Same as that in Section 3.7.2, determination of time step with flow

direction from node i to node j (drainage) is considered while the flow in the other direction

(imbibition) is not repeated here. Here, the position of right air-water interface is defined as

$P_{iterface-r}$ and the definitions of other parameters including the starting point, ending point

and position of throat are same as those defined above. There are three situations for

calculating time step of the bond i-j:

Situation 1: $b_s \leq P_{interface-r} \leq b_t$

In this situation, the left part of bond is filled with water and the right air-water interface is in the left part of the bond (between the node i and the throat) as shown in the following figure:
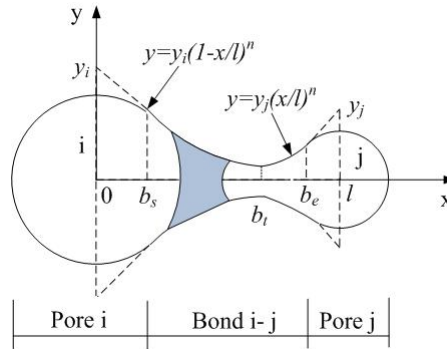
Figure 3.6 Situation 1 for time step calculation for two-interface configuration.

Then a time step is chosen such that the meniscus is allowed to travel to the throat during the time step. The time step of the bond i-j can be calculated based on the volume between the right air-water interface and the throat and the volumetric flow rate through the bond. For simplicity, the space between the right air-water interface and the throat is assumed in the shape of circular truncated cone. The radius of the right air-water interface is: $r_{interface-r} = y_i(1 - p_{interface-r}/l)^n$. The time step can be estimated as:

$$t_{ij} = \frac{\pi(b_t - p_{interface-r}) * (r^2_{interface-r} + r_{interface-r} * r_t + r_t^2)}{3q_{ij}}$$

(3.11)

Situation 2: $b_t \prec P_{interface-r} \prec b_e$ & $P_{interface-r} \leq b_t$

In this situation, the water phase in the bond is across the throat as shown in the following figure:

Figure 3.7 Situation 2 for time step calculation for two-interface configuration.

In order to determine the time step of this bond, the volume of the water phase between the left air-water interface and the throat and the volume of the water phase between the right air-water interface and the right end of the bond should be compared and the smaller volume is used for determining the time step. Then a time step is chosen such that the left meniscus is allowed to travel to the throat or the right air-water interface is allowed to travel to the right end of the bond. The time step of the bond i-j can be estimated by the using the following equation:

$$t_{ij} = \frac{\min(v_l, v_r)}{q_{ij}} \tag{3.12}$$

Where the v_l and v_r are the volumes of the left space and the right space mentioned above respectively. The volumes v_l and v_r can be estimated by the following two Equations:

$$v_l = \frac{\pi(b_t - p_{interface-l}) * (r_{interface-l}^2 + r_{interface-l} * r_t + r_t^2)}{3} \tag{3.13}$$

$$v_r = \frac{\pi(b_e - p_{interface-r}) * (r_{interface-r}^2 + r_{interface-r} * y_j * (b_e / l)^n + (y_j * (b_e / l)^n)^2)}{3} \tag{3.14}$$

Situation 3: $b_t \prec P_{interface-r} \prec b_e \, \& \, P_{interface-r} \geq b_t$

In this situation, the water phase is in the right part of the bond as shown in Figure 3.8.
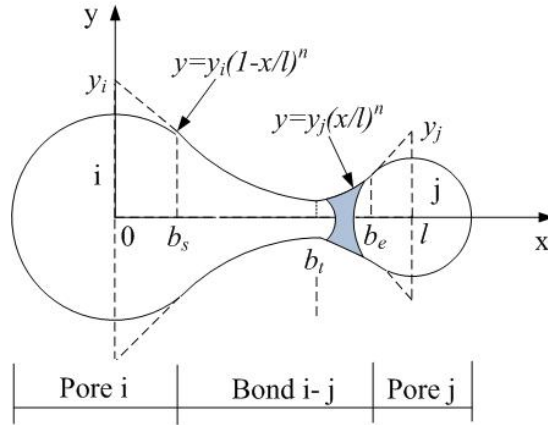
Figure 3.8 Situation 3 for time step calculation for two-interface configuration.

The time step is chosen that the right air-water interface can travel to the right end of the bond, which can be expressed as:

$$t_{ij} = \frac{\pi(b_e - P_{interface-r}) * (r_{interface-r}^2 + r_{interface-r} * y_j * (b_e / l)^n + (y_j * (b_e / l)^n)^2)}{3q_{ij}}$$

(3.15)

Situation 4: $P_{interface-r} = b_e$

In this situation, the right air-water interface is at end the bond as shown in the following figure:
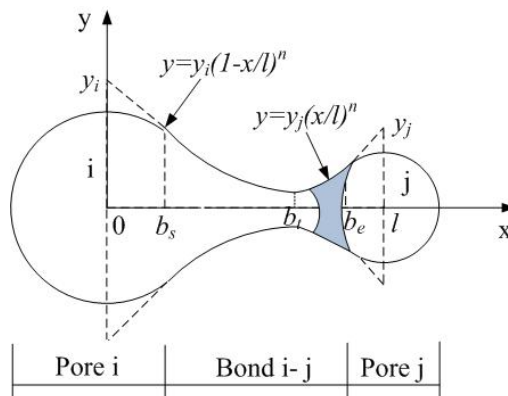
Figure 3.9 Situation 4 for time step calculation for two-interface configuration.

Then, the time step is chosen to filling up the node j by the air. When calculating the time step in this situation, the situation that more than one bond fills up the bond simultaneously still need to be carefully treated. So, all the bonds connected to the node j should be scanned to check the number of bonds filling up the node j simultaneously. The time step can be estimated as:

$$t_{ij} = \frac{v_j * S_{wj}}{\sum q_{kj}}$$

(3.16)

Where v_j is the volume of pore j, s_{wj} is the water saturation of pore j and k is the index of the pores that are connected to node j with bond k-j and inject water into the node j thorough bond k-j with the current fluid configurations.

3.8   Updating Fluid Configurations and Parameters

As mentioned in Section 3.7, once the time step for each bond in the pore network is determined, the minimum time step of all the calculated time steps in each bond Δt_{min} can be chosen as the time step for the whole network with the existing fluid configurations. Then, the fluid configurations including number of interfaces in the bond, the positions of interfaces, saturation of each bond and nodes should be updated. Finally, the parameters for simulation of two-phase flow through the pore network including the capillary force, effective viscosity of fluids in each bond can be updated.

3.8.1   Update Fluid Configurations

As the pore network contains two parts: pore bodies and bonds, both of them are need to be updated during the air-water two phase flow. Generally, updating fluid configurations contain two main parts; one is for updating saturation, number of interfaces, positions of

interfaces and radii of interfaces in bonds while the other one is for updating saturation, number of interfaces and radii of interfaces in pore bodies.

When updating the fluid configurations in bonds, the time step of the bond i-j Δt_{ij} should be always compared with the time step of the whole network $\Delta t_{\min}$. In order to improve the efficiency of the simulation, an allowable error Δe_{allow} is set up to account for the time steps that are close to the time step of the whole network. It is determined here that if $\dfrac{\Delta t_{ij} - \Delta t_{\min}}{\Delta t_{\min}} \leq \Delta e_{allow}$, then assume the time step of bond ij is equal to the time step of the network ($\Delta t_{ij} = \Delta t_{\min}$) and update the fluid configuration in bond i-j based on the time step Δt_{ij}, otherwise, update the fluid configuration in bond i-j based on the time step of the whole network ($\Delta t_{\min}$).

(1) For bonds with one air-water interface

For the bonds with one air-water interface, if the difference between the time step of the bond i-j and the time step of the network is less than the allowed error ($\dfrac{\Delta t_{ij} - \Delta t_{\min}}{\Delta t_{\min}} \leq \Delta e_{allow}$), then the new position of the air-water interfaces can be easily determined based on the positions of the air water interface used for determining the time step of the bond i-j. For example, for the drainage from node i to node j, if the air-water interface is behind the throat, then the updated position of the interface should be at the throat; if the air-water interface is beyond the throat, then the updated position of the interface should be at the right end of the bond i-j; if the air water interface is at the end of the bond, then both the bond and node connected to the right end of the bond become full of

air and there is no interface in the bond any more. Once the new position of the interface is determined, the saturation of the bond and radius of the interface can be easily updated as well.

If $\dfrac{\Delta t_{ij} - \Delta t_{min}}{\Delta t_{min}} \succ \Delta e_{allow}$, then the fluid configuration of bond i-j should be

updated based on Δt_{min} . As the shape of the bond is not cylindrical and its cross section area varied at different location of the bond, try and error approach is used to update the position of the interface. An example of determining the time step under this situation is shown in the following Figure 3.10:
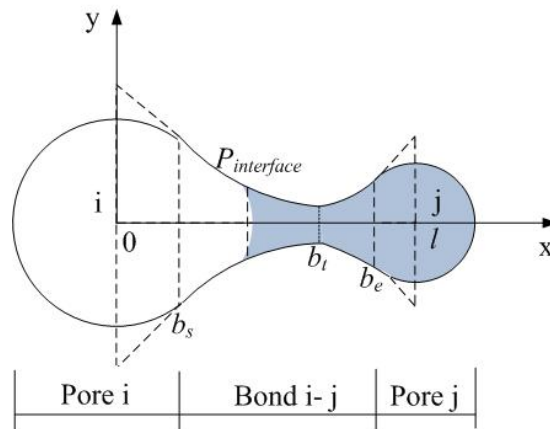
Figure 3.10 Configuration of one-interface bond for updating fluid configuration.

In this example, flow rate in the bond i-j is q_{ij} , and the difference between time step of bond

and time step of the whole network meet the requirement that: $\dfrac{\Delta t_{ij} - \Delta t_{min}}{\Delta t_{min}} \succ \Delta e_{allow}$. To

update the fluid configuration in the bond i-j, the following iteration procedure is applied:

Initially, the new position of the air water interface can be assumed based on the ratio between the time step in the bond i-j and the time step of the whole network:

$(p_{\text{int}erface})_{new} = p_{\text{int}erface} + \dfrac{\Delta t_{\min}}{\Delta t_{ij}} * (b_t - p_{\text{int}erface})$. Based on this new position of the air water

interface, the radius of the new interface can be also be determined based on the

configuration of the bond as shown in Figure 3.4. Then the volume of the bond between the

current air-water interface and the assumed new air water interface can be calculated as

well. Finally, the time required for filling up the new volume $\Delta t'$ can be determined by

considering the volumetric flow rate in the bond. Now the new position of the interface

should be checked whether it is reasonable or not by comparing the calculated time step

with the time step of the network. If $\dfrac{\Delta t' - \Delta t_{\min}}{\Delta t_{\min}} \leq \Delta e_{allow}$ then, the assumed the new position

will be the updated position of the air water interface, otherwise, the whole process will be

repeated until it meet the requirement of allowed time error.

(2)   For bonds with two air-water interfaces

As defined in the Section 3.4.2, there are two cases for the configuration with two air-water

interfaces. However, as the updating processes for the both cases are same, the updating

process for only one case of them is presented here.

Similar to the procedure for updating the air-water interface in the bonds with one

interface, if the difference between the time step of the bond i-j and the time step of the

network is less than the allowed error ($\dfrac{\Delta t_{ij} - \Delta t_{\min}}{\Delta t_{\min}} \leq \Delta e_{allow}$), then the new position of the

air water interfaces can be easily determined according to the positions used for

determining the time step of the bond i-j.   If $\dfrac{\Delta t_{ij} - \Delta t_{\min}}{\Delta t_{\min}} \succ \Delta e_{allow}$, then the fluid

configuration of bond i-j should be updated based on the ratio between $\Delta t_{\min}$ and try and

error approach will be used to update the position of the interface, which is similar to the updating process for one-interface bond mentioned above. However, the main differences between the calculation for bonds with one interface and the bonds with two interfaces lie in the calculation of the new volume of bond between old interface and newly assumed interfaces. For the situation of two interfaces, with a certain movement of air water interface, special effort should be taken to calculate the corresponding change of volume for both the left air-water interface and the right air-water interface.

When updating configurations in pore bodies, there are two special situations: one is that a pore body is initially fully saturated with water but gets completely air saturated at the end of the time step (called drained nodes) while the second situation is that a pore body is initially full of air but imbibed by water and becomes water saturated at the end of the time step (called imbibed nodes). The two different situations discussed separately as follows:

(1) For drained nodes

For drained nodes, once it changes from a water saturated node to an air saturated node, it leads to an increase/decrease of number interfaces in the bonds connected to it. The following figure shows different situations of changing of air-water interfaces in the bonds connected to the drained node.
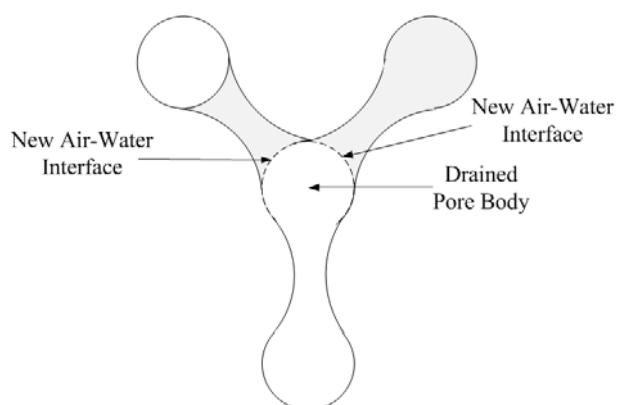
Figure 3.11 Updating the fluid configuration of a drained node.

As shown in Figure 3.11, once a node becomes air saturated at the end of a time step, one air-water interface is created in the bond connected to it if the bond is filled up with water or partially filled with water. As a result, for the bond full of water before this time step, the number of air water interface is changed from 0 to 1 while for the bond partially filled with water, the number of air water interface is changed from 1 to 2.

Similarly, for the imbibed node, once it changes from an air saturated node to a water saturated node, it also leads to an increase/decrease of number of interfaces in the bonds connected to it. Different situations of changing of air-water interfaces are shown in the following figure.
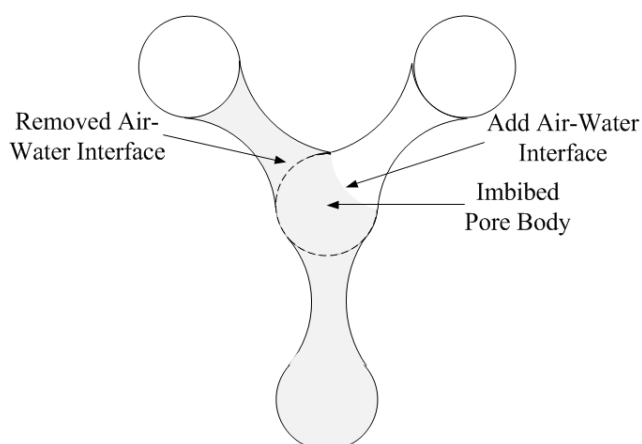
Figure 3.12 Updating the fluid configuration of an imbibed node.

As shown in Figure 3.12, once a pore is filled up by water during a time step, the air water interface is removed in the connected bond which is filled with water and the air water interface is created in the connected bond which is filled with air. For a bond full of water before the time step, the number of air-water interface is changed from 1 to 0 and for the bond partially or fully filled with air, the number of air-water interface is changed from 2 to 1. For the bond full of air, the number of air-water interface is changed from 0 to 1.

3.8.2   Update Pore Network Parameters

As shown in Equation 3.6 which is for calculating the volumetric flow rate in each bond, there are two parameters: capillary force and effective viscosity that vary along with the fluid configuration. Once the fluid configurations are updated as mentioned in the last section, the positions and radii of interfaces can be easily be determined.   Then the capillary force can be calculated as $2\sigma / r_{\mathrm{int}erface}$ while the effective viscosity can be calculated as weighted viscosity $\mu_{eff} = (1 - S_w) * \mu_{air} + S_w * \mu_w$.

3.9   Computing Saturation

During the simulation of air-water two-phase flow, temporal variation of the saturation of the network is recorded for the purpose of developing the correlation between the relative permeability and saturation or for the purpose of developing the correlation between capillary force and saturation. In addition, in order the check the front dynamics of air water two-phase flow during air sparging, both the saturation of each layer and the saturation of the whole network should be calculated. When calculating the saturation for each layer or for the whole network, both the saturation of the bonds and the saturation of the nodes should be considered. As the pore bodies at the bottom are always full of air, the

nodes in this layer are not considered in the calculation of saturation. The calculation of saturation of each layer is defined in the following equation:

$$
\begin{cases}
S_i^{nw} = \dfrac{\displaystyle\sum_{j=1}^{n_b} S_j^{nw} V_{bj} + \sum_{k=1}^{n_p} S_k^{nw} V_{pk}}{\displaystyle\sum_{j=1}^{n_b} V_{bj} + \sum_{k=1}^{n_p} V_{pk}}, i = 2,...,n_z \\[6pt]
S_i^{w} = 1 - S_i^{nw}
\end{cases}
\tag{3.17}
$$

Where n_z is the total number of layers in the pore network; n_p, n_b are the total number of pore bodies and bonds in each layer respectively; V_p, V_b are the volume of pore bodies and bonds respectively.

In addition, it is time consuming and also not necessary to calculate the saturation after each time step, as only small change of saturation occurs during each small time step. In this research, the saturation of every 50 time steps was calculated and recorded.

3.10 Stopping Criteria

For each air injection pressure, the drainage simulation is terminated once the steady state has reached. There are lot of criteria can be used as stopping criteria during air water two-phase flow, such as using variation of air injection rate (for constant air injection pressure), changing rate of air saturation or nonwetting fractional flow. In this research, the changing rate of air saturation is employed as the stopping criterion in this research. During the simulation of air-water two-phase flow, the pressure at the bottom boundary was increased by a specified pressure drop each time until fluid distribution reached an equilibrium configuration during this pressure step. The saturation of the whole network and the moving average of the saturation change per time $\left| \Delta \overline{s}_w / \Delta t \right|$ was successively

calculated for a window of 50 time steps. The equilibrium condition is set to be $\left|\Delta \overline{s}_w / \Delta t\right| \prec 10^{-3}$.

3.11 Summary

In this chapter, the dynamic air water two phase flow model was described. The details on model assumptions, boundary conditions, types of fluid configurations, determination of the time step, updating of fluid configurations, capillary force, and effective viscosity of fluids in the networks, compute of saturation of each layer of the network, stopping criteria and etc. were presented. The flow chart of simulating the air water two-phase flow process by the dynamic model is shown in the following figure.
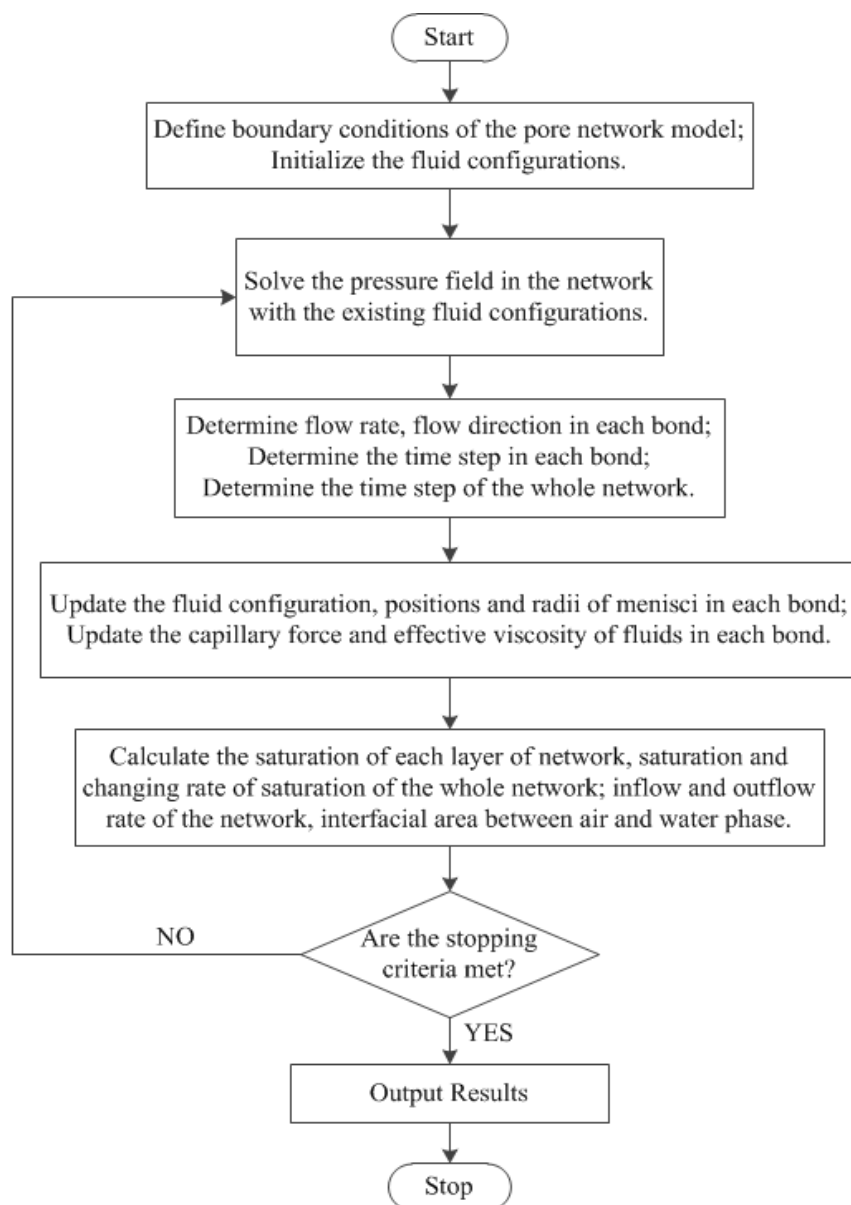
Figure 3.13 Flow chart of simulating two-phase flow process by the developed dynamic model.

This model can capture the temporal variation of saturation of the each layer of the network, air-water interfacial areas in each layer of the network, the outflow rate of each phase and etc. Both the dynamic relative air/water permeability and the dynamic capillary pressure curve can be calculated by this model, as a result, it can be employed to study the dynamic air water two-phase flow properties during air sparging.

CHAPTER 4

TWO-PHASE FLOW DURING AIR SPARGING

4.1 Introduction

In order to bridge the gap between the pore scale and the porous-medium-continuum scale, the air-water two phase flow process simulated at pore scale can be translated into functional relationships between continuum-scale variables.

One important functional relationship for macroscopic research is relative permeability-saturation. As suggested by Reddy (2008), when considering the factors of air flow dynamics within the zone of influence, one recommendations can be made for modeling purposes is that flow of multiple fluids within a porous media may be modeled using Darcy's Law. Flow of each fluid will depend on its own relative permeability. As we know relative permeability depends primarily upon the microscopic distribution of the fluids within the pore space, relative air permeability within the zone of influence will increase with increased air injection. Under different air injection conditions with different capillary numbers, the distribution of fluids at the pore scale and flow patterns show quite different behaviors depending on the level of saturation, the saturation history and direction of saturation change. However, currently the correlation between the rate of air injection and the degree of relative permeability is still unknown. In this section, the dynamic properties of air relative permeability during air sparging will be studied by using the developed pore network models described in Chapter 3.

Another important functional relationship for macroscopic model is the correlation between capillary force and saturation. There is an empirical relationship between

capillary pressure and saturation in the form that $P^n - P^w = P^c = f(S)$ where P^n and

P^w are the average pressures of nonwetting and wetting phases respectively. P^c is capillary

pressure, and S is the wetting phase saturation. Usually this relationship is obtained

experimentally under equilibrium conditions. Thus, to obtain a drainage (or imbibition)

curve, one starts with a wet (or dry) soil sample, then the capillary pressure is increased (or

decreased) incrementally. At each step the water content is measured after equilibrium is

reached. The typical time needed to construct a complete capillary pressure-saturation

curve is in order of weeks or longer. Now, the question arises whether such curves

adequately describe the relationship between capillary force and saturation in the order of

hours. In fact, there is ample theoretical and experimental evidence that this simple

relationship is not unique but it depends on the flow dynamics; it depends on both the

history and the rate of change of saturation. The dependence of capillary curves on the rate

of change of saturation is due to dynamic effects, and this is one of the subjects of this

study.

In addition, the effects of capillary number and pore size distribution on residual

saturation, temporal evolution of air/water saturation, dynamic phase transition and

nonwetting phase fractional flow are also studied in this research.

4.2   Determination of Pore Network Model Parameters

4.2.1   Two Definitions of Capillary Number

Before presenting any results, the definition of capillary number is defined here. Usually,

the capillary number is defined as $C_a = \dfrac{\mu V}{\sigma}$, which represents the relative effect of viscous

forces versus surface tension acting across an interface between two different liquids. Here, μ is the viscosity of the liquid; V is displacement velocity and σ is the surface or interfacial tension between the two fluid phases. This definition is called microscopic Capillary Number here. During air water two-phase flow, the microscopic Capillary Number can be defined as $C_a = \dfrac{\mu Q_{inj}}{\sigma \sum}$, where Q_{inj} is the total air injection rate at the bottom of the network and $\sum$ is the cross-section area of the network. Singh et al. (2003) argued that the above definition of capilalry number from steady-state flow field is not consistent and they suggested another consistent definition of capillary number which is employed in this research. According to Singh et al (2003), the capillary number is defined as $N_{ca} = \dfrac{\mu K \Delta P}{\sigma L}$.

Here, K is the single-phase permeability, ΔP is the pressure drop across the network for single-phase flow, σ is the interfacial tension, and L is the axial length of the porous medium. This definition of capillary number is called as macroscopic capillary number. In this research, the second definition of capillary number is employed. One main advantage of using definition of macroscopic capillary number instead of the microscopic capillary number is that the second definition of capillary number can be predetermined before the numerical experiments with constant air injection pressure; as a result, it is very helpful in designing scheme of experiments. As to the first definition of the capillary number, it is very helpful if the air sparging simulation is performed with constant air injection rate.

In this section, the two definitions of capillary number are compared and discussed. The process for calculating the two defined capillary numbers is beriefly summarized as follows. At a certain air injection presure, the macroscopic capillary number can be calculated by knowing the permeability coefficient of the pore network and also the

dimension of the network. As to the microsocpi capillary number, it can be calculated at the end each simulation with a certain air inejction pressure. For a certain air injection pressure, once the air flow reaches the steady state, the outflow rate can be collected. Then, based on the air injection rate at the steady state and the cross section area of the network, the microscopic capillary number can be calculated. The comparisons of the two definitions of capillary number are shown as follows:
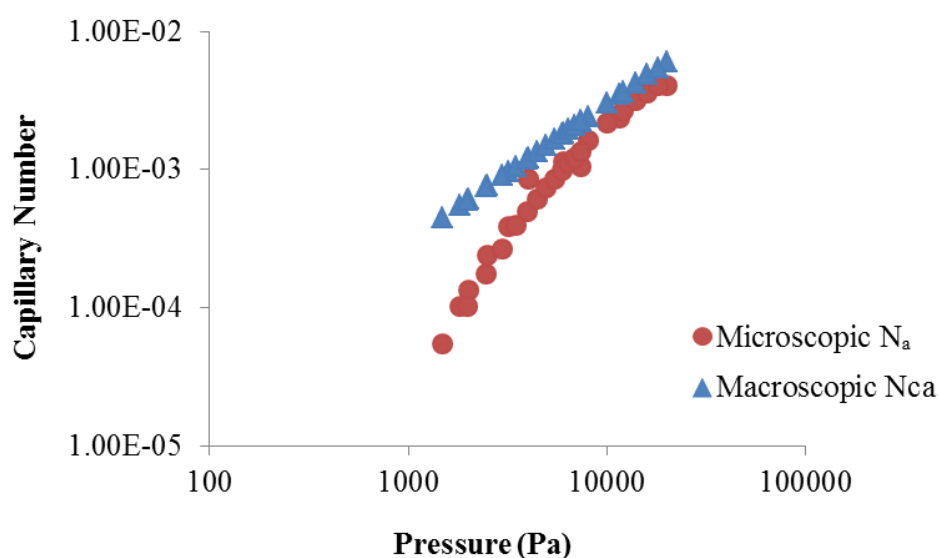
Figure 4.1 Comparison between the two definitions of capillary number.

From the above figure, it can be observed that for air-water two-phase flow at high capillary number, the two definitions of capillary number are almost identical with each other. However, for the flow at low capillary number, the macroscopic capillary number is higher than microscopic capillary number. These results are consistent with our knowledge on the two-phase flow process during air sparging. As we know, at low air injection pressure, the capillary force is much larger than that of viscous force. Under this condition, the flow regime is always the capillary finger and there are only a few continuous air channels formed in the network while most of nonweting phase may be isolated air clusters.

So, the microscopic capillary number which is calculated based on the outlfow of air come out very small numbers. On the other side, the macroscopic capillary number is calculated based on the air permeability of the pore network, as a result, it is not affected by the flow regime. At high air injection pressure, the air flow rate is increased greatly and the flow regime is transferred from capillary finger to viscous finger. Under this condition, more and more continuous flow channels can be developed during the two-phase flow process. Once the air flow reaches the steady state, the two-phase flow under traisnent flow condition may even transfer to single phase flow at steady state, as a result, the bases of calculating the two capillary numbers are same as each other. So the two definitions of capillary number are close to each other under high air injection conditions as shown in Figure 4.1.

4.2.2 Network Dimensions

Another important parameter need to be defined before the simulation of air-water two-phase flow is the network size. The air water two phase flow simulation is time consuming for large size of pore network model; however, if the size the pore network model is too small, it cannot produce reproducible results. In order to obtain the appropriate size of networks employed in this research, air water two phase flow in three different sizes of networks are studied and compared in this section. The appropriate size of pore network used in this research is suggested.

In this section, three sizes of network are employed in simulation of air-water two-phase flow: the first network has 12 nodes in each directions with total 1728 nodes, the second network has 15 nodes in each direction with total 3375 nodes and the third one has 17 nodes in each direction with total 4913 nodes. The three networks have same pore size

distribution and pore spacing. The main parameters of the three networks are shown in the following table. All the parameters defined here are same as that defined in table 2.1.

Table 4.1 Parameters of the Three Pore Networks with Different Dimensions

Network Size	$\overline{r}$ (mm)	r_{min} (mm)	r_{max} (mm)	σ_r	n	σ_n	Curvature Constant
12-12-12	0.39	0.26	0.56	0.06	5	0.2	1.7
15-15-15	0.39	0.26	0.56	0.06	5	0.2	1.7
17-17-17	0.39	0.26	0.56	0.06	5	0.2	1.7

The air water two-phase flow was simulated in the three networks with macroscopic capillary number of 2.2E-3. The variation of air saturation over time in the three networks and the correlation between relative permeability and saturation of the networks are compared in the following parts.
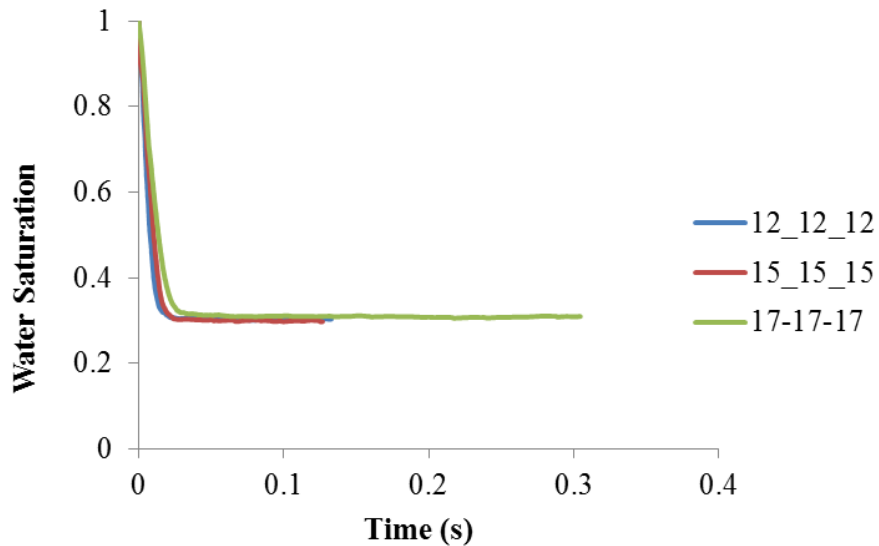

Figure 4.2 Temporal change of water saturation in the three pore networks.

Figure 4.2 shows the variations of saturation over time in the three networks. From this figure, two main types of information can be extracted: one is the changing rate of water saturation while the other one is residual water saturation. From Figure 4.2, it can be observed that the three curves almost overlap each other, which means the the three networks have same changing rate of water saturation and residual saturation. As shown in the above figure, for all the three pore networks, the saturation changing rate is a constant before 0.023 sec, and it reaches steady state after that. There are no obvious differences among the saturation changing rates in the three pore networks. As to the residual water saturations in the three pore networks, it is equal to around 0.3 for all the three networks. Be comparing the variation of water saturation over time shown in Figure 4.2, it can be preliminarily concluded that all the three size of networks can capture the variation of air/water saturation during air-water two phase flow through the network.

Although all the three networks can produce same results of changing rates of saturation and residual saturation, it does not mean all of them can produce same dynamic air water two-phase flow properties. One important dynamic properties of air water two-phase flow during air sparging is the air water spatial distribution as a function of saturation. With same water saturation, there may be different air water spatial distributions in the network. In order to consider air water spatial distribution, air and water relative permeabilities are introduced.

Relative permeability is defined as the ratio of the effective permeability of the porous medium to the absolute permeability of the porous medium, where the effective permeability of a permeable medium is a measure of the ability of the material to conduct one fluid phase of a multiphase fluid system. In the case of a multiphase system existing in

the medium, the ability of each fluid to flow is reduced by the presence of the other fluids in the system; as a result, the effective permeability for all fluid phase is less than the absolute permeability for single phase flow and the relative permeability is always less than one.

When air water two phases are present in the network, if flow rates are computed using the same pressure drop as for single-phase flow, then the relative permeability is:

$$k_{rw} = \frac{Q_{mw}}{Q_{sw}} = \frac{Q_{mw}\mu_w L}{K(P_{inlet} - P_{outlet})}$$ (4.1)

$$k_{rnw} = \frac{Q_{mnw}}{Q_{sw}} = \frac{Q_{mnw}\mu_{nw} L}{K(P_{inlet} - P_{outlet})}$$ (4.2)

Where μ_{nw} is the viscosity of air, Q_{mw} is the total flow rate of water across the network for air-water two phase flow, which is the water flow summed over all throats connected to the outlet, and Q_{mnw} is the total flow rate of air across the network for air-water two phase flow, which is the air flow summed over all bonds connected to the outlet. The total flow rate of both air and water across the network can be calculated based on the pressure field under each fluid configuration at each level of water saturation in the network. Please be noted here that in all the two formulae for calculating relative permeability, the flow rate of each phase is the outflow at the outlet of the network, so the flow of the isolated clusters of each phase in the network during the dynamic process is not considered. P_{inlet} and P_{outlet} are the pressure at the inlet and outlet of the network respectively. K is the absolute permeability of the network which can be calculated by Darcy's law:

$$K = \frac{\mu_w Q_{sw} L}{A(P_{inlet} - P_{outlet})}$$ (4.3)

Where μ_w is the viscosity of the water, Q_{sw} is the total flow rate across the network for single-phase flow of water (this is the flow summed over all throats connected to the inlet or outlet), A is the cross-sectional area of the network model and L is the axial size of the network.

In order to check whether all the three pore networks can capture the dynamic air water two-phase flow properties or not, the air/water relative permeabilities in the three networks are compared as shown in the following figure.

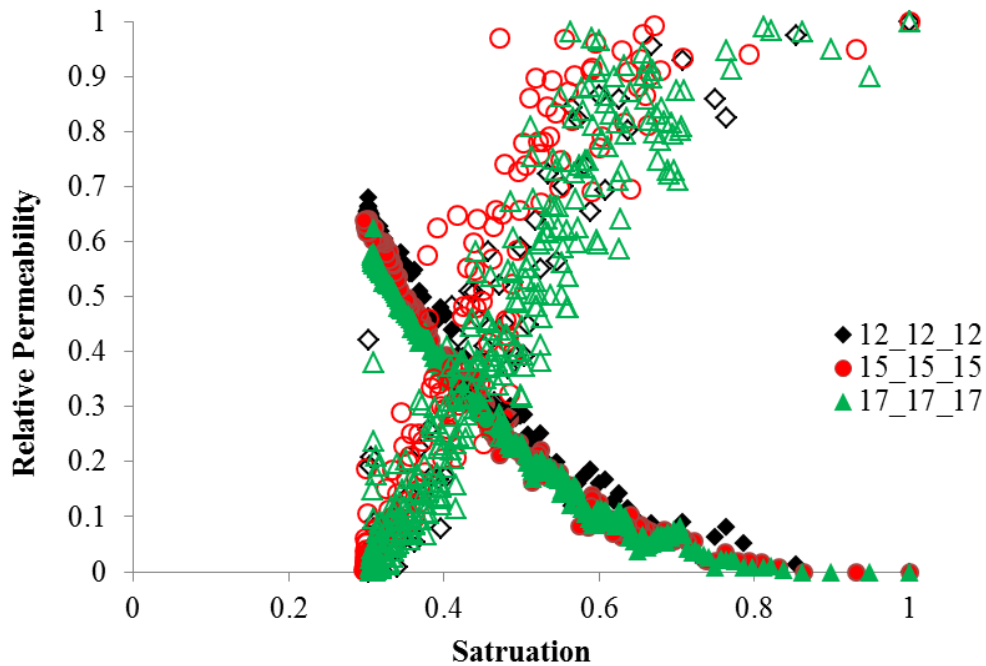**Figure 4.3** Relative permeabilities in the three pore networks.

In Figure 4.3, the solid symbols represent air relative permeabilities while the hollow ones represent the water relative permeabilities. It can be observed that the relative permeability of the three networks matches each other very well. As is known that, to some extent, the relative permeability can reflect the developed air flow channels in the

pore network. As the relative permeability curves in the three pore networks are almost identical to each other, it can be concluded that the air channel development in the three pore networks are almost same.

Based on the results in the above two figures, it can be concluded that the network with size of 12*12*12 can generate reasonable results as those by the network with size 15*15*15 and by the network with size of 17*17*17. As a result, in this research, the pore network size of 12*12*12 will be employed to conduct numerical experiments on air water two-phase flow in this research.

4.3   Simulation Results for One Step Air Injection Pressure

4.3.1   Introduction

A major difficulty in modeling multiphase flow comes from the constitutive relationship governing multiphase movement (Parker et al., 1987). The relationships are expressed as functional relationships of capillary pressure, saturation, relative permeabilities of coexisting phases. Capillary pressure-saturation equation such as Brook-Corey equation (Brooks and Corey, 1964) and van Genuchten equation (van Genuchten, 1980) are widely used to describe the relationship between the capillary pressure and effective saturation of a wetting fluid for multiphase flow. The effective saturation of a wetting fluid is defined by

$$s_{we} = \frac{s_w - s_{wr}}{1 - s_{wr}}$$
(4.4)

Where s_{we}, s_w, and s_{wr} are the effective water saturation, real water saturation, and irreducible water saturation, respectively. However, these capillary pressure-saturation correlations could not clearly consider the effect of flow dynamics. In addition, the

irreducible water saturation itself is not intrinsic property of porous medium and it is also affected by the air flow rate or air injection pressure. So in this section, effect of capillary number on changing rate of water saturation, residual saturation, dynamic phase transition and fractional flow are investigated.

In addition, in multiphase flow, each fluid is regarded as a continuum in a porous medium, and each fluid has its own flow pathway according to its saturation level. The permeability of each fluid within a porous medium is affected by the presence of the other phase. Under the extension of Darcy's law, the permeability of each fluid is called an effective permeability. The ratio of the effective permeability of each fluid to the permeability of a single-phase fluid is defined as relative permeability. Relative permeability is generally expressed as a function of fluid saturation. In water-gas fluid systems, Brooks and Corey parametric model yields the relative permeabilities of water and gas phase as follows (Brooks and Corey, 1964):

$$k_{rw} = s_{we}^{(2+3\lambda)/\lambda} \tag{4.5}$$

$$k_{rg} = c_k (1 - s_{we})^2 \left[1 - s_{we}^{(2+\lambda)/\lambda} \right] \tag{4.6}$$

And the van Genuchten model gives (van Genuchten, 1980)

$$k_{rw} = s_{we}^{1/2} \left[1 - (1 - s_{we}^{1/m})^m \right]^2 \tag{4.7}$$

$$k_{rg} = c_k (1 - s_{we})^{1/2} (1 - s_{we}^{1/m})^{2m} \tag{4.8}$$

Where k_{rw} and k_{rg} are relative permeabilities of water and gas phases, respectively, and c_k is the Klinkenberg factor, which accounts for the air slippage in air-water flow systems. From these two expressions of air and water relative permeability, it can be found that relative permeability is the function of saturation. In order to consider the dynamic effects of air water two-phase flow properties on the relative permeability, the relative permeability of air water two-phase flow under different capillary numbers are studied and compared.

4.3.2   Effect of Capillary Number on Residual Saturation

For a water-wet media, the wetting phase maintains connectivity for practically all saturation values through wetting layers in corners and films. The wetting films disjoin or rupture when the film thickness reaches molecular dimensions-this happens at extremely low wetting saturation. In addition, once the outlet fractional flow of non-wetting phase approaches unity, wetting phase saturation is never reduced to the extremely low values corresponding to true wetting residual. Based on this description of wetting phase movement, it is reasonable to assume that the residual saturation of water phase during air water two phase flow process is affected by the spatial distribution of the two phases during drainage and imbibition process, which is also controlled by the flow regimes. As we know, N_{ca} shows the competition between the driving force for removal of wetting phase (viscous force) and the retention force for the wetting phase (capillary force) in a porous medium and the flow regimes is determined by N_{ca}. So, there may be a correlation between residual saturation and capillary number.

In addition, as the capillary number represents the ratio between viscous force and capillary force and the capillary force is related to the pore size of the network, it is possible

that the residual saturation is also affected by the pore size of the network. This can be understood easily by considering flow in a network of interconnected capillary tubes. For example, there are two networks consisting of interconnected capillary tubes. One contains large inner diameter capillary tubes while the other one consists of tubes with small diameter. For the air water two-phase flow with same capillary number in the both networks, the flow rate in the network with small tubes must be higher than that in the network with large diameter tubes. As a result, it is possible that the development of flow paths is quite different in the two networks, which results in two different residual saturations in the two networks.

In this section, both the effects of capillary number and network pore size on the residual water saturation are studied. Three types of networks were employed in this research. The parameters of the three types of networks are shown in Table 4.2. The results of residual saturation are shown in Figure 4.4.

Table 4.2 Geometrical and Topological Parameters of the Three Pore Networks

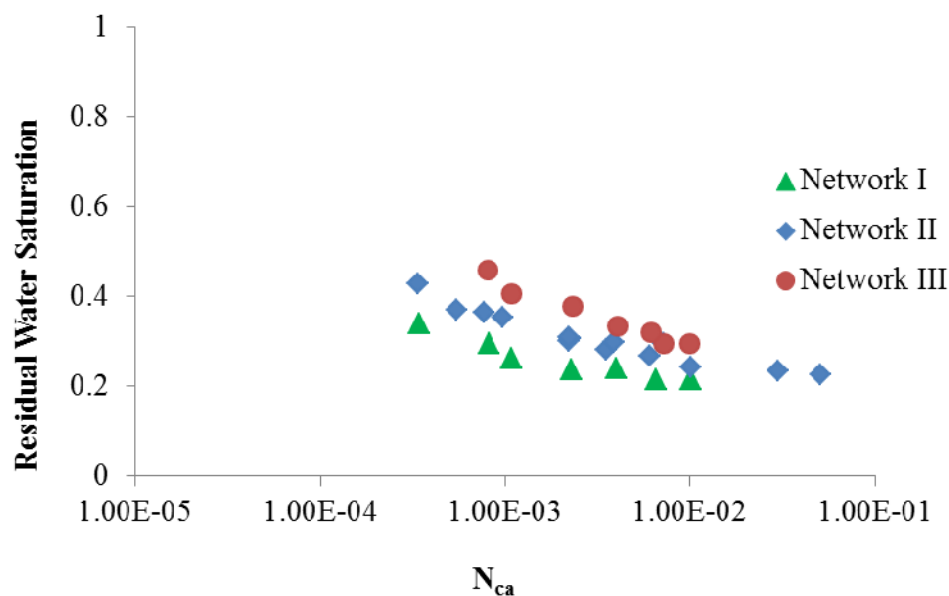| Network ID	Network Size	$\overline{r}$ (mm)	r_{min} (mm)	r_{max} (mm)	σ_r	n	σ_n
I	12-12-12	0.299	0.195	0.559	0.06	5	0.2
II	12-12-12	0.390	0.260	0.559	0.06	5	0.2
III	12-12-12	0.481	0.260	0.585	0.06	5	0.2

Figure 4.4 Variation of wetting residual with capillary number

Figure 4.4 shows the variation of wetting residual as a function capillary number for each network. It can be observed from the Figure 4.4 that the residual saturation increases monotonically with a decrease in capillary number. The overall trend of the correlation between saturation and capillary number for 3D porous media is consistent with the findings by Mohit Singh et al. (2003). For flow with high capillary number, the residual water saturation is lower than that with small capillary number. Based on this result, it can be concluded that residual saturation is not an intrinsic properties of porous medium and it is dependent on the flow dynamic of the two phase flow in the porous medium. However, comparing with the results by Mohit Singh et al. (2003), the value of residual saturation is higher in our study. The main reasons accounting for the differences are the description of the geometrical and topological properties of porous medium and the way of calculating water saturation. In this research, the bond connecting two neighboring pore bodies is in the converging-diverging shape while that in the research of Mohit Singh

et al. (2003) is in a shape of cylinder with constant cross sectional area. In this research, the coordination number is not a constant, however coordination number is a constant of 6 in Mohit (2003)'s research. In addition, in this research the saturation is calculated all over the 3D pore network which is also different from that calculated by researcher of Mohit Singh et al. (2003). According to Mohit Singh et al., the saturation is calculated as the saturation in a thin slice in the network.

In addition to the above conclusion that the residual saturation is affected by the capillary number during air-water two-phase flow, it can be also observed from the above figure that residual saturation is also dependent on the geometrical properties of the pore network. By comparing the residual saturation in the three networks it can be found that at same capillary number the residual saturation for the network with small pore size is lower that for the network with large pore size. One possible reason accounting for this is that for the two-phase flow with same capillary number in the two networks, the flow rate must be higher in the network with small pore size than that it in the other one as discussed before. With high flow rate, it is prone to develop more continuous air and water flow paths in the network with small pore size, on the contrary, with low flow rate; there are high possibilities of forming isolated water clusters or air clusters during two-phase flow in pore network with large pore size. As a result, the residual saturation in network with small pore size is higher than that in network with larger pore size.

4.3.3 Effect of Capillary Number on Dynamic Two-Phase Flow

On the microscopic level the fluids occupy separate interpenetrating networks, with flow in bonds between the two fluids inhibited by capillary pressure. Hence, the flow rates are reduced from the single phase value by a factor of k_r which is called the relative

permeability. In this section, the effects of capillary number on drainage relative permeability are studied.

Relative permeabilities are often plotted as a function of saturation; however, the changing rate of the saturation may also affect the relative permeability of each phase. In order to consider the effect of air flow dynamics on relative permeability, different air injection pressures or air injection rates are applied in the numerical experiments. In this research, five different air injection pressures were applied to the three types of networks with parameters given in Table 4.2 and the corresponding macroscopic capillary numbers were N_{ca}=5.5E-4, N_{ca}=7.6E-4, N_{ca}=6.1E-3, N_{ca}=2.2E-3, N_{ca}=3.0E-2. The results presented in this section are organized as follows: initially, the effect of capillary number on changing rate of saturation and on relative permeability in the network II will be studied; Then the simulation results in all the three networks will be compared to check whether this observations obtained in network II are consistent in the three networks or not. Finally, by comparing the simulation results in the three networks, it can be checked that whether the influences of capillary number on relative permeability are affected by the pore size or not.

The variation of saturation along with time during the air water two-phase flow in network II is plotted in the Figure 4.5.
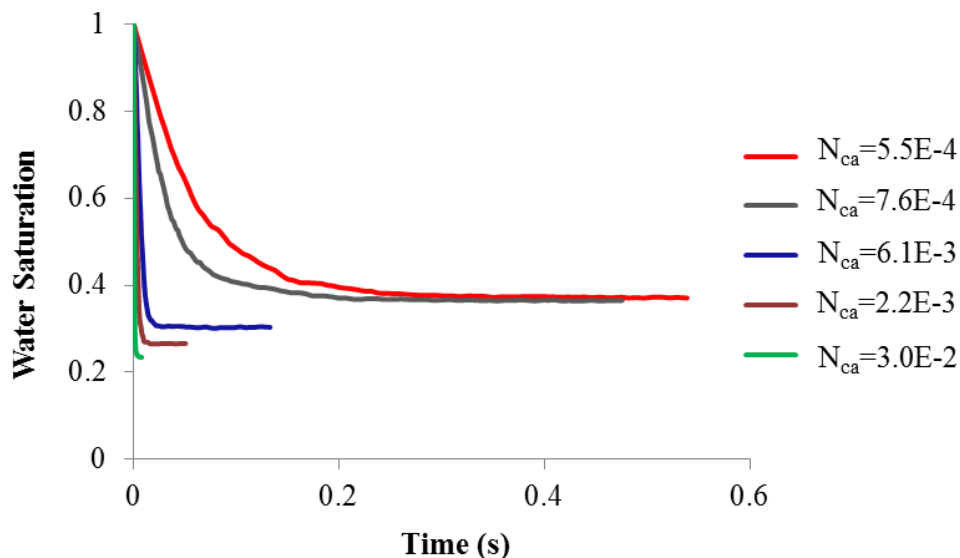
Figure 4.5 Temporal change of water saturation during air water two-phase flow in Network II.

Based on the results shown in Figure 4.5, two obvious conclusions can be drawn from this figure: 1. the residual saturation is affected by the capillary number, which is consistent with the conclusions about the effects of capillary number on residual saturation presented in previous section. As shown in this figure, the residual saturation for capillary number of 5.5E-4 is almost double of that for capillary number of 3.0E-2. 2. In addition, the changing rate of saturation increases greatly with the increasement of capillary number. As shown in the above figure, it takes less than 0.02s for air water two-phase flow with capillary number greater than 6.1E-3 to reach the steady state, however, it takes almost more than 0.2s for two-phase flow with capillary number smaller than 7.6E-4 to reach the steady state.

Next, the air relative permeability of two-phase flows with different N_{ca} are compared and presented in Figure 4.6.
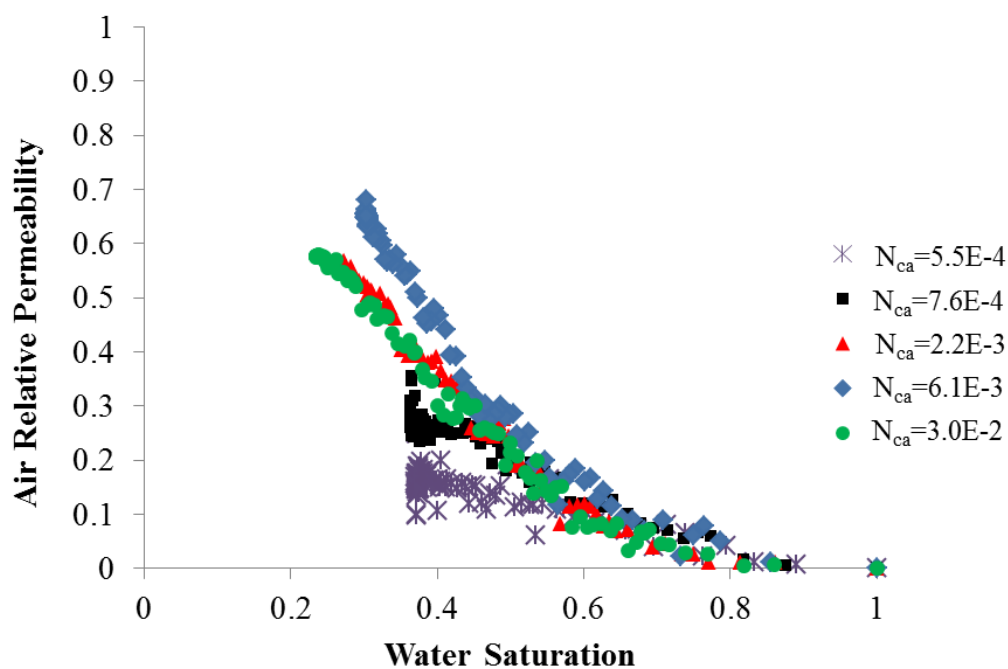
Figure 4.6 Air relative permeabilities for Network II

It can be observed in Figure 4.6 that for all the air relative permeability curves, there is a common trend that the air relative permeability is a function of saturation. This is consistent with our common knowledge on air relative permeability that the relative permeability is dependent upon the fluid saturation levels. During two-phase flow, as part of the pore space in the porous medium is occupied by one fluid of the multiphase fluid system, so the flow of another fluid is impeded and reduced. With the decrease of water saturation, more and more water is drained out leading to an increase of continuous air flow channels in the network, as a result, the relative permeability increases monotonically with the decrease of water saturation. As can be further observed from Figure 4.6 that for the water saturation higher than 0.8, all the air relative permeabilities for flows with all capillary numbers are almost zeros, which means at this water saturation, there is no breakthrough of air flow channels. Then as the water saturation decreases, the air relative

permeability increases monotonically. However, it does not reach 1 and it stops at certain water saturation depending on different capillary numbers. It can be observed from Figure 4.6 that, at same level of water saturation, the air relative permeability for the flow with smaller N_{ca} is much lower than that for the flow with high N_{ca}. For example, at the water saturation of 0.4, the air permeability for N_{ca}=5.5E-4 is less than 0.25, however, the air permeability for N_{ca}=6.1E-3 is almost equal to 0.5. The most possible reason account for this difference is the varied water/air spatial distribution in the network. In order the study this, the water saturation in each layer of the network is computed. For each layer, the water saturation is calculated based on the total volume of water in all pore bodies in that layer and in all the bonds between that layer and the adjacent layer below it. As the bottom layer is the inlet, so that layer is not considered in this calculation. The following two figures show the water saturation in each layer of the network at the average water saturation of the whole network equal to 0.5, 0.48, 0.46, 0.44, 0.42, and 0.4, respectively.
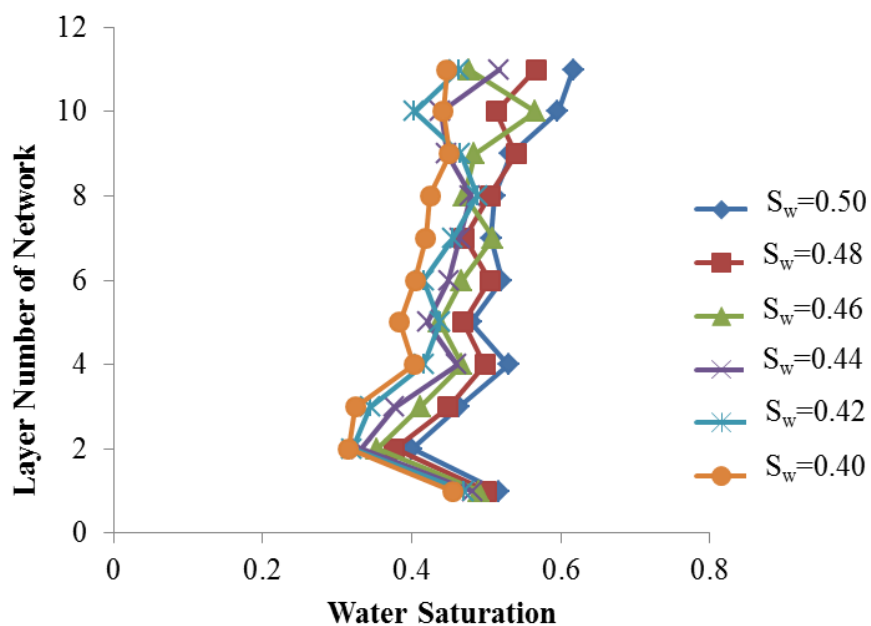
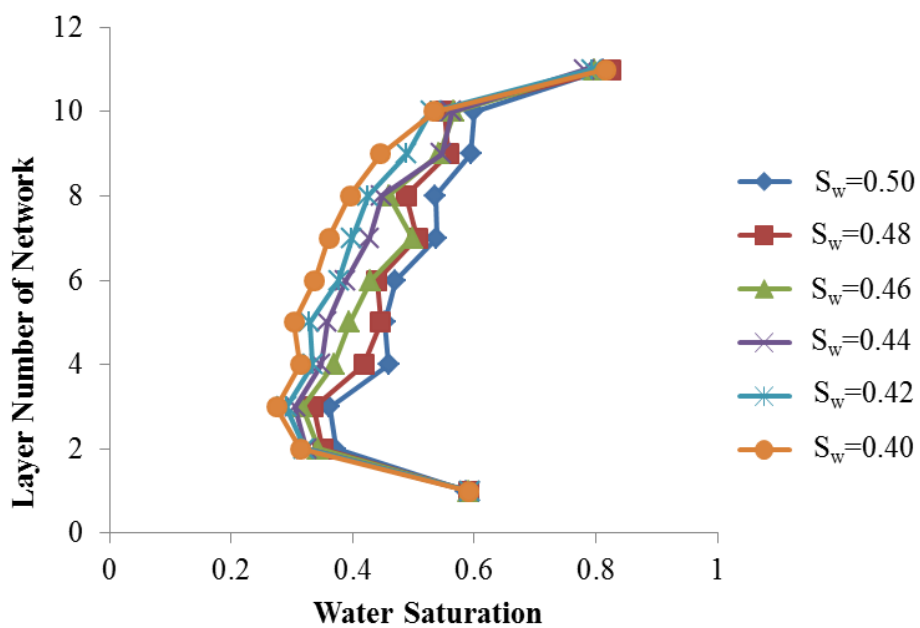**Figure 4.7** Front dynamics in Network II for N_{ca}=6.1E-3.

Figure 4.8 Front dynamics in Network II for N_{ca}=5.5E-4.

Figure 4 .7 shows the water saturation of each layer of the network at different water saturation levels with the capillary number N_{ca}=6.1E-3 while Figure 4.8 shows the

corresponding distribution of water saturation with capillary number N_{ca}=5.5E-4. By comparing Figure 4.7 and Figure 4.8, it can be concluded that the water spatial distributions is not only the function of water saturation, it is also affected by the capillary number. As can be observed from the two figures that the air phase is distributed more evenly during the flow with high capillary number than that during the flow with low capillary number. As we know, for more evenly distributed air phase, there are more continuous air-flow channels formed and more of the channels are accessible to flow and less displaced fluid is bypassed, which leads to higher air relative permeability. On the contrary, for the unevenly distributed air phase observed in Figure 4.8 for the flow with low capillary number, because the flow is dominated by capillary forces, so the nonwetting fluid occupied the wider bonds or larger pore bodies while the much of the displaced fluid resides in disconnected blobs, which do not contribute to the flow. This can explain the influence of capillary number on relative permeability shown in the Figure 4.6. Finally, it comes to the conclusion that during air water two-phase flow air spatial distribution is not only the function water saturation and it is also affected by the capillary number. The air relative permeability which is usually considered as a function of water saturation highly depends on the air/water spatial distribution during air water two-phase flow. As a result, the air relative permeability does not only depend on the air/water saturation; but also depends on the capillary number which determines the air flow rate and air spatial distribution in the network.

In the Figure 4.9, both air and water relative permeabilities are presented for flows with different capillary numbers. The solid points denote the air permeability while the hollow ones represent the water permeability.
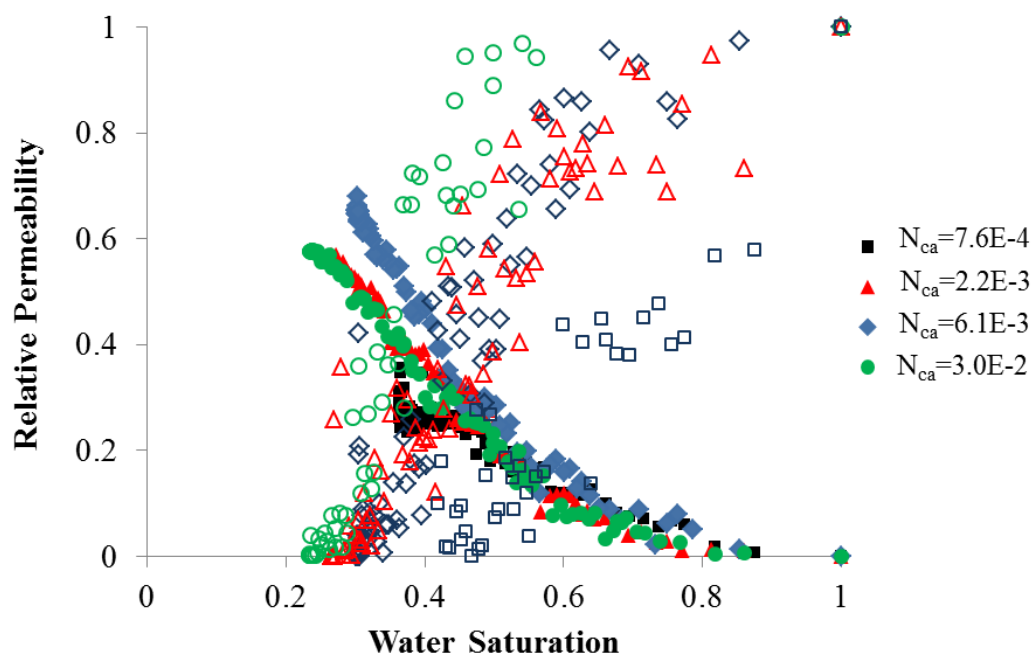
Figure 4.9 Air-water relative permeabilities for Network II.

From this figure, it can be obviously observed that the water relative permeabilities are more scattered than air permeabilities. The main reason accounting for this is that contrary to the flow pattern transition of air which is transferred from disconnected phase to connected phase, the water phase is changed from continuous phase to discrete phase during the dynamic air water two-phase flow. As a result, there are lots of isolated water clusters formed during the two-phase flow process in the network. The connection among these isolated water clusters vary with the time and water saturation. This accounts for the scattered points shown in the Figure 4.9. However, there is an overall trend that with more water are drained out during air water two phase flow, the water relative permeabilities for all flows with different capillary numbers are decreasing. By comparing the water relative permeability for flow with different capillary numbers, it can be further observed that the there is a general trend that at a certain water saturation level, the water relative

permeability for the flow with high capillary number is higher than that with low capillary number. However, this trend is not very clear due to the scattered points, which will be further investigated by the simulation in the other two networks.

In addition, it can be found from the figure that the sum of the two relative permeabilities is less than unity showing that the two-phase flow always retards the overall flow. This happens because some interfaces are "frozen" or "capillary blocked" and this imparts non-liner saturation dependence to relative permeability (Singh, et al., 2003).

In order to further verify what are observed from the simulation in the network II, the air water two-phase flow was also simulated in the network I and network III with the geometrical and topological parameters shown in table 4.2. Figure 4.10 and Figure 4.11 show the temporal variation of water saturation in the network I and network III respectively while Figure 4.12 and Figure 4.13 show the air/water relative permeabilities in the network I and network III during the two-phase flow with different capillary numbers respectively.

Figure 4.10 Temporal change of water saturation during air water two-phase flow in Network I.

Figure 4.11 Temporal change of water saturation during air water two-phase flow in Network III.

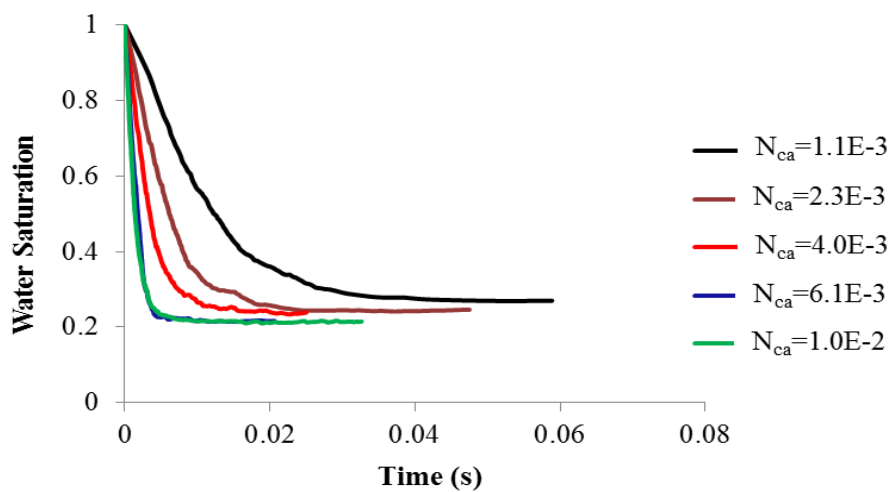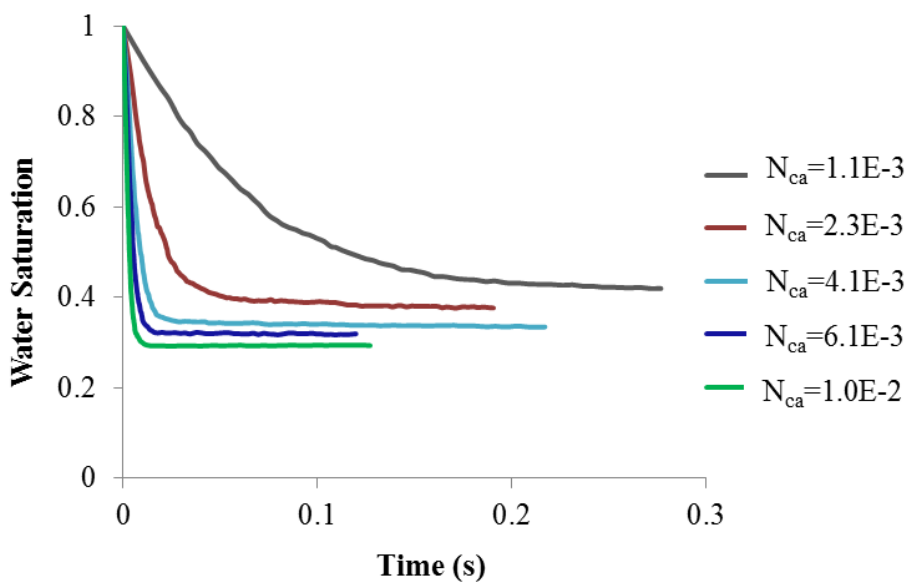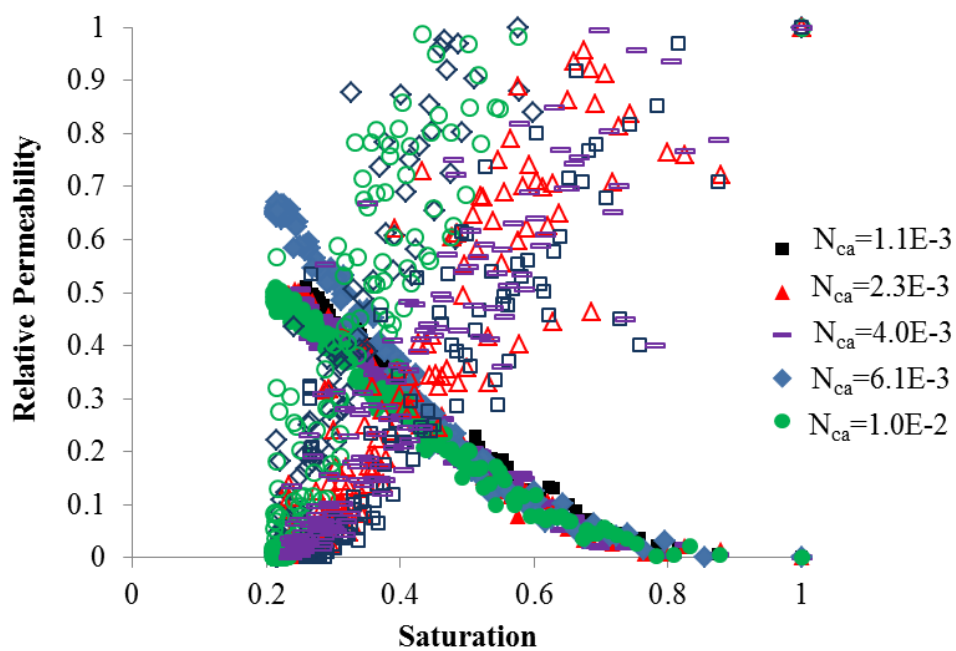**Figure 4.12** Air-Water relative permeabilities for Network I.
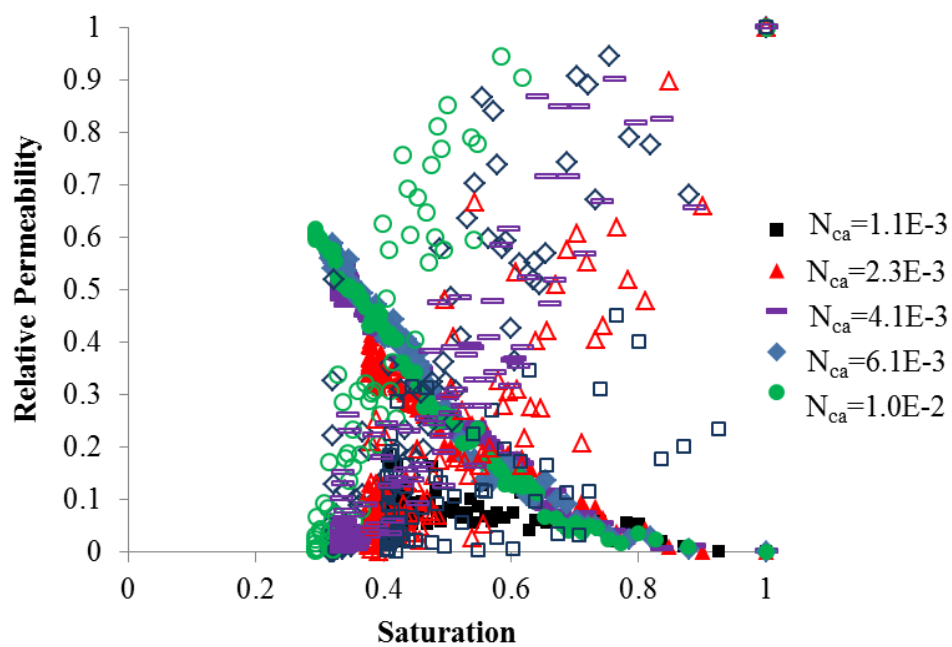

Figure 4.13 Air-Water relative permeabilities for Network III.

Figure 4.10 and Figure 4.11 verify the main conclusions on the temporal change of water saturation drawn from the simulation results in Network II that, the residual saturation is affected by the capillary number and high capillary number leads to lower residual saturation. In addition, the changing rate of saturation increases greatly with the increase of capillary number. Besides these conclusions, by comparing the variation of water saturation over time in the three networks, it can be further observed that the changing rate of saturation in the network III with large pore size is lower than that in the network I with small pore size for the two-phase flow with same capillary number. For example, for the flow with capillary number of 1.3E-3, it takes about 0.04s to reach equilibrium in Network I while it takes more than 0.2s to reach equilibrium in Network III which is almost 5 times of that in Network I. This phenomenon will be further studied in the next section which focuses on the effect of pore size on two-phase flow properties in network.

From Figure 4.12 and Figure 4.13, it can be observed that water relativity is more scatted than air permeability, which verifies the observation based on Figure 4.9. There is an overall trend that with decrease of water saturation in the soil, the water relative permeability for all flows with different capillary number are decreasing while the corresponding air relative permeability are increasing. At the same level of water saturation, water relative permeability for flow with high capillary number is higher than that with lower capillary numbers while air relative permeability has opposite situations. By comparing Figure 4.12 and Figure 4.13, it can be further observed that the difference among the air/water relative permeabilities for flows with different capillary numbers is

more apparent for Network III with larger pore size than that for Network I with small pore size.

4.3.4 Effect of Pore Size on Dynamic Two-Phase Flow

According to the Section 4.3.2 and the Section 4.3.3, it can be concluded that both the residual saturation and relative permeability are affected by the capillary number, however, it does not show that the capillary number is the only factor that affects the residual saturation and relative permeability. Both the residual saturation and relative permeability should be also affected by the geometrical and topological properteis of pore network. Actually, according to the observation during experimetnal study of air sparging by Hu et al. (2010), particle size of porous medium is one important factor always affecting the air spatial distribution of air in the soil. In this section, the dynamic flow of air water two-phase flow with same capillary number in the three types of networks with geometrical properties and topological properties shown in table 4.2 is studied. The temporal change of water satruation and air/water relative permealibties during the dynamic two-phase flow are studied. In order to check the reproducibility of the simulation results, the simulation tests in the three networks were conducted three times with three different capilalry numbers: N_{ca}=2.2E-3, N_{ca}=6.1E-3 and N_{ca}=1.0E-2. The detailed analysis will be provided to the test results for the capillary number of N_{ca}=6.1E-3 while the presence and discussions on the results for the other two capillary numbers is on the purpose of verifying the observation and analysis for the simualtion results for capillary number of N_{ca}=6.1E-3. Firstly, the temporal change of water saturation for N_{ca}=6.1E-3 is presented in the following Figure 4.14.
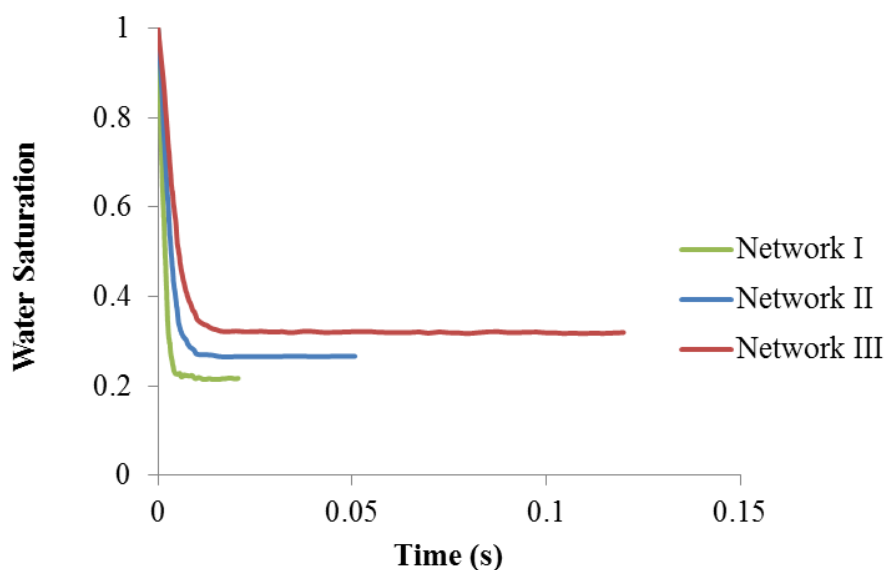
Figure 4.14 Temporal change of water saturation during air water two-phase flow for N_{ca}=6.1E-3.

From Figure 4.14 it can be observed that for the flow with same capillary number in the three networks the changing rate of water saturation for the network with small pore size is higher than that with larger pore size. Also the residual water saturation of the network with small pore size is smaller than that with large pore size. By considering the effects of capilary number on temporal change of water saturation discussed in the previous section, it can be concluded here that both changing rate of water saturation and residual water saturation are not only affected by the capillar number but also affected by the geomerical and topological properties of network. The main reason accounting for the effect of pore size on changing rate of water saturaiton is the different air-water flow rates in the three networks. With the same capillary number of all the three networks, the injection pressure for the network I should be much higher than that for network II and network III for them to maintain same capillary number. Then, higher pressures lead to more driving force for the wetting phase to be removed from the medium and lead to high

changing rate of saturation and lower wetting residuals. In addition, during air water two-phase flow in the network the pore-body/bond radius controls local imbibition rate, hence, having bigger pore bodies/bonds causes more trapping of the wetting phase which leads to higher wetting residuals.

The air relative permeablities and water relative permeabilities for the three networks are also calculated and shown in the following figure.
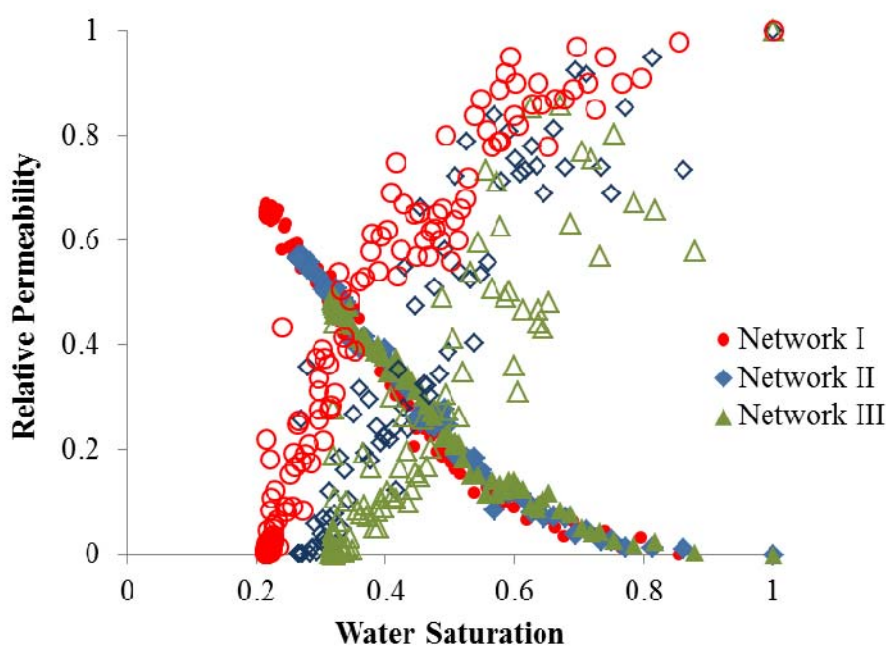
Figure 4.15 Air-water relative permeabilities in the three networks for N_{ca}=6.1E-3.

The above figure shows the air water relative permeabilities of the three networks for the flow with capilalry number of N_{ca}=6.1E-3. From the figure it can be observed that both the air permeabilty and water permeability are affected by the geometry of the pore network, however, the geometrical properteis of the network affect them in different ways. As to the air permeability, for the water saturation higher than 0.3 in all the three networks, there are no apparent differneces among the air relative permeabilities of the three networks. The curves of the air relativer permeablity of the three network almost overlap

each other. For the water saturation less than 0.3, there are big difference among the three air permeablities. For the network III the water saturation cannnot be reduced futher and the minimum water saturation during the simulation is around 0.3 with the corresponding air permeability of less than 0.5. For the network I and network II, the water satruation can be reduced further to 0.2 and 0.25 respectively with the highest air relative permeability around 0.65 for network I and around 0.55 for network III, repectively. As to the water permeablity, the water permeabilities in the three networks are affected by the geometry of the networks in a clear way, although the results of water saturation is more scattered than that of air permeability. As shown in Figure 4.15 that at a certain level of water saturation, the water permeability of small pore size network is higher than that of the network with large pore size. The most reasonable explaination for this effect is that in the network with the larger pore size, there is higher possiblity of forming isolated clusters of wetting phase that than in the network with small pore size.

In order the further verify the above observations for the capillary number of N_{ca}=6.1E-3, the whole simulations were repeated in the three networks for flow with capillary number of N_{ca}=2.2E-3 and for flow with capillary number of N_{ca}=1.0E-2.
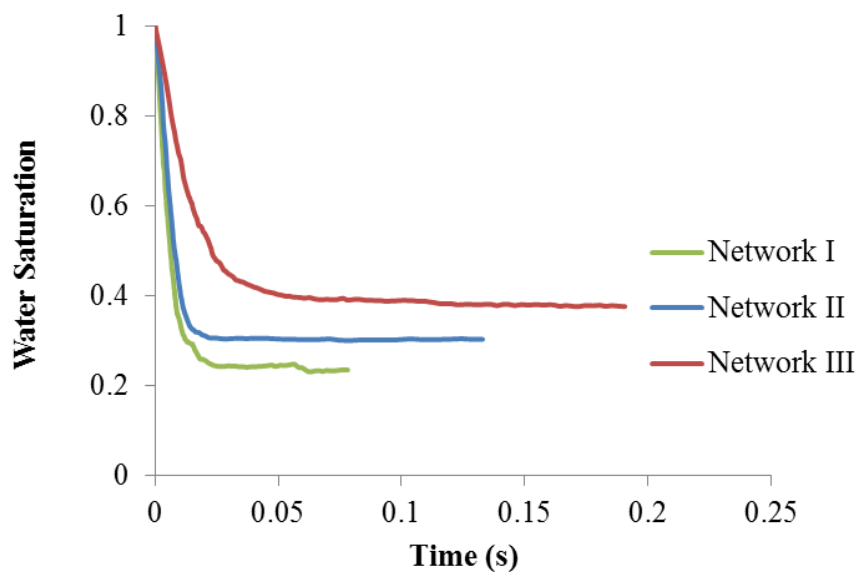
Figure 4.16 Temporal change of water saturation during air water two-phase flow for N_{ca}=2.2E-3.
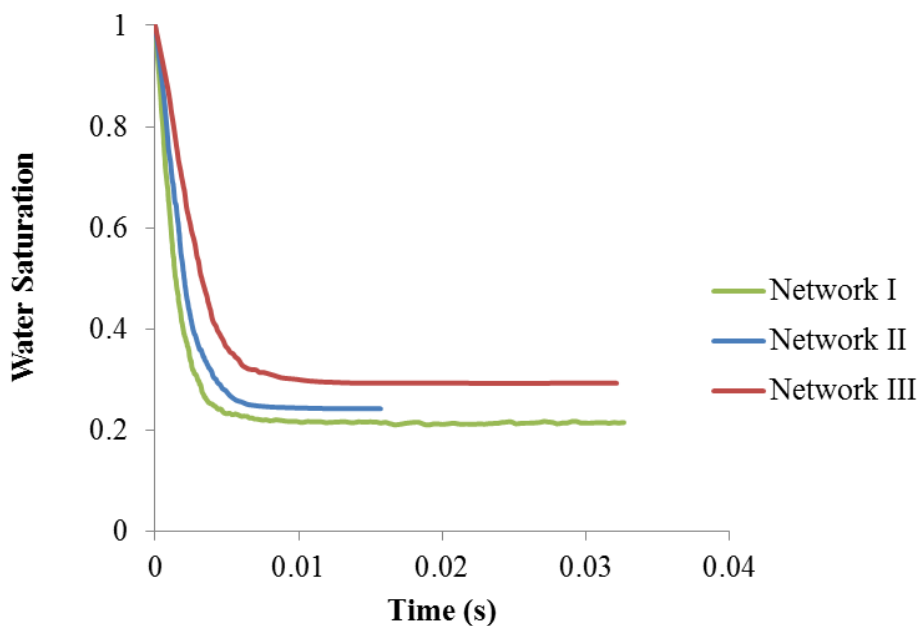
Figure 4.17 Temporal change of water saturation during air water two-phase flow for N_{ca}=1.0E-2.

The temporal changes of water saturation shown in both Figure 4.16 and Figure

4.17 futher verify that the changing rate of water saturation for the network with small

pore size is higher than that for the network with larger pore size and the differences between the changing rate for networks with different pore sizes are even larger for the low capillary number than that for the high capillary number. It also verifies that the residual water saturation of the network with small pore size is smaller than that with large pore size. The differences among the residual water saturation for the three networks become greater for the flow with lower capillary number. As shown in Figure 4.16 which is for the capillary number of N_{ca}=2.2E-3, the difference between the residual saturation for Network I and network III is about 0.2 while the correspondind difference for the capillary number of N_{ca}=1.0E-2 is only half of that.
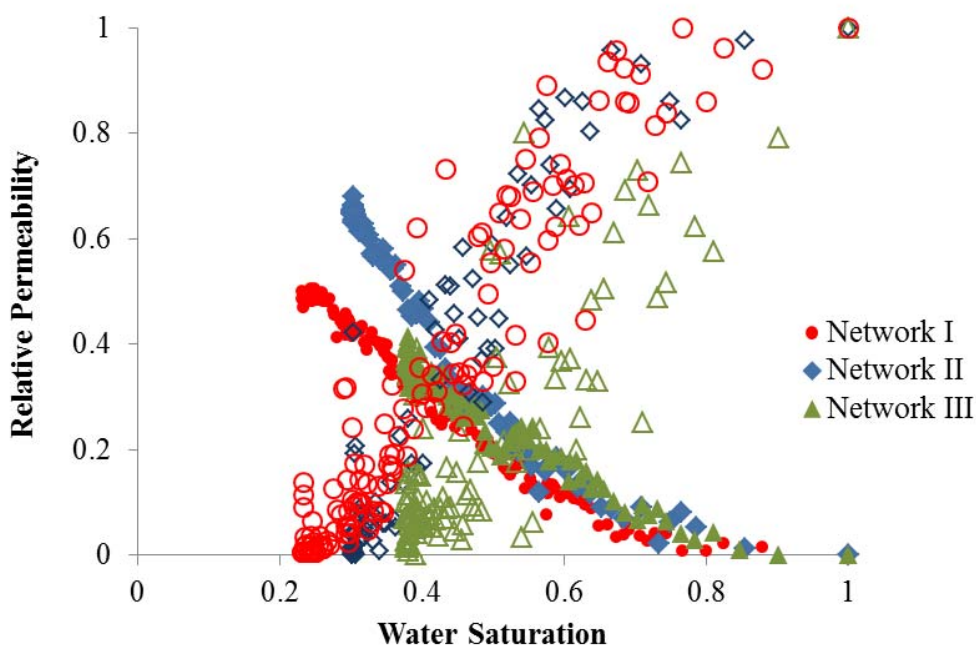
Figure 4.18 Air-Water relative permeabilities in the three networks for N_{ca}=2.2E-3.
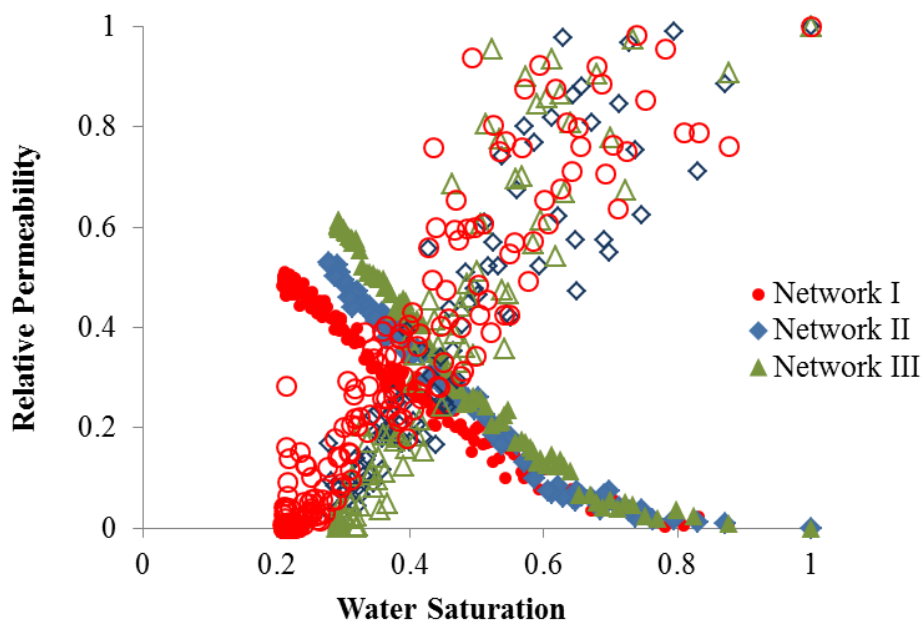
Figure 4.19 Air-Water relative permeabilities in the three networks for N_{ca}=1.0E-2.

By comparing the Figure 4.18 and Figure 4.19, it confirms the preliminary conclusions drawn from Figure 4.15 that at high water saturation (e.g., S_w>0.4), the air permeability is not affected by the geometry of the network, however, at low water saturation, the effect of geometrical properties of network on the air relative permeability becomes obvious.

Figure 4.18 and Figure 4.19 also verify that the water relative permeability for the network with small pore size is higher than that for the network with large pore size at low capillary number. However, the effect of the geometrical properties of pore network on water saturation becomes negligible at high capillary number. The main reason accounting for this is that in the network with larger pore size, the wetting phase is prone to be isolated by the injected nonwetting phase (air), as a result, the water relative permeability for the network with large pore size is usually lower than that for the network with small pore size. This is especial the case for the flow with low capillary number. However, for the flow

with high capillary number, as the flow rate the nonwetting phase is very high, it is possible to move the isolated wetting phase from the network, as a result, the difference between the water relative permeabilities for the networks with different pore sizes becomes smaller.

4.3.5 Capillary Force-Saturation Curve

The description of how an interface moves through a node and into connecting tubes is somewhat more difficult. In drainage, the capillary pressure is a force opposing the movement of the interface. When the position of interface is changed, the geometrical shape of the interface is changed, thereby changing the capillary pressure, as a result, in order to track the movement interfaces, the interfacial area weighted capillary forces can be recorded as an indicator of movement of air water interfaces.

As to regular primary drainage Pc-S curve, the capillary pressure is defined to be

$$P_c(S) = P_{bottom} - P_{top} \tag{4.9}$$

Where P_{bottom} is the air injection pressure at the bottom of the network and P_{top} is the boundary pressure at the top of the network.

Here, a new definition of macroscopic capillary pressure based on the average of local capillary pressure of pore bodies, weighted by the corresponding interfacial area A_i^{nw} is presented, which is also employed by Niasar et al. (2010) in their research on non-equilibrium effects in capillarity and interfacial are in two-phase flow.

$$P^c = \frac{\sum_{i=1}^{nb} p_i^c A_i^{nw}}{\sum_{i=1}^{nb} A_i^{nw}} \tag{4.10}$$

Then the average capillary force defined in Equation 4.10 is calculated during the flow with different capillary numbers in the network I and network II at each saturation level. The variations of average capillary pressure with water saturation for the two networks are shown in the following two figures.
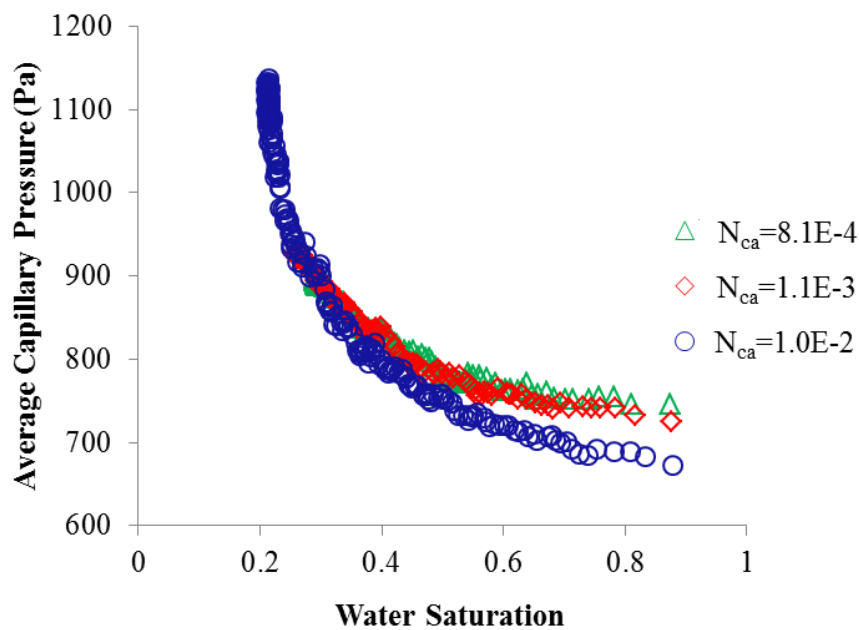
Figure 4.20 Variation of interfacial area weighted capillary pressure for Network I.
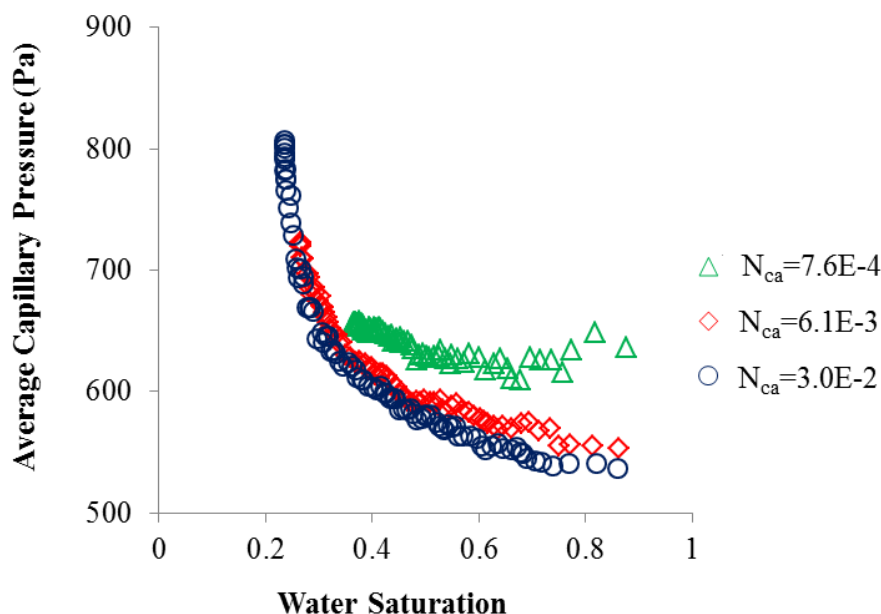
Figure 4.21 Variation of interfacial area weighted capillalry pressure for Network II.

From Figure 4.20, a common trend of changing of capillary pressure over water saturation for the flows with three difference capillary numbers is that as the water saturation decreases during the drainage process, the average capillary pressure increases. Based on this observation a preliminary conclusion can be drawn is that during the drainage process in the network the larger pores are always filled with the injected air first due to the less resistance than that of the small pores. Then, as more large pores are drained out by the injected air, the water saturation is decreased, meanwhile, if the steady state has not been reached, the pores with smaller pore sizes will be drained, leading to an increase of capillary force. By further comparing the maximum capillary force in Figure 4.20 for the flows with three different capillary numbers, it can be found that the maximum capillary force for high capillary number is much higher than that for the low capillary number. For example, as shown in Figure 4.20, the maximum capillary pressure for N_{ca}=1.0E-2 is about

1150Pa while that for N_{ca}=1.1E-3 is about 950Pa. This result is consistent with the conclusion drawn from section 4.3.2 that flow with high capillary number leads to a low residual saturation. For the flow with capillary number of N_{ca}=1.0E-2, as it is higher than that with capillary number of N_{ca}=1.1E-3, more small pores and bonds will be drained out at the end of the drainage process than that for the other one. So the maximum capillary pressure of it is much higher than that of the low capillary number. Figure 4.21 can also verify the above observations.

There is another obvious effect of the capillary number on the varation of capillary pressure with water saturation during the initial stage of drainge process that the capillary forces for the flow with low capillary number are higher than that with high capillary number. This seems contradicting our knowledge on the two-phase flow process. According to our common knowledge on the air water two-phase flow that for the flow with low capillary number, the air injection pressure is lower than that with high capillary number, as a result, the capillary force for the flow with low capillary number should be smaller than that for the flow with high capillary number. Actually, the results shown in both Figure 4.20 and Figure 4.21 are not contradicting the above discussions. The above discussion of our common knowledge on the drainage process is based on the flow at steady state or based on the drainage process with very low drainage speed. During the dynamic process, it is a little bit different from that. During the initial stage of the drainage process, for the flow with high capillary number, it has very high flow rate during the drainge process compared with that for the flow with low capillary number. As a result, the large pore and bonds can be filled by the injected air instantly after the drainage process. As to the slow drainage process, the drainage or imbibition in bonds or pore bodies is

dominated by the capillary force. If the injection pressure is higher than the local capillary force in the bonds or pore bodies, the drainage will occur. So at the same water saturation level during the initial stage of drainage process, there are more small bonds or pores got drained during the flow with low capillary number than that with high capillary number. This is especial the case when the injection pressure for both the flow with high capillary number and the flow with low capillary number is higher than the average capillary pressure of the network calculated based on the pore size and bond size in the network. So it can be found that differenc among the capillary pressures for flow with different capillary numbers is more obvious in Network II than that in Network I.

4.3.6   Dynamic Phase Transition

In steady flow the volume fractions of the wetting and the nonwetting phase will not change along with time. However, during transient flow condition, the nonwetting fractional flow should be a function of nonwetting saturation. Here the nonwetting fractional flow is defined same as that by (Henning et al., 2006):

$$F_{nw} = \frac{Q_{nw}}{Q_{inj}}$$

(4.11)

Where Q_{inj} is the total air injection rate at the bottom of the network and Q_{nw} is the total air outflow rate at the top of the network.

The nonwetting fractional flows for different flow at different capillary numbers in Network II are compared in the following figure:
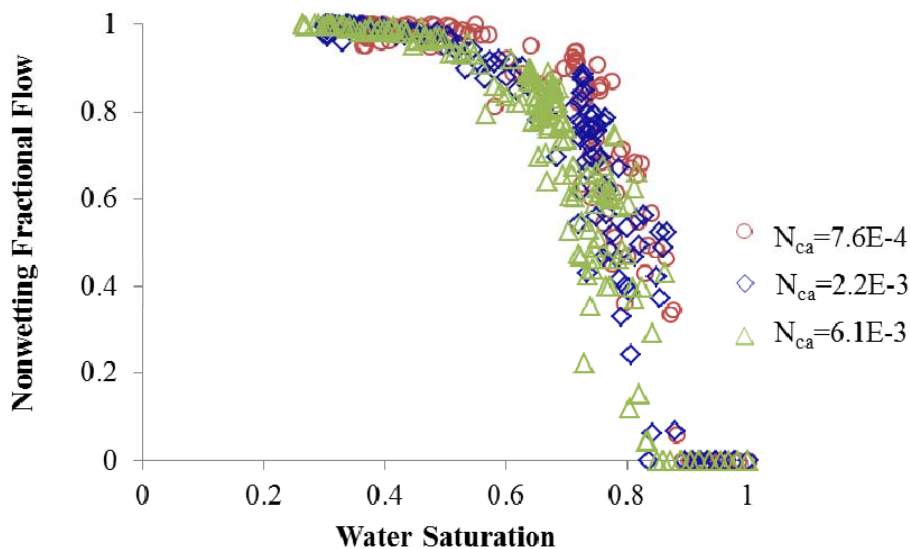
Figure 4.22 Nonwetting fractional flow for different capillary numbers in Network II.

As illustrated in this figure, fractional flow curves can be divided into three segments which are corresponding to the three stage of air water two-phase flow during air sparging. Stage one is the initial stage after injecting the air into the soil during which the water saturation is higher than 0.8 ($S_w \geq 0.8$). In this stage, the nonwetting fractional flow is almost equal to zeros for all flows with the three capillary numbers which means there is no breakthrough and only the wetting phase flow out of the network. Stage three is the ending stage of the air sparging during which the water saturation is lower than around 0.4, and the steady state is almost reached. In this stage, the nonwetting fractional flow is almost equal to 1, which means only the nonwetting phase flows out of the network. Stage two is the stage between the stage 1 and stage 3, which is a two-phase flow region. The cross-overs from single-phase flow to two-phase flow are dynamical phase transitions.

The effect of capillary number on the nonwetting fraction can also be observed from this figure. From the Figure 4.22, it can be found that for the flow with high capillary number, the transition water saturation between the stage 1 and stage 2 is higher than that for low capillary number which is consistent with our knowledge about the flow regimes. With low capillary number, the flow pattern is more likely to be the capillary finger; as a result, the saturation is much lower than that for viscous finger at breakthrough the transition water saturation. It can also be further found from the Figure 4.22 that for the flow with high capillary number, it reaches the steady state at lower water saturation than that for flow with low capillary number. This is also consistent with the conclusion drawn in the previous section about the effects of capillary number on residual saturation. In the stage 2, there is no clear trend shows the influence of capillary number on nonwetting fractional flow.

The effect of pore size on nonwetting fraction flow is also studied in this section. The three networks used in the Section 4.3.4 are employed here. The parameters of the three networks are shown in the Table 4.2, with average pore size 0.3mm for Network I, average pore size of 0.39mm for Network II and average pore size of 0.48mm for Network III. The comparisons of the three types of networks are shown in the Figure 4.23.
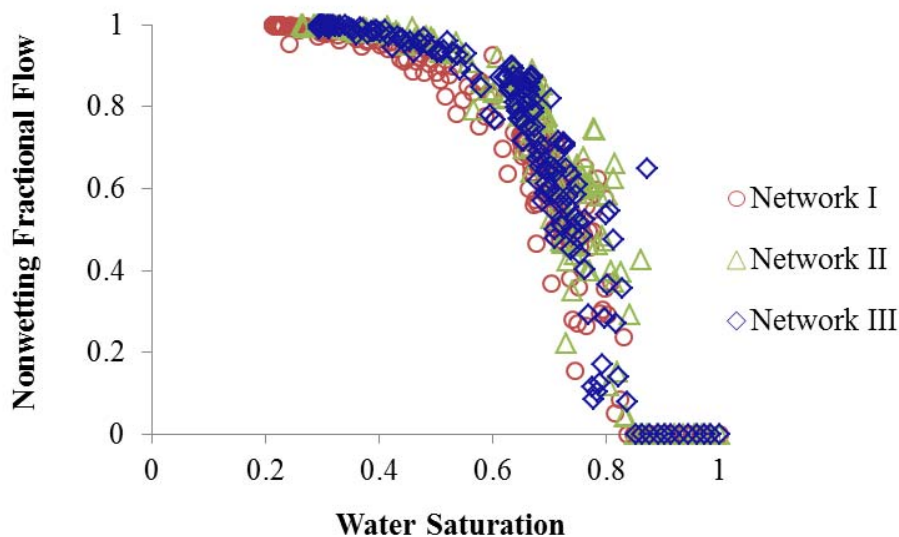
Figure 4.23 Nonwetting fractional flow for different networks.

According to this figure, similar conclusions about dividing the air sparging process into three stages can be drawn. But there is not abivious trend about the effect of the pore size on nonwetting fractional flow for flow with same capillary number in the three different networks in the stage 1 and stage 2. The only difference among the three networks occurs in stage 3. As shown in Figure 4.23, the flow in the network with lager pore size reaches the steady state at higher water saturaiton than the flow in the network with small pore size. For example, the flow in the network III reaches the steady state at higher water saturation than that for network I and network II. This is consisent with conclusion on the effect of pore size on residual saturation metioned in previous sections.

4.4   Simulation Results for Multistep Air Injection Pressure

4.4.1   Introduction

As mentioned in the Section 4.1, in order to bridge the gap between the pore scale and the porous-medium-continuum scale, the air-water two phase flow process simulated at pore scale can be translated into functional relationships between continuum-scale variables. There are two main functional relationships: one is the functional relationship between capillary force and saturation and the other one is the functional relationship between relative permeability and saturation.

In the Section 4.3, the dynamic two-phase flow properties have been studied by tests with one-step air injection pressure. However, during one-step pressure tests the capillary pressure cannot be obtained as the boundary pressures are maintained as constant during the whole process. In addition, usually multistep pressures are applied during air sparging process; as a result, it is necessary to study the effect of pressure steps on the dynamic flow properties. In this section, the numerical tests with multistep pressures are performed and the capillary pressure curves both at the steady state and the transient state are studied. The dynamic effects on the air/water relative permeabilities during multistep pressure drainage are also studied.

4.4.2   Steady-State Capillary Pressure Curve

In this section, a stepwise change of water pressure was injected to the network and the maximum air injection pressure is 20kPa with the corresponding macroscopic capillary number defined in section 4.2.1 N_{ca}=6.1E-3. The numerical experiments were conducted with four different pressure steps: 5 steps, 10 steps, 20 steps and 40 steps with corresponding pressure steps of 4000Pa, 2000Pa, 1000Pa and 500Pa respectively.

During the numerical experiment, the network was initially completely filled with wetting fluid connected to a reservoir at the top boundary at a given pressure. The pressure at the bottom boundary was then increased by a specified pressure step Δp until the nonwetting fluid started to invade the network. After that the bottom pressure was increased by the pressure step each time and the pressure was maintained until the air-water distribution reaches a stable configuration. The steady state can be determined by calculating the changing rate of the saturation of the whole network. Repeated simulation process like this for a sequence of imposed injection pressure allows a complete injection pressure-water saturation curve. The main results of the simulation of air-water two-phase flow are presented in the following part of this section.
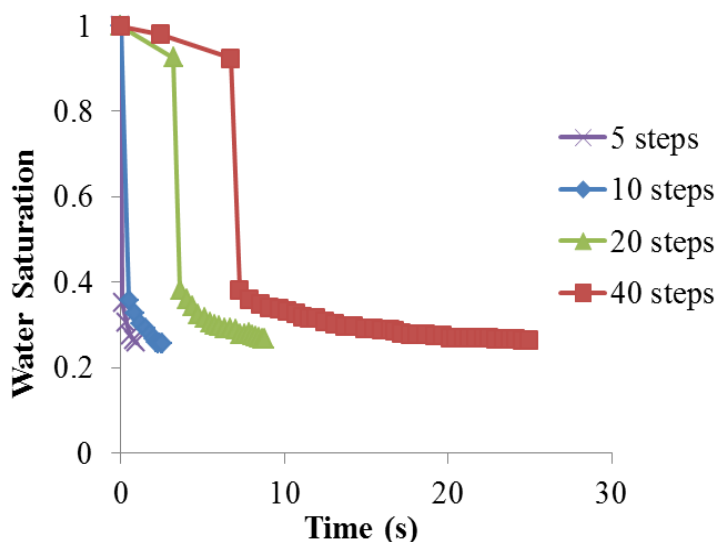

Figure 4.24 Temporal change of water saturation during air water two-phase flow for multistep pressure.

In Figure 4.24, the saturation is plotted as a function of time. From the Figure 4.24, an obvious characteristic of the temporal change of the water saturation can be observed is that for the flow at each pressure step, there is an abrupt change of saturation during the

initial stage of the two-phase flow before the water satruation reaches 0.4. Then, after that, the changing rate of water saturation becomes very small. For example, as shown in Figure 4.27, for the 5-step and 10-step pressure, the water saturation of the network dropped from 1.0 to 0.4 during the first step of the air injection pressure while for the 20-step and 40-step injection pressure, the water saturation of the network dropped to 0.4 after the second and third step of the injection pressure respectively. Then after that, the water satruation changes very slows for all injection pressure. Why is there a main decrease of the water saturation before the water saturation reaches 0.4? This can be explained by movement of ganglia of wetting fluid. During the initial stage of air-water two phase flow, the wetting phase is transited from continuous phase to disconnected from the reservoir. After nonwetting breakthrough at round water saturaiton equal to 0.8 which can be obtained from Figure 4.22, the flow rate of the injection air is greately increased. Under the condition of high flow rate, some of these ganglia can be mobilized leading to an abrupt decrease of water saturation. Figure 4.25 shows the saturation of each layer of the network at different saturation levels. As can be observed in this figure that after the water saturation reach 0.4, the difference between the water saturation of the top layer and that of the bottom becomes very small, which means most of the air flow channels have been developed at this saturation level. This result is consisent with the results of phase transition shown in Figure 4.22. As shown in Figure 4.22 that the nonwetting fraction flow is almost equal to 1 once the water saturation is lower then 0.4.
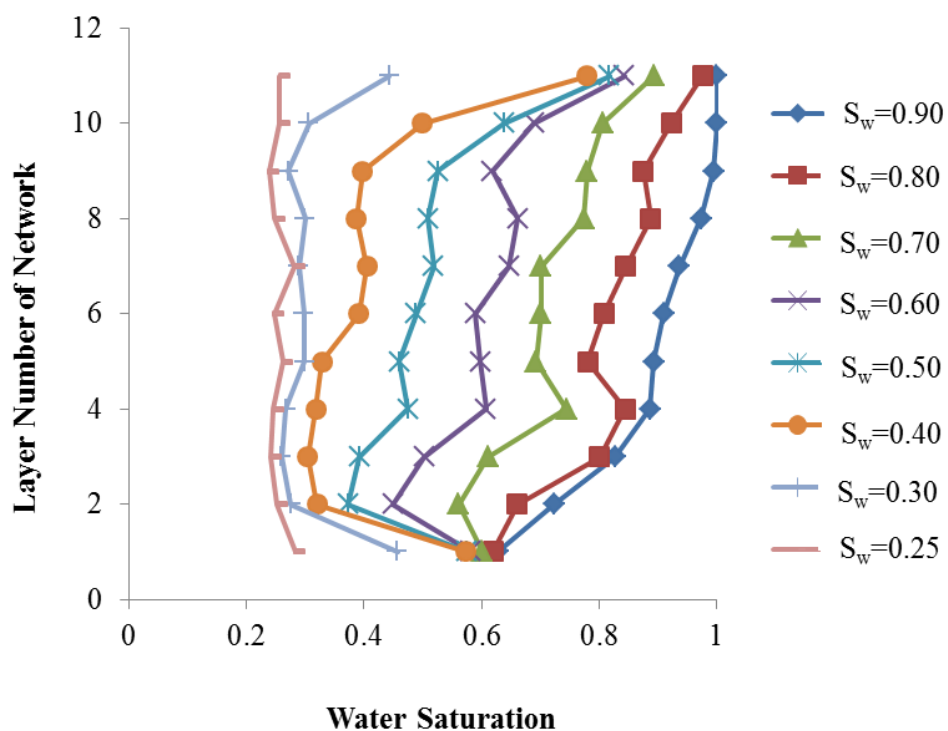
Figure 4.25 Variation of water saturation over network layers.

Figure 4.26 shows the correlation between the air injection pressure and water saturation for different pressure steps. This correlation between air injection pressure and water saturation is the correlation at steady state.
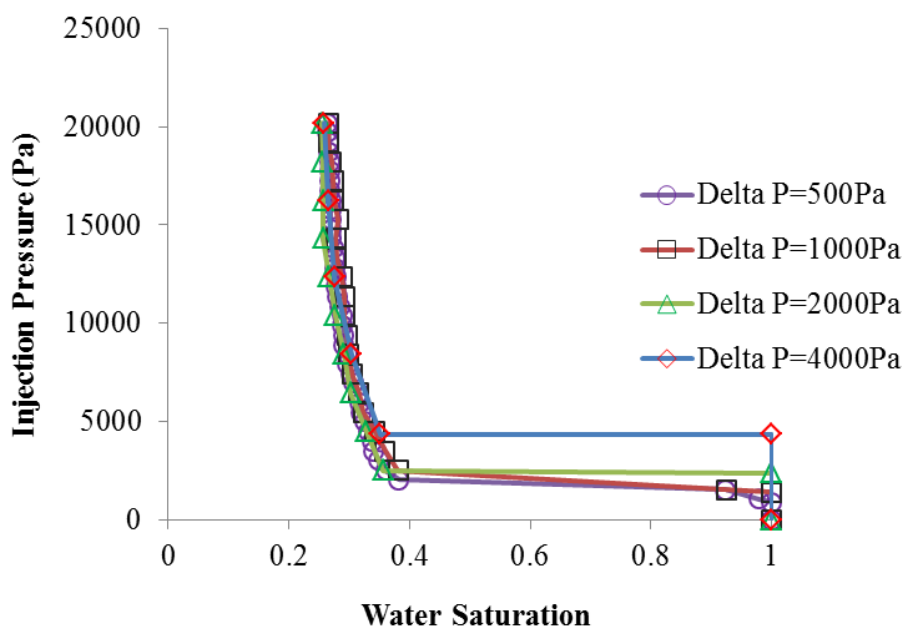
Figure4.26 Correlation between injection pressure and water saturation for steady state flow.

As can be observed from the above figure that the capillary force-saturation correlation for different air injection steps is almost identical with each other denoting that steady capillary pressure curve is an intrinsic properties soil. It is not affected by the pressure step or air injection rate. This is also consistent with experimental observations. Topp et al. (1966) carried out drainge experimetns on a sandy soil with size fraction ranging from 0.1mm to 0.5mm. Water content and pressure head were measured at a point in the middle of the column simultaneously. The water content was varied by controlling the gas phase pressure and allowing water to leave or enter the sample from th bottom of the column. The drainage water content-capillary pressure head relationship, starting at saturation, was determined by three methods: static equilibrium, steady-state flow and unsteady-state flow. As observed during the experiment that the data points for the flow in static equilibrium are very close to the datapoints for the steady-state flow.

4.4.3   Unsteady-State Capillary Pressure Curve

In the Section 4.4.2, the steady capillary curve has been obtained during numerical test. However, during actual air water two-phase flow situation, each step of injection pressure is not always maintained for long enough time to reach the steady state. In these cases, the steady capillary pressure curve may not be applicable anymore. In addition, sometimes the transient two-phase flow process is needed to be simulated, and in these cases the dynamic capillary curve is required.

As suggested by Hassanizadeh and Gray (1990) that by considering the dynamic effect of the drainage process during air-water two-phase flow, the correlation between capillary force and saturation can be expressed as:

$$P^n - P^w = P^c - \tau \frac{\partial S}{\partial t} = f(S) - \tau \frac{\partial S}{\partial t} \qquad (4.11)$$

Where τ [ML^{-1}T^{-1}] is a material coefficient that is a measure of the dynamic effect. According to this theory, in unsteady-state experiments, the dynamic capillary is significant higher than that in the case of equilibrium or steady-state experiments. There is also ample evidence of the significance of dynamic effects on capillary pressure- saturation curve during experiments, for example, this effect is also observed in the drainage experiments carried out on a sandy soil by Topp et al. (1967). In order to study the dynamic effects of air water two-phase flow, the 20-step pressure with the maximum air injection pressure of 20kPa was applied to the network at different time interval in this section. Here the time interval is the defined as the elapse time for each air injection pressure. Three time intervals were employed in this numerical test: 0.125ms, 0.25ms and 0.5ms. The applied air injection pressure for each time interval is shown in Figure 4.27.

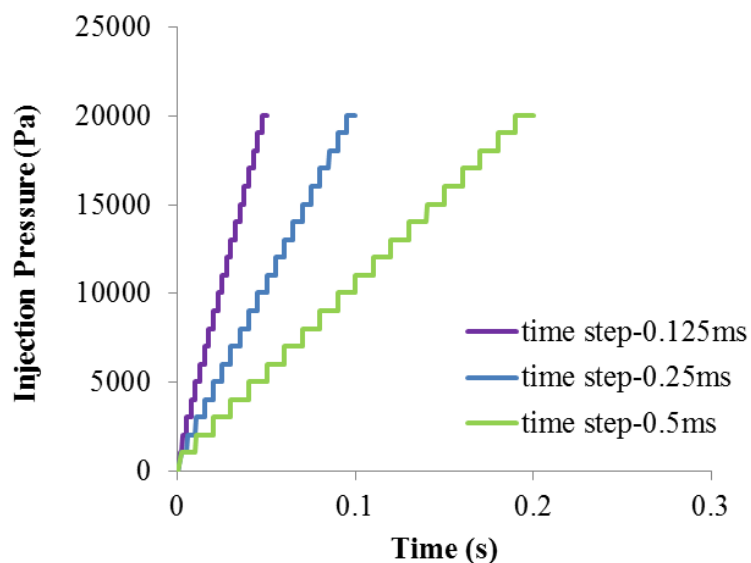**Figure 4.27** The applied three multistep air injection pressures.

During the numerical simulation, both the injected air inejction pressure and the saturation of the whole network are recorded for each set of inejction pressures. The dynamic capillary pressure curves for all the three numerical tests are presented in Figure 4.28.
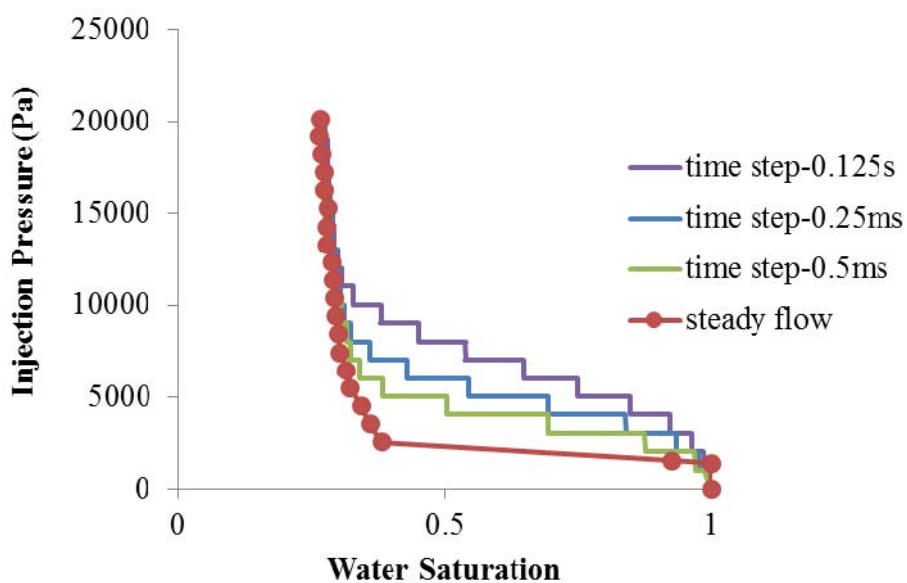
Figure 4.28 Comparison between dynamic and steady capillary pressure curve.

It can be observed from Figure 4.28 that the dynamic capillary pressure curves are always above the steady capillary pressure curve. This is consistent with lots of experimental observations. Topp et al. (1967) compared the correlation between capillary force and water saturation and observed that during unsteady-state, the dynamic capillary pressure is significant higher than in the case of equilibrium or steady sate runs. They were not sure about the sources of this nonuniqueness in capillary pressure-water content curves. As possible causes, they mention the presence of disconnected pendular water rings or the accumulation of traces of contaminants in the air-water interfaces within the sample. Smiles et al. (1971) also observed that when a large drainage step was imposed, the measured capillary force-water content curves lay higher than that during static drainage. In addition, they (1971) determined that the size of the dynamic effect depends on the rate at which water content changes or the size of the change in the boundary suction head. However, it can be further observed that at very low water saturation, there is no obvious different between dynamic capillary curve and steady-state capillary curve. This can be explained by the moving of isolated water cluster at low water saturation. At low water saturation which is corresponding to high capillary pressure, the water spatial distribution in the different tests may be different, however, as more air flow channels have been developed at this stage, there are only a few isolated clusters left in all different simulations. So there are no obvious differences in the capillary curves at low water saturation. Based on this explanation, it can be predicted that the difference between dynamic capillary curve and steady-state capillary curve will be amplified for the simulations with low air injection pressure, in network with wide pore size distribution, with short time interval and etc.

4.4.4 Dynamic Drainage Relative Permeability Curve

In this section, the dynamic relative permeabilities during the multistep pressure simulation are studied. As mentioned in the Section 4.3, air distribution in the soil is not only the function of air saturation, it is also affected by the capillary number for a given pore network. During the simulation with multistep air injection pressures, as air injection pressure was increased by different pressure steps, the historical variation of capillary number for the three tests are quite different, which will lead to quite different historical variation of air spatial distribution. Hence, it can be predicted that the dynamic relative permeability is affected by the different pressure steps.

In this research, three multistep pressure tests were conducted in the Network. During all the three tests, the maximum air injection pressure is 20kPa with the corresponding capillary number of N_{ca}=6.1E-3, and number of pressure steps employed in the three tests are 1, 5, and 10 respectively. The relative permeability during different simulations with varied pressure steps are compared and shown in Figure 4.29.
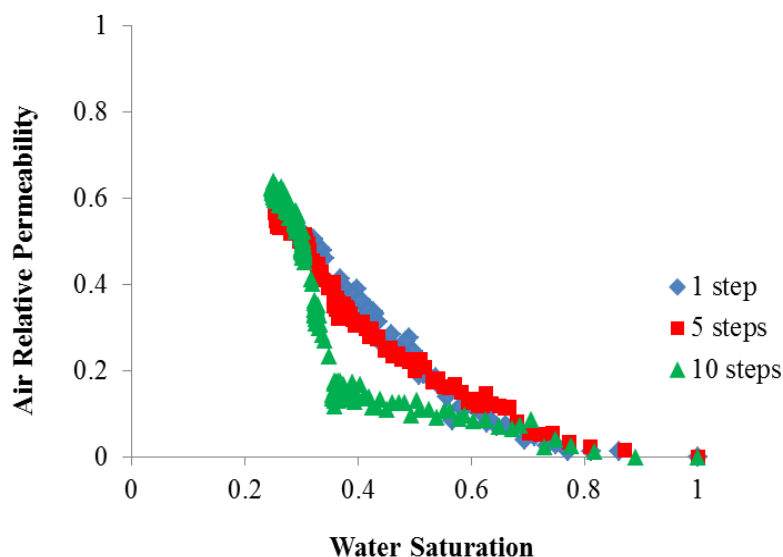
Figure 4.29 Air relative permeabilities in the Network II with N_{ca}=6.1E-3.

Figure 4.29 shows the variation of air relative permeabilities with water saturation during air water two-phase flow with different multistep pressures. From this figure, it can be clearly observed that the whole figure can be divided into three parts: part I is for the water saturation greater than 0.75. This part is corresponding to the initial stage of air injection. In this part, the air permeability is almost zero which means there is no continuous air flow channels developed in the soil for all the three pressure steps. Part II is for the water saturation between 0.35 and 0.75. In this part, the air-water two-phase flow does not reach the equilibrium statement and the flow for all the three pressure steps are in transient statement. In this part, it can be clearly observed that the air relative permeability for the flow with small number of steps is much lower than that with large number of steps. The main reason accounting for this is that for the flow with small number of steps, the capillary number is very small and then the flow pattern is similar to capillary finger. So for the same water saturation, there are more isolated air clusters in the network than that with high pressure step. To confirm this, the front dynamics of flow in the networks in the 1-step-flow and 10-step-flow are compared at water saturation of 0.4, 0.42, 0.44, 0.46, 0.48, and 0.5.
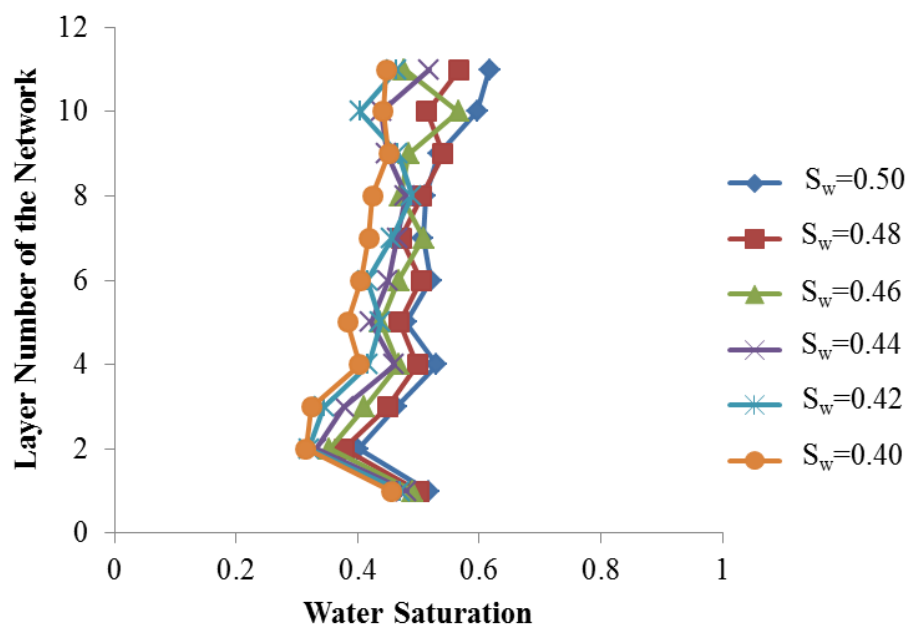
Figure 4.30 Front dynamics for the 1-step air injection pressure.
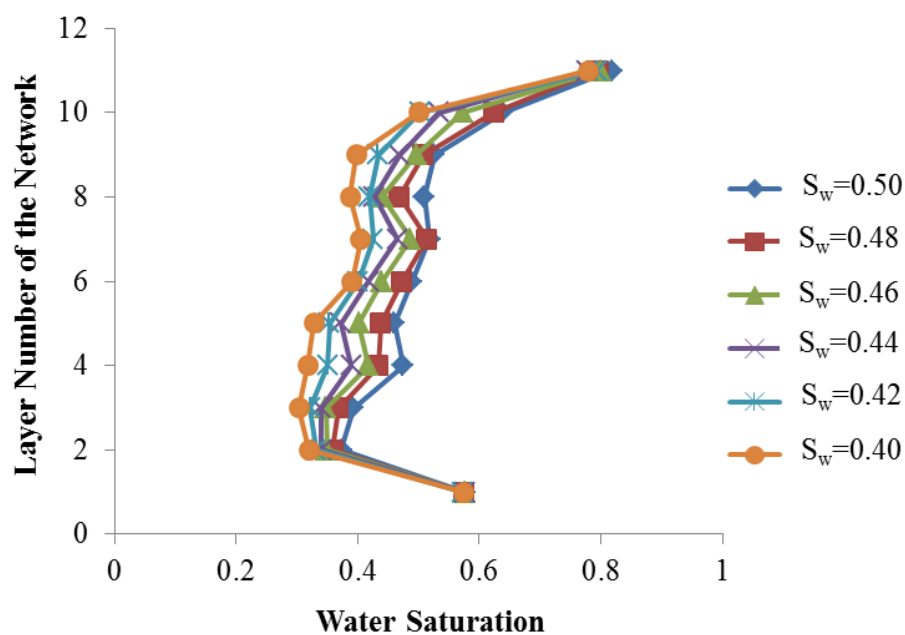
Figure 4.31 Front dynamics for the 10-step air injection pressure.

From the Figure 4.30 and the Figure 4.31, it can be found that the water distribution for the flow with 1 step air injection is more evenly distributed than that with 10-step air injection. For example, for the average water saturation of 0.4 in the network, the biggest difference among the water saturation in different layers for 1 step pressure is less than 0.15; however, the maximum difference among the water saturation of all the network layers with the 10-step air injection pressure is around 0.5. This nonuniform spatial distribution of air water phase accounts for the low relative permeability of the flow with larger number of steps. However, by comparing the simulation results of 1-step pressure and 5-step pressure, it can be further concluded that the dynamic effect on the relative permeability is also affected by the pressure step which is an indicator of the capillary number. For the two flows with close pressure step or capillary number, the dynamic effects on the relative permeability are not obvious.

The third part of the air relative permeability curve shown in Figure 4.29 is for the water saturation less than 0.3 which is corresponding to the steady state of air water two-phase flow. During the steady state, it can be found that the air relative permeabilities of the three numerical tests are almost identical with each other. In order to verify this observation, another similar numerical experiment was conducted. In this test, the maximum air injection is 7.5kPa with the corresponding capillary number of N_{ca}=2.2E-3. Three experiments were performed with 1-step pressures, 7-step pressures and 15-step pressures. The correlations between air relative permeability and water saturation for the three experiments are presented in Figure 4.32.

Figure 4.32 Air relative permeability in the Network II with N_{ca}=2.2 E-3.

As shown in the Figure 4.32, the air relative permeability curves can also be divided into three parts which are corresponding to three stages during two phase flow: initial stage before breakthrough, transient stage and state state stage, which is consistent with the observations obtained from the Figure 4.29. While in the first and the last parts, the air relative permeability of all the three experiments are very close, there are big difference among the three air relative permeability curves in the transient stage. As shown in this figure that at a certain level of water saturation, the lower air injection pressure step is, the smaller the air relative permeability is. As to the third part of the air relative permeability, there are some difference between the results shown in Figure 4.29 and Figure 4.32. Different from the result shown in Figure 4.29 that the relative permeabilities of the three tests are almost identical with each other, the relative permeabilities of the test with 7 and 15 pressure steps are much lower than that with 1-step pressure in Figure 4.32.

This difference between the two sets of simulations is consistent with the prediction mentioned at the beginning of this section that the relative permeability is affected by the capillary number. For the second set of the tests, the maximum air injection pressure is 7.5kPa and this is much lower than that of the first set of the tests with maximum air injection pressure of 20kPa. So for the second set of simulations with low capillary number, the isolated clusters developed during the two phase flow cannot be moved like that in the first set of simulations.

In the above parts, the dynamic properties and the effects of capillary on the simulated relative permeabilities in the Network II are discussed. As air/water relative permeability is a function of spatial distribution of nonwetting/wetting phase, it should be not only affected by the capillary number but also affected by the geometrical and topological properties of pore network as mentioned in Section 4.3. In order the check the effects of geometrical properties of pore network on relative permeability, the Network I which has smaller pore size than that of the Network II is also employed to study the dynamic properties of the relative permeabilities. Two sets of tests were performed in Network I. In the first set of tests, the maximum air injection pressure is 78kPa with the corresponding capillary number N_{ca}=6.1E-3 which is same as that in the simulation in Network II with the maximum air injection of 20kPa. In the other set of tests, the maximum air injection pressure is 27kPa with the corresponding capillary number N_{ca}=2.2E-3 which is same as that in the simulation in Network II with the maximum air injection of 7.5kPa. In the both sets of tests, both 1-step pressure and 10-step pressure are applied and the comparison of the air relative permeabilities obtained in the two sets of tests is provided in the Figure 4.33 and Figure 4.34, respectively.
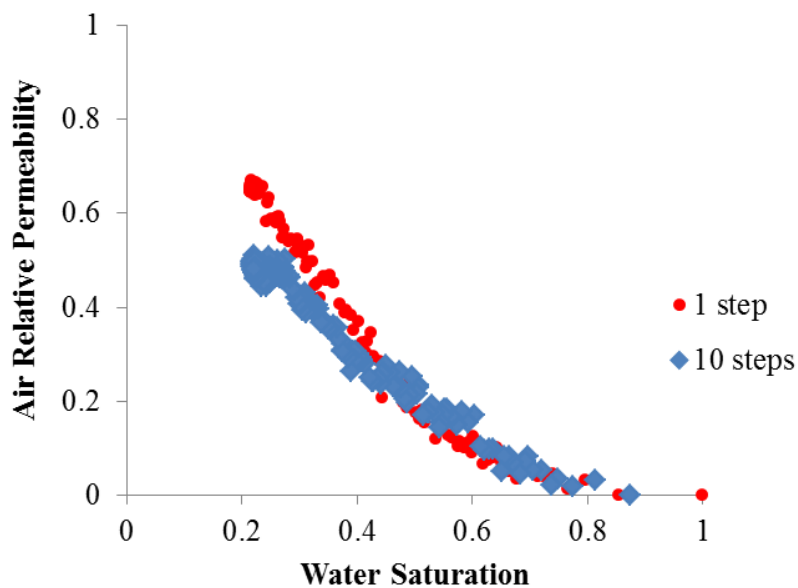
Figure 4.33 Air relative permeability in the Network II with N_{ca}=6.1E-3.

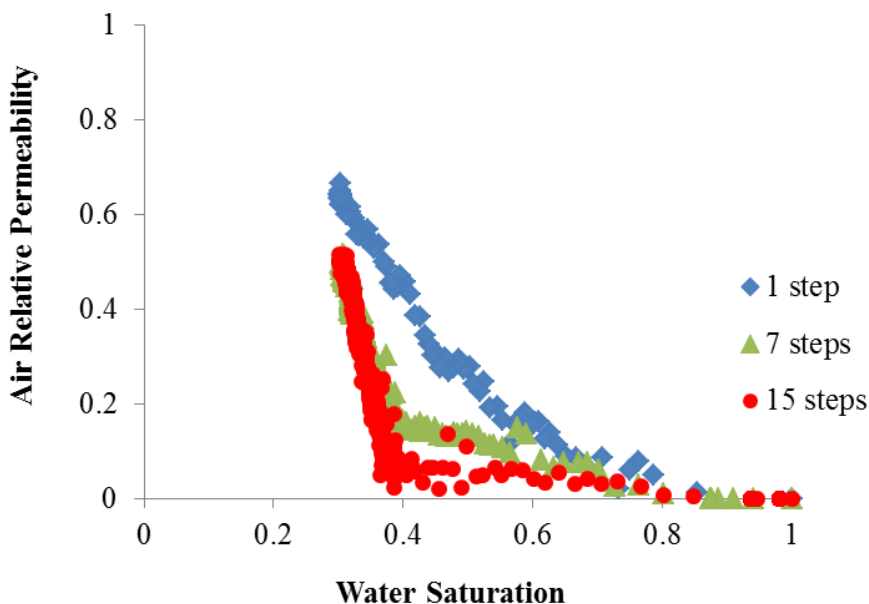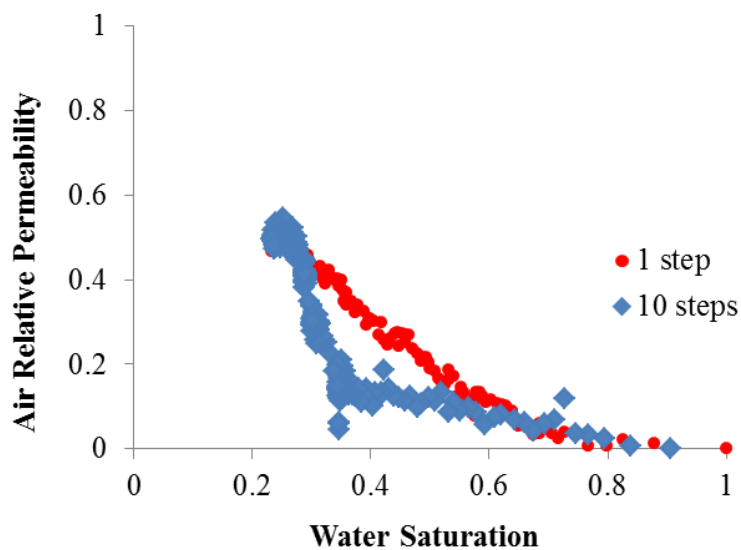**Figure 4.34** Air relative permeability in the Network II with N_{ca}=2.2E-3.

As shown in Figure 4.33, the relative permeability of 1-step pressure test and that of the multi-step pressure test are almost identical with each other; however, there are obvious differences between the 1-step and 10-step relative permeabilities in the simulation of

two-phase flow with the maximum capillary number of N_{ca}=2.2E-3 shown in Figure 4.34. This confirms the conclusion of the effects of capillary number on air relative permeabilities drawn from Figure 4.29 and Figure 4.32. By comparing the Figure 4.29 and Figure 4.33, it can be further observed that for the flow with same maximum capillary number, the difference between the relative permeability of 1-step test and that of multistep test is smaller for Network I than that for Network II. This is consistent with the conclusions about the effect of pore size on dynamic two phase flow mentioned in section 4.3.4 that for the flow with same capillary number in network with small pore size and in network with large pore size, there are more continuous air channels developed in the small-pore- network than that in large-pore network.

The following figure shows the water relative permeability of the three experiments in Network II with the maximum air injection pressure of 20kPa.
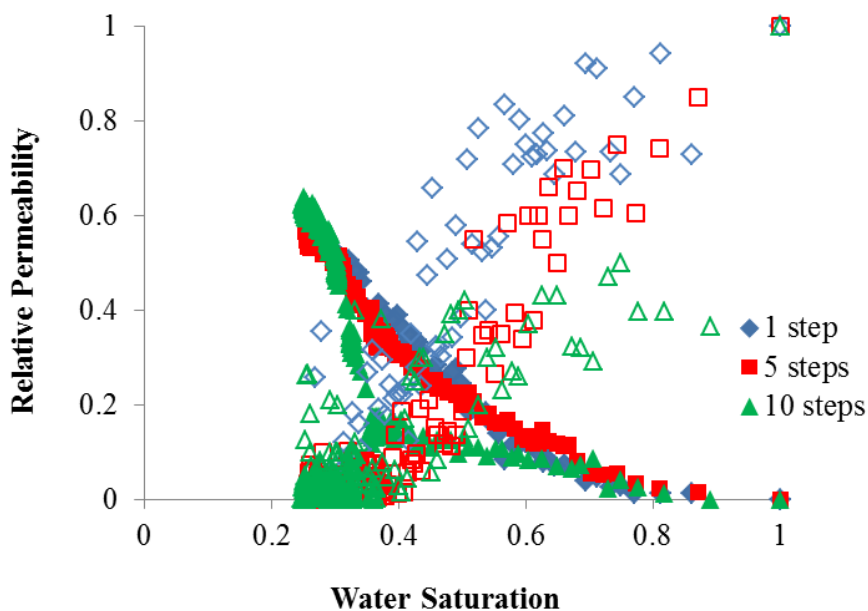
Figure 4.35 Air-water relative permeability in the Network II with N_{ca}=6.1E-3.

From the Figure 4.35, it can be observed that the water relative permeability is more scattered that that of air relative permeability. It can also be found from the above figure that for the flow with small number of steps, its water relative permeability is smaller than that with large number of steps. The mail reason accounting for this is that at low pressure step, it is much easier for water phase getting trapped and isolated. In order to check the effect of network geometrical properties on water relative permeability, the simulation with same maximum capillary number of N_{ca}=6.1E-3 is also performed in Network I. The results of air –water relative permeability is shown in Figure 4.36.
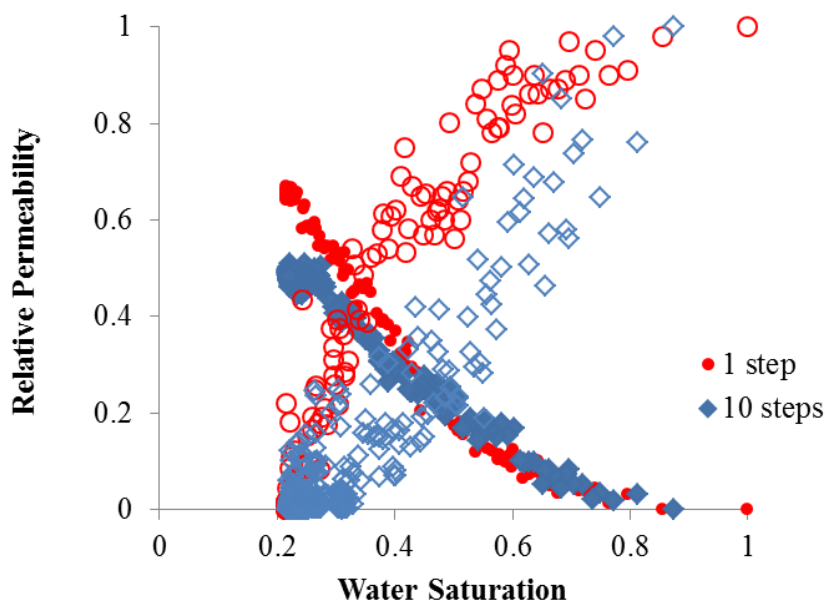
Figure 4.36 Air-water relative permeability in Network I with N_{ca}=6.1E-3.

From Figure 4.36, same conclusion about the effects of pressure steps on the relative permeability as than in Figure 4.35 can be drawn. As shown in figure 4.36, the water relative permeability in 1-step simulation is much higher than that in 10-step simulation. By comparing the Figure 4.35 and Figure 4.36, it can be further observed that the difference between the 1-step and 10-step tests in Network I is much smaller than that

in Network II. In addition, as can be observed from both the Figure 4.35 and Figure 4.36 that, the difference between the water relative permeabilities is much larger than that between the air permeabilities. As shown in Figure 4.36, the two air relative permeabilities curve almost overlap each other, however, the two water relative permeability curves are quite different from each other. The main reason accounting for this is the different flow pattern transition between air and water. During the air water two-phase flow, the air is transferred from discrete phase to continuous phase while the water is changed in the reverse direction.

4.5   Conclusions

In this chapter, the dynamic two-phase flow was studied by the developed dynamic air water two-phase flow model. Two types of numerical tests were conducted in this research; one is by one-step air injection pressure while the other one is by multistep air injection pressure. In one-step air injection pressure test, the effects of capillary number and pore size distribution on residual saturation, non-wetting phase front dynamics, air/water relative permeability and dynamic phase transition were studied. In the multistep pressure tests the dynamic capillary-saturation curve and the dynamic relative air/water permeability were studied.

It is demonstrated in one-step pressure tests that residual saturation is not an intrinsic property of soil; it depends not only on the geometry of the pore network but also on the capillary number of the flow. The residual water saturation of the network with small pore size is smaller than that with large pore size, however, for the same network, the residual saturation decreases along with the increase of capillary number. Similarly, relative permeability is not just a function of saturation, but also a function of air water

spatial distribution during two-phase flow. According to the simulation results, the air water spatial distribution is affected by the capillary number. As a result, the relative permeability is also affected by the capillary number. Compared with air permeability, the water relativity is more scattered. There is an overall trend that with more water drained out during air water two-phase flow, the water relative permeabilities for all flows with different capillary number are decreasing. By comparing the water relative permeabilities for flow with different capillary numbers, it can be further observed that the there is a general trend that at a certain water saturation level, the water relative permeability for the flow with high capillary number is higher than that with low capillary number at a certain level of water saturation. The differences among the relative permeabilities for flows with different capillary number are more apparent for Network III with larger pore size than that for Network I with small pore size. In order to describe the movement of interfaces through a node/bond during drainage process, an interface area weighted capillary pressure was defined in this research. It can be drawn from the simulation results that during the drainage process in the network the larger pores are always filled with the injected air first due to the less resistance than that of the small pores. Then, as more large pores are drained out by the injected air, the water saturation is decreased, meanwhile, if the steady state has not been reached, the pores with smaller pore sizes will be drained, leading to an increase of capillary force. The interfacial area weighted capillary force is also affected by capillary number. During the initial stage of drainge process, the capillary forces for the flow with low capillary number are higher than that with high capillary number. Nonwetting fractional flow was also studied by one-step pressure simulation. According to this research, fractional flow curves can be divided into three segments which are

corresponding to the three stage of air-water two-phase flow during air sparging. Stage one is the initial stage after injecting the air into the soil during which the water saturation is higher than 0.8 ($S_w \geq 0.8$). In this stage, the nonwetting fractional flow is almost equal to zeros for all three capillary numbers which means there are no breakthroughs for air. The third stage is the ending stage of the air sparging during which the water saturation is lower than around 0.4, and the steady state is almost reached in this stage with the nonwetting fractional flow almost equal to 1. Stage two is the stage between the stage 1 and stage 3, which is a two phase flow stage. The cross-overs from single-phase flow to two-phase flow occur in the second stage. This phase transition properties are also affected by the capillary number and geometry of pore networks.

During multistep pressure test, both the steady capillary pressure curve and dynamic capillary pressure curve were studied. As to the steady capillary pressure curve, the capillary force-saturation correlation for different air injection steps were almost identical with each other denoting that steady capillary pressure curve is an intrinsic properties soil, which is consistent with experimental observations by other researchers. As to the dynamic capillary pressure curve, it was always above the steady capillary pressure curve. This conclusion is also consistent with lots of experimental observations. Finally, dynamic relative permeability was also studied in this research. According to the simulation results, the dynamic relative permeability can be divided into three parts: part I is for the water saturation greater than 0.75. This part is corresponding to the initial stage of air injection without air breakthroughs. Part II is for the water saturation between 0.35 and 0.75. In this part, the air-water two-phase flow is in transient statement. In this part, it can be clearly observed that the air relative permeabilities for the flow with small pressure

steps are much lower than that with high pressure steps. The last part is for water saturation less than 0.35 which is corresponding to the steady state. In this part, the differences among relative permeabilities of the tests with different pressure steps become much smaller than that in the second part of the relative permeability curve and these differences are even smaller for flow with high capillary number.

CHAPTER 5

CONCLUSIONS AND FUTURE RESEARCH

5.1   Conclusions

Pore network modeling is now a well-established and successful technique for understanding and predicting a wide range of multiphase flow and transport properties, such as relative permeability, capillary pressure, interfacial area and dissolution rate coefficients. With appropriate data, such models can be predictive, offering the possibility of using pore-scale modeling as a practical tool in porous medium characterization and multiphase flow simulation.

In this research, two approaches of generating 3D stochastic pore networks which can capture both the geometrical information of soil matrix including pore size and throat size distributions with their correlation and the topological information of soil matrix including the distribution of coordination numbers was proposed. The first methodology extracted pore structure from a computer simulated packing of spheres. The modified Delaunay tessellation (MDT) was used to describe the porous media, and modified Nelder-Mead method in conjunction with three pore-merging algorithms was used to generate the pore size and coordination number distributions of the randomly packed spheres. The Biconical Abscissa Asymmetric CONcentric (BACON) bond was used to describe the connection between two adjacent voids. This algorithm was validated by predicting pore structure of a cubic array of spheres of equal radius with known pore sizes, throat sizes and coordination number distributions. The predicted distributions of pore structure agreed well with the measured. Then the algorithm was used to predict permeability   of   randomly   packed   spherical   particles,   and   the   predicted

permeability values were compared with published experimental data. The results showed that the predicted permeability values were in good agreement with those measured, confirming the proposed algorithm can capture the main flow paths of packed beds. The second methodology generated an equivalent pore network of porous media, of which the centers of voids were located in a regular lattice with constant pore center distance. However, this network allowed for matching both main geometrical and topological characteristics of the porous media. A comparison of the two approaches suggested that the second approach can also be used as a predictive tool to quantitatively study the microscopic properties of flow through porous media. However, it should be pointed out here that the proposed two algorithms of developing pore networks is not applicable to clay of which the soil particles cannot be represented by spheres.

Then based on the developed network model, a dynamic two-phase flow model was developed to study temporal evolution of air pressure, air flow rate and time dependence of air spatial distribution in porous media during air sparging. Finally, the developed dynamic air water two-phase flow was applied to study dynamic air water two-phase flow properties. Two types of the numerical tests were performed; one is the type of tests with one-step pressures while the other one is the type of tests with multistep pressures. During the numerical tests, the dynamic flow properties of air water two-phase flow including residual saturation, changing rate of water/air saturation, air and water spatial distribution, air and water relative permeability, dynamic phase transitions with one-step air injection pressure or multistep air injection pressure were studied.

5.2   Future Research

It is believed that this type of dynamic pore-scale model will prove to be very useful to study many aspects of two-phase flow in porous media, in particular aspects involving variables that are very difficult or impossible, to measure physically. For example, by using the developed dynamic pore-scale model, the average interfacial area can be calculated at each time step or pressure step during air water two-phase flow and it is almost impossible to obtain this parameter in the lab. As new theories for multiphase flow in porous media are developed, many of which include these kinds of variables, carefully designed pore-scale network models may be the only realistic option to test the theories, and to attempt quantify functional relationships involving new variables like interfacial area per unit volume of porous medium.

One main task in future research is to improve the developed dynamic pore scale model to allow even more realistic simulation of multi-phase displacements, and lead to a new generation of scale-up tools to transfer detailed pore-scale descriptions to more practical continuum-scale simulators. Firstly, the pore network can be modified by including more realistic geometric descriptions of the pore space. In the current research, the cross section of bond connecting two neighboring pores is in circular shape and this can be replaced by an arbitrary shape for calculating the hydraulic conductivity, capillary force at the air-water interface and etc. Secondly, more complex displacement rules can be introduced to the dynamic model, e.g., rules for film flow or special rules for bubble flow in the pore network. Finally, separate pressure computations for each phase can be introduced to this research. In the current research, it is assumed that in a node filled with both air and water the two fluids share same nodal pressure. If the air and water pressure

can be separated and treated in different way, more accurate simulation of the evolution of air/water pressure and air/water spatial distribution can be obtained.

Another important task to be conducted in future research is to perform micro to macro level analysis to obtain macro behaviors of air water two-phase flow by using micro-mechanics. Two appraoches can be employed for this purpose.

Approach 1: based on the developed microscopic model, deriving the constitutive relationships for air water two-phase flow at macro scale which includes macroscopic capillary pressure-saturation relationship and relative permeability-saturation relationships. It contains two upscaling steps: the first upscaling step goes from the pore scale to local scale. It results in a set of parameters for each material for which an REV can be determined. The next scale transition takes up from the local scale to the macro scale. The definitions of different scales are presented in Figure 5.1.

----------------<0.01m------------------0.01-1m---------------------1-10m----------------
Pore Scale   **Local Scale**   **Macro Scale**

Figure 5.1 Definitions of different levels of analysis on air sparging.

At the pore scale, the two-phase flow processes are predominantly influenced by the pore geometry. At the subsequent larger scale, the local scale, the equations for the conservation of mass and momentum can be derived by volume averaging over the pore scale properties, applying the concept of the REV. Starting from the local scale we have to determine the distribution of all material parameters and constitutive relationships. Applying the capillary equilibrium assumption to a distribution of local P_c–S_w relationships one can determine the saturation distribution for a given capillary pressure.

The weighted arithmetic mean of the saturation distribution gives one point on the macroscopic capillary pressure–saturation relationship.

Approach 2: for directly connecting pore-scale modes with macros-scale modes, a more efficient, domain decomposition method can be used for this purpose. In this appraoch, the medium is decomposed into hundreds of smaller networks (sub-domains) and then coupled with the surrounding models to determine accurate boundary conditions. Each sub-network is computed individually and provided with the input pressure profile, and output the flux profile on six faces. The pressure field at shared boundaries is chosen so that fluxes can match. At each time step, the fluid saturation and pressure of each sub-network are calculated, formulating mass balances at each sub-network, accounting for capillary, viscous and gravity forces, solving the system of coupled and linear equations, calculating the instantaneous flow rates, and updating the local fluid saturations. Finally, the air spatial distribution and air flow dynamics can be obtained in the whole system which is at macroscale.

REFERENCES

Abichou T, Benson CH, Edil TB. (2004). "Network model for hydraulic conductivity of sand-bentonite mixtures." *Canadian Geotechnical Journal*, 41(4), 698-712.

Aboobaker, N., Meegoda, J. N., and Blackmore, D. (2003). "Fractionation and Segregation of Suspended Particles using Acoustic and Flow Fields." *ASCE Journal of Environmental Engineering*, 129 (5), 427-434

Acharya, Ram C., Sjoerd E. A.T.M. van der Zee and Leijnse A. (2004). "Porosity-permeability properties generated with a new 2-parameter 3D hydraulic pore-network model for consolidated and unconsolidated porous media." *Advances in Water Resources*, 27, 707-723.

Adams, J.A. (1999). "System effects on the remediation of contaminated saturated soils and groundwater using air sparging." Dissertation to University of Illinois at Chicago.

Ahlfeld, D.P., Dahmani,A. and Ji, W.(1994). "A conceptual model of field behavior of air sparging and its implications for application." *Ground Water Monitoring and Remediation*, 14(4), 132-139.

Al-Raoush, R., Thompson, K., and Willson, C. S. (2003). "Comparison of network generation techniques for unconsolidated porous media." *Soil Sci. Soc. Am. J.*, 67, 1687-1700.

Amir R., Majid, H. S. (2010). "A new method for generating pore network models of porous media." *Transp. Porous Med.,* 81, 391-407.

Arns Ji Youn, Robins, V., Sheppard, A. P., Sok R. M., Pinczewski W.V. and Knackstedt M. A. (2004). "Effect of network topology on relative permeability." *Transport in Porous media*, 55, 21-46.

Baehr, A.L., Hoag, G.E., and Marley, M.C. (1989). "Removing volatile contaminants from the unsaturated zone by inducing advective air phase transport." *J. Contaminant Hydrology*, 4, 1-26.

Bakke, S. and Øren, P. E. (1997). "3-d pore-scale modeling of sandstones and flow simulations in the pore networks." *Society of Petroleum Engineers Journal*, 2, 136-149.

Baldwin, C. A., Sederman, A. J., Mantle, M. D., Alexander, P. and Gladden, L. F. (1996). "Determination and characterization of the structure of a pore space from 3d volume images." *Journal of Colloid and Interface Science*, 181, 79-92.

Balhoff, M.T, Thompson, K.E. (2004). "Modeling the steady flow of yield-stress fluids in packed beds." *AIChE J.*, 50, 3034-3048.

Blunt, M. J. (2001). "Flow in porous media-pore network models and multiphase flow." *Current Opinion in Colloid & Interface Science*, 6, 197-207.

Blunt. M.J., Jackson, M.D., Piri, M, Valvatne, P.H. (2002). "Detailed physics, predictive capabilities and macroscopic consequences for network models of multiphase flow." *Adv. Water Res.*, 25(8-12), 1069-1089.

Blunt, M., King, P. (1990). "Macroscopic parameters from simulations of pore scale flow." *Physical Review A*, 42 (8): 4780-4789.

Brooks, M. C., Wise, W. R. and Annable, M. D. (1999). "Fundamental changes in in-situ air sparging flow patterns." *Ground Water Monit. Rem.*, 19(2), 105-113.

Byrant, S.L., Cade, C., Mellor, D. (1993). "Permeability prediction from geologic models." *Am. Ass. Petrol. Geol. Bull.*, 77(8), 1338-1350.

Celia, M. A., Reeves, P. C., Ferrand, L. A. (1995). "Recent advances in pore scale models for multiphase flow in porous media." *Reviews of Geophysics*, 33(2), 1049.

Chan, S.K. and NG, K.M. (1988). "Geometrical characteristics of the pore space in a random packing of equal spheres." *Powder Technology*, 54, 147-155.

Chandler, R., Koplick, J., Lerman, K., and Willemsen, J. F. (1982). "Capillary displacement and percolation in porous media." *J. Fluid. Mech.*, 119, 249-267.

Chatzis, I. and Dullien, F.A. L. (1985). "The modeling of mercury porosimetry and the relative permeability of mercury in sandstones using percolation theory." *Int. Chem. Eng.*, 25(1), 47-66.

Chu, C.F., NG, K.M. (1989). "Flow in packed tubes with a small tube to particle diameter ratio." *AIChE J.*, 35(1), 148-158.

Cousin, I, Levtiz, P, Bruand, A. (1996). "Three-dimensional analysis of loamy-clay soil using pore and solid chord distributions." *Eur. J. Soil Sci.*, 47, 439-452.

Crawford, J. W. (1994). "The relationship between the structure and hydraulic conductivity of soil." *European Journal of Soil Science,* 45, 493-502.

Cundall, P. A. and Strack, O.D.L. (1979)."A Discrete Numerical Model for Granular Assemblies." *Geotechnique*, 29(1), 47-65.

Dias, M. M. and Payatakes, A. C. (1986). "Network models for two-phase flow in porous media. Part 2. Motion of oil ganglia," *J. Fluid Mech.*, 164, 337-358.

Diaz, C.E., Chatzis, I. and Dullien, F.A.L. (1987). "Simulation of capillary pressure curves using bond correlated site percolation on a simple cubic network." *Transport in Porous Media,* 2, 215-240.

Dillard, L.A., Blunt, M.J. (2000). "Development of a pore network simulation model to study nonaqueous phase liquid dissolution." *Water Resour. Res.,*36(2), 439-454.

Dixit, A.B., McDougall, S.R., Sorbie, K.S. (1998). "A pore-level investigation of relative-permeability hysteresis in water-wet systems." *SPE Journal,* 3(2),115-123.

Dixit, A.B., McDougall, S.R., Sorbie, K.S., Buckley, J.S. (1999). "Pore-scale modeling of wettability effects and their influence on oil recovery." *SPE Reservoir Eval. Eng.,* 2, 25-36.

Dixit, A.B., Buckley, J.S., McDougall. S.R., Sorbie, K.S. (2000). "Empirical measures of wettability in porous media and the relationship between them derived from pore-scale modeling." *Transp. Porous Media*, 40(1), 27-54.

Dullien, F.A. L. (1992). "Porous Media: Fluid Transport and Pore Structure." 2nd edn. Academic Press, San Diego, CA.

Elder, C. R. and Benson, C. H. (1999). "Air channel formation, size, spacing, and tortuosity during air sparging." *Ground Water Monitoring & Remediation*, 19 (3), 171-181.

Fenwick, D. H., and Blunt, M. J. (1998). "Three-dimensional modeling of three-phase imbibition and drainage." *Advances in Water Resources*, 21 (2), 121-143.

Fischer, U, Celia, M.A. (1999). "Prediction of relative and absolute permeabilities for gas and water from soil water retention curves using a pore-scale network model." *Water Resour. Res.*, 35(4), 1089-1100.

Gao, S., Meegoda, N.J., Hu, L. (2011). "Microscopic research on air sparging I-Network model development." *Geo-Frontiers 2011*.

Gauglitz, P.A., Laurent, C.M. and Radke, C.J. (1988). "Experimental determination of gas-bubble breakup in a constricted cylindrical capillary." *Ind. Eng. Chem. Res.*, 27, 1282-1291.

Gauglitz, P.A., Radke, C.J. (1990). "The dynamics of liquid film breakup in constricted cylindrical capillaries." *J. Colloid Interf. Sci.,* 134, 14-40.

Geistlinger, H., Krauss, G., Lazik, D., and Luckner, L. (2006). "Direct gas injection into saturated glass beads: Transition from incoherent to coherent gas flow pattern." *Water Resources Research*, 42, W07403.

Griffith, P. and Wallis, G.B. (1961). "Two-phase slug flow." *J. Heat Transfer,* 83, 307-320.

Harleman, D.F., Mehlhorn, P.F., Rumer, R.R. (1963). "Dispersion-permeability correlation in porous media." *Journal of Hydraulics Division, Proceedings of the American Society of Civil Engineers*, 89(HY2), 67-85.

Hassanizadeh, S.M. and Gray, W.G. (1990). "Mechanics and thermodynamics of multiphase flow in porous media including interphase boundaries." *Adv. Water Resour.* 13, 169-186.

Haughey, D.P., Beveridge, G.G. (1966). "Local voidage variation in a randomly packed bed of equal-sized spheres." *Chem. Eng. Sci.,* 21,905-916.

Haughey, D.P., Beveridge, G.G. (1969). "Structural properties of packed beds-a review." *The Canadian Journal of Chemical Engineering*, 47, 130-140.

Knudsen H. A. and Hansen A. (2006). "Two-phase flow in porous media: dynamical phase transition." *European Physical Journal B*, 49, 109-118.

Heiba, A. A., Davis, H. T., and Scriven, L. E. (1984). "Statistical network theory of three-phase relative permeabilities." *SPE/DOE No. 12690*.

Hewitt, G.F., Robertson, D.N. (1969). 'Studies of two phase patterns by simultaneous X-ray and flash photography." UKAFA, Harwell: Report, AERE-M 2159.

Hu, L., Wu, X., Liu, Y., Meegoda, J.N., Gao, S. (2010) "Physical modeling of air flow during air sparging remediation," *Environmental Science and Technology*, 44 (10), 3883-3888.

Ioannidis, M.A., Chatzis, I. (2000). "On the geometry and topology of 3D stochastic porous media." *Journal of Colloid and Interface Science*, 229,323-334.

Jerauld, G. R., and Salter, S. J. (1990). "The effect of pore-structure on hysteresis in relative permeability and capillary pressure: pore level modeling." *Transport in Porous Media*, 5,103-151.

Ji, W., Dahmani, A., Ahlfeld, D., Lin, J.D. and Hill, E. (1993). "Laboratory study of air sparging: air flow visualization." *Ground Water Monitoring Review*, Fall, 115-126.

Johnson, R.L., Johnson, P.C., McWhorter, D.B., Hinchee, R.E. and Goodman, I. (1993). "An overview of in situ air sparging." *Ground Water Monitoring Review*, Fall, 127-135.

Jodrey, W.S., Tory, E.M. (1979). "Simulation of random packing of spheres." *J. Simulation*, 32, 1-12.

Jullien R. and Meakin P. (1987). "Simple three-dimensional models for ballistic deposition with restructuring." *Europhysics Lett.,* 4, 1385-1390.

Juncosa, S.G.T. (1993). "Removal of Benzene and TCT from Water and Soil by Air Sparging." Master's thesis, Department of Civil Engineering. University of Massachusetts-Lowell.

Kagan, M., Pinczewski, W.V.(2000). "Menisci in a diamond-shaped capillary." J. *Colloid Interface Sci.*, 230, 452-454.

Karsten, E.T., Fogler, H.S. (1997). "Modeling flow in disordered packed beds from pore-scale fluid mechanics." *AIChE J.*, 43(6), 1377-1389.

Kornhauser, I., Rojas, F., Faccio, R., Riccardo, J., Vidales, A. and Zgrablich, G. (1997). "Structure characterization of disordered porous media? A memorial review dedicated to Vicente Mayagoitia." Fractals 5(3), 355-377.

Koplik, J. and Lasseter, T. J. (1982). "Two-phase flow in random models of porous media.' *57th Annual SPE of AIME Fall Tech. Conf.*, New Orleans, SPE No. 11014.

Kwiecien, M. J., Macdonald, I. F., and Dullien, F. A. L. (1990). "Three-dimensional reconstruction of porous media from serial section data." *Journal of Microscopy,* 159 (3), 343-359.

Larson, R. B., Scriven, L. E., and Davis. H. T. (1981). "Percolation theory of two phase flow in porous media." *Chem. Eng. Sci.,* 36, 57-73.

Lenormand, R., Touboul, E., and Zarcone, C. (1988). "Numerical models and experiments on immiscible displacements in porous media." *J. Fluid Mech.,* 189, 165-187.

Leonard, W.C. and Brown, R.A. (1992). "Air sparging: an optimal solution." *Proceedings of Petroleum Hydrocarbons and Organic Chemicals in Groundwater,* Prevention, Detection and Restoration, Houston, Texas, 349–363.

Lerdahl, T.R., Oren, P.E., Bakke, S. (2000). "A predictive network model for three-phase flow in porous media." *Proceedings of the SPE/DOE Symposium on Improved Oil Recovery*, Tulsa, OK, April.

Levine, M. M. and Chernick, J. (1965). "A numerical model of random packing of spheres." *Nature*, 208(5005), 68-69.

Liang, Z. R., Phillippi, P. C., Fernandes, C. P., and Magnani, F. S. (1999). "Prediction of permeability from the skeleton of three-dimensional pore structure." *SPE Reservoir Evaluation and Engineering*, 2(2), 161-168.

Lindquist, W.B., Venkatarangan, A., Dunsmuir, J., Wong, T. (2000). "Pore and throat size distributions measured from synchrotron X-ray tomographic images of fontainebleau sandstones." J. Geophys. Res., 105B, 21508-21528.

Lo, I. M. C., Hu, L. M. and Meegoda, J. N. (2004) "Centrifuge Modeling of LNAPLs Transport in Unsaturated Soils." *ASCE Journal of Geotechnical and Geo-environmental Engineering*, 130 (5), 535-540.

Lochmann, K., Oger, L. and Stoyan, D. (2006). "Statistical analysis of random sphere packings with variable radius distribution." *Solid State Science*, 8, 1397-1413.

Lowry, M. I. and Miller, C. T. (1995). "Pore-scale modeling of nonwetting-phase residual in porous media." *Water Resources Research*, 31(3), 455-473.

Lundegard, P.D., and Andersen, G. (1996). "Multiphase numerical simulation of air sparging performance." *Ground water*, 34(3), 451-460.

Man, H.N., Jing, X.D. (1999). "Network modeling of wettability and pore geometry effects on electrical resistivity and capillary pressure." *J. Petroleum Sci. Eng.,* 24, 255-267.

Man, H.N., Jing, X.D. (2000). 'Pore network modeling of electrical resistivity and capillary pressure characteristics." *Transp. Porous media*, 41, 263-285.

Man, H.N., Jing, X.D. (2000). "Network modeling of strong and intermediate wettability on electrical resistivity and capillary pressure." *Adv. Water Resour.,* 24, 345-363.

Mani, V. and Mohanty, K.K. (1999). "Effect of pore-space spatial correlations on two-phase flow in porous media." *Journal of Petroleum Science and Engineering,* 23,173-188.

Mardlaw, N.C., Li, Y., Forbes, D. (1987). "Pore-throat size correlation from capillary pressure curves." *Transport in Porous Media*, 2, 597-614.

Markus, H., Roland, G., Miller, C. T., (2003). "Calibration of a pore- network model by a pore-morphological analysis." *Transport in Porous Media*, 51, 267-285.

Marley, M., Hazenbrouck, D.J. and Walsh, M.T. (1992). "The application of in situ air sparging as an innovative soils and groundwater remediation technology." *Ground Water Monitoring Review*, 12, 137–145.

Marulanda, C. (2001). "A study of air flow through saturated porous media and its applications to in-situ air sparging." *Ph.D. Dissertation*, Massachusetts Institute of Technology.

Mattews, G., Moss, A., Spering, M., and Voland, F. (1993). "Network calculation of mercury intrusion and absolute permeability in sandstone and other porous media." *Powder Technol.,* 76, 95-107.

Mattews, G., Ridgway, C., and Spering, M. (1995). "Void space modeling of mercury intrusion hysteresis in sandstone, paper coating, and other porous media." J. *Colloid Interface Sci.*, 171, 8-27.

Mayagoitia, V., Rojas, F. and Kornhauser, I. (1985). "Pore network interactions in ascending processes relative to capillary condensation*." J. Chem. Soc. Faraday Trans. I.,* 81, 2931-2940.

Mayagoitia, V., Rojas, Kornhauser, I. and Prez-Aguilar, H. (1997). "Modeling of porous media and surface structures: Their true essence as networks." Langmuir 13, 1327-1331.

McCray, J. E. (2000). "Mathematical modeling of air sparging for subsurface remediation: state of the art." *Journal of Hazardous Materials*, 72, 237-263.

Meakin, P. (1983). "Diffusion-controlled cluster formation in 2-6-dimensional space." *Phys. Rev. A*, 27(3), 1495-1507.

Meakin, P. (1983). "Diffusion-controlled deposition on fibers and surfaces." *Phys. Rev. A*, 27(5), 2616-2623.

Meakin, P. and Stanley, H. E. (1984). "Novel dimension-independent behavior for diffusive annihilation on percolation fractals." *J. Phy. A. Math. Gen.,* 17, 1173-1177.

Meegoda, N. J., King, I. P., and Arulanandan, K. (1989) "An expression for the permeability of anisotropic granular media." *International Journal for Numerical and Analytical Methods in Geomechanics*, 13, 575-598.

Meegoda, J. N., and Ratnaweera, P. (2008) "Prediction of Effective Porosity of Contaminated Soils using Electrical Properties," *ASTM Geotechnical Testing Journal*, 31(4), 344-357.

Meegoda, J. N. and Tantemsapya, N. (2007) "Microscopic Modeling of Colloidal Silica Stabilized Granular Contaminated Soils." *ASCE Journal of Materials in Civil Engineering*, 19 (1), 91-98.

Mishima, K. and Hibiki, T. (1996). "Some characteristics of air-water two-phase flow in small diameter vertical tubes." *Int. J. Multiphase Flow*, 22 (4), 703-712.

Moscinski, J., Bargiel, M., Rycerz, Z.A., Jacobs, P.W.M. (1989). "The force-biased algorithm for the irregular close packing of equal hard spheres." *Mol. Simulat.*, 3, 210-212.

Moscinski, J., Bargiel, M. (1991). "C-language program for the irregular close packing of hard spheres." *Computer Phys. Comm.*, 64, 183-192.

Nadege, R., Vincens, E., and Cambou, B. (2008). "A statistical analysis of void size distribution in a simulated narrowly graded packing of spheres." *Granular Matter*, 10, 457-468.

Nelder, J.A. and Mead, R. (1965). "A simplex method for function minimization." *Computer J.*, 7, 308-313.

Niasar, V.J., Hassanizadeh, S.M., Leijnse, A. (2008). "Insights into the relationships among capillary pressure, saturation, interfacial area and relative permeability using pore-network modeling." *Transport in Porous Media,* 74, 201-219.

Niasar, V. J., Hassanizadeh, S.M., and Dahle, H. K. (2010). "Non-equilibrium effects in capillarity and interfacial area in two-phase flow: dynamic pore-network modeling." *J. Fluid Mech.*, 665: 38-71.

Noack, A.G., Grant, C.D., Chittleboroough, D.J. (2000). "Colloid movement through stable soils of low cation-exchange capacity." *Environ. Sci. Technol.* 34, 2490-2497.

Nolan, G. T., Kavanagh, P. E. (1994). "The size distribution of interstices in random packings of spheres." *Powder Technology,* 78, 231-238.

Nyer, E. K., Suthersan S.S. (1993). "Air sparging: Savior of ground water remediations or just blowing bubbles in the Bath Tub?" *Ground Water Monitoring & Remediation*, 13 (4), 87-91.

Oger, L., Troadec, J.P., Richard, P., Gervois, A., Rivier, N. (1997). "Voronoi tessellation of packings of equal spheres." *Powders and Grains*, 97, 287-290.

Okabe, H. and Blunt, M. J. (2003). "Multiple-point statistics to generate geologically realistic pore-scale representations." *Proceedings of the society of core analysts annual meeting*, SCA2003-A33, 22-25 September, PAU, FRANCE.

Oren, P.E., Bakke, S., Arntzen, O.J. (1998). "Extending predictive capabilities of network models." *SPE J*, 3, 324-336.

Pathak, P., Davis, H.T., and Scriven, L. E. (1982). "Dependence of residual non-wetting liquid on pore topology." *SPE Journal*, No. 11016.

Patzek, W.T., Silin, D.B. (2001). "Shape factor and hydraulic conductance in noncircular capillaries I. One-phase creeping flow." *Journal of Colloid and Interface Science*, 236, 295-304.

Patzek, W.T., Kristensen, J.G. (2001). "Shape factor correlations of hydraulic conductance in noncircular capillaries II. Two-phase creeping flow." *Journal of Colloid and Interface Science*, 236, 305-317.

Payatakes, A.C., Tien, C., Turian, R.M. (1973). "A new model for granular porous media: Part I. Model formulation." *AIChE Journal*, 19(1), 58-67.

Peterson, J.W., Murray, K.S., Tulu, Y.I., Peuler, B.D. (2001). "Air-flow geometry in air sparging of fine-grained sands." *Hydrogeology Journal*, 9, 168-176.

Pushkina, O. L. and Sorokin, Y. L. (1969). "Breakdown of liquid film motion in vertical tubes." *Heat Trans. Soviet Res.,* 1 (5).

Rajaram, H., Ferrand, L. A. and Celia, M. A. (1997). "Preddiction of relative permaibilities for unconsoloataed solis using pore-scale network models." *Water Resources Research*, 33(1), 43-52.

Reddy, K. R., and Adams, J. (2008). "Conceptual modeling of air sparing for groundwater remediation." *Proceedings of the 9th international symposium on environmental geotechnology and global sustainable development*, Hong Kong, June 2008.

Reddy, K.R., and Adams, J.A. (2001). "Effects of soil heterogeneity on air flow patterns and hydrocarbon removal during in-situ air sparing." *Journal of Geotechnical and Geoenvironmental Engineering*, ASCE, 127(3), 234-247.

Reddy, K. R., Kosgi, S., and Zhou, J. (1995). "A review of in situ air sparging for the remediation of VOC-contaminated saturated soils and groundwater." *Hazardous Waste and Hazardous Materials*, 12(2), 97-118.

Reeves, P. C. and Celia, M. A. (1996). "A functional Relationship between capillary pressure, saturation, and interfacial areas as revealed by a pore-scale network model." *Water Resources Research,* 32(8), 2345-2358.

Riccardo, J., Steele, W., Cuesta, A. and Zgrablich, G. (1997). "Pure Monte Carlo simulation of model heterogeneous substrates: From random surfaces to many site correlations." *Langmuir,* 13,1064-1072.

Rintoul, M. D., Torquato, S., Yeong, C., Kaene, D. T., Erramili, S., Jun, Y. N., Dabbs, D. M., and Aksay, I. A. (1996). "Structure and transport properties of a porous magnetic gel via x-ray microtomography." *Physical Review E*, 54, 2663–2669.

Rouault Y., Assouline S. (1998). "A probabilistic approach towards modeling the relationships between particle and pore size distributions: the multicomponent packed sphere case." *Power Technology,* 96, 33-41.

Roychoudhury, A.N. (2001). "Dispersion in unconsolidated aquatic sediments." *Estuar Coastal Shelf Sci.,* 53, 745-757.

Scheidegger, A.E., (1958). "The Physics of Flow Through Porous Media." Macmillan, New York, pp. 91-113.

Schneider KJ. (1963). "Investigation of the influence of free thermal convection on heat transfer through granular material." *Proceedings of the 11th international congress of refrigeration*, 2, 247-254.

Selker, J. S., Niemet, M., Mcduffie, N. G., Gorelick, S. M. and Parlange, J. Y. (2007). "The local geometry of gas injection into saturated homogeneous porous media." *Transport in Porous Media,* 68, 107-127.

Semer, R., Adams, J.A. and Reddy, K.R. (1998). "An experimental investigation of air flow patterns in saturated soils during air sparging." *Geotechnical and Geological Engineering,* (16) 59-75.

Sharon, E. R. and Yavuz, C. M. (1998). "Air bubble migration in a granular porous medium: Experimental studies." *Water Resources Research*, 34 (5), 1131-1142.

Smiles, D.E., Vachaud, G. and Vauclin, M. (1971). "A test of the uniqueness of the soil moisture characteristic during transient, non-hysteretic flow of water in a rigid soil." *Soil Sci. Soc. Am. Proc.,* 35, 535-539.

Steven, B, Blunt, M. J. (1992) "Prediction of relative permeability in simple porous media." *Physical Review A*, 46(4), 2004-2011.

Steven, L.B., King, P.R., Mellor, D.W. (1993). "Network model evaluation of permeability and spatial correlation in a real random sphere packing." *Transp. Porous Media*, 11, 53-70.

Stevenson, K., Ferer, M., Bromhal, G.S., Gump, J., Wilder, J. and Smith, D.S. (2006). "2-D network model simulations of miscible two-phase flow displacements in porous media: Effects of heterogeneity and viscosity." *Physica A*, 367, 7-24.

Thovert, J.F., Yousefian, F., Spanne, P., Jacquin, C.G. and Adler, P.M. (2001). "Grain reconstruction of porous media: application to a low-porosity Fontainebleau sandstone." *Physical Review E*, 63.

Topp, G.C., Klute, A. and Peters, D.B. (1967). "Comparison of water content-pressure head data obtained by equilibrium, steady-state, and unsteady-state methods." *Soil Sci, Soc. Amer. Proc.* 31, 312-314.

Tsakiroglou, C.D. and Payatakes, A.C. (1991). "Effects of pore-size correlations on mercury porosimetry curves." *Journal of Colloid and Interface Science,* 146(2), 479-494.

Vischer, W.M., Bolsterli, M. (1972). "Random packing of equal and unequal spheres in two and three dimension." *Nature (London)*, 239, 504.

Vogel, H.J., Roth, K. (2001). "Quantitative morphology and network representation of soil pore structure." *Adv. Water Resour.*, 24, 233-242.

Ward, J.C. (1964). "Turbulent flow in porous media." *Journal of Hydraulics Division, Proceedings of the American Society of Civil Engineers*, 90(HY5), 1-12.

Wardlaw, N.C., Li, Y. and Forbes, D. (1987). "Pore-throat size correlation from capillary pressure curves." *Transport in Porous Media*, 2, 597-614.

Wyllie, M.R.J, Gregory, A.R. (1955). "Fluid flow through unconsolidated porous aggregates." *Industrial and Engineering Chemistry*, 47(7), 1379-1388.

Yanuka, M., Dullien, F. A. L. and Elrick, D.E. (1986). "Percolation processes and porous media. 1. Geometrical and topological model of porous-media using a 3-dimensional joint pore-size distribution." *J. Colloid Interf. Sci.,* 112(1), 24-41.

Yang, R.Y., Zou, R.P., Yu, A.B. (2002). "Voronoi tessellation of the packing of fine uniform spheres." *Phys. Rev. E*, 65, 041032

Yavuz, C. M., Cihan, A., and Drazenovic, M. (2004). "Rise velocity of an air bubble in porous media: Theoretical studies." *Water Resources Research*, 40, W04214.